Novel Lorentz Force Velocimetry System based on Bulk High-temperature Superconductors

Dissertation

zur Erlangung des akademischen Grades

Doktoringenieur
(Dr.-Ing.)

vorgelegt der
Fakultät für Maschinenbau der
Technischen Universität Ilmenau

von Herrn M.Sc. Oleksii Vakaliuk

Gutachter:

Univ.-Prof. Dr.-Ing. habil. Thomas Fröhlich (Doktorvater)	Technische Universität Ilmenau
Prof. Specially-Appointed, Dr. Eng. Tetsuo Oka	Shibaura Institute of Technology
Dr. Bernd Halbedel	Technische Universität Ilmenau

Tag der Einreichung: 02. 12. 2019
Tag der wissenschaftlichen Aussprache: 22. 04. 2020

Kurzfassung

Die **L**orentz**k**raft**a**nometrie (LKA) ist eine Technik zur Messung der Geschwindigkeit von elektrisch leitfähigen Flüssigkeiten. Sie ist eine nicht-invasive Messtechnik, die besonders vorteilhaft für heiße, opake und aggressive Elektrolyte ist. Die LKA wurde für Salzwasser als Modellelektrolyt erfolgreich mit **D**auer**m**agnetanordnungen (DM) ohne magnetischen Rückschluss, aber mit gezielter Flussführung (Halbach-Array) und hochpräzisen **K**raft**m**ess**s**ytemen (KMS) auf Basis der interferometrischen Messung der Auslenkung des Magnetsystems und der elektromagnetischen Kompensation der Auslenkung demonstriert.

Jedoch sind die DM-Systems begrenzt hinsichtlich der magnetischen Oberflächen-flussdichte auf 0.5 T trotz der Nutzung des zurzeit energiereichsten Dauermagnetwerk-stoffes (Nd-Fe-B) sowie der Masse auf 1 kg aufgrund der verwendbaren KMS. Weiterhin waren bei den LKA-Experimenten die DM nur 3 mm vom fließenden Salzwasser entfernt, wodurch eine effektive Wechselwirkung der vom DM erzeugten magnetischen Flussdichte mit dem Durchflussvolumen erreicht wurde. Bei heißen und aggressiven Elektrolyten (z.B. Säuren, Laugen, Salzschmelzen und Glasschmelzen) ist eine solche enge Ankopplung an den Strömungskanal aufgrund der dicken thermischen Isolier-wände nicht möglich. Darüber hinaus betragen die Leitfähigkeiten solcher Elektrolyte von $\sigma < 10 \, \mathrm{S \, m^{-1}}$ und ihre üblichen Strömungsgeschwindigkeiten sind $u < 1 \, \mathrm{m \, s^{-1}}$.

Um die LKA für schwach leitfähige Elektrolyte zu erweitern, ist eine Magnetfelderzeu-gung von $> 1 \, \mathrm{T}$ erforderlich. Ein **H**och**t**emper**a**tur**s**upraleiter-Bulk (Bulk-HTS) kann ein Magnetfeld von mehreren Tesla erzeugen und somit die LKA-Leistung deutlich verbessern und die bisher genutzten DM ersetzen.

Diese Arbeit zielt deshalb darauf ab, Bulk-HTS's in der LKA unter Berücksichtigung der kritischen Verbindungen zwischen der Funktionalität von Bulk-HTS's und dem KMS einzusetzen und ein LKA-System mit Bulk-HTS's zu entwerfen, herzustellen und zu testen.

Wie Bulk-HTSs in ein LKA-System implementiert werden können und welche Her-ausforderungen damit verbunden sind, wurde experimentel untersucht und die notwendi-gen Bedingungen fixiert. Anschließend wurde erstmals die Einsetzbarkeit von Bulk-HTS's für die LKA mit einer vereinfachten Flüssigstickstoffkühlung experimentel nach-gewiesen. Zusätzlich zum Experiment wurde ein numerisches 3D-Modell entwickelt um die notwendigen einzufrierenden magnetischen Flussdichten B_T für ein Modellelek-trolyt mit $(\sigma \cdot u) = 10 \, \mathrm{S \, s^{-1}}$ zu berechnen.

Die Ergebnisse wurden für die Entwicklung eines neuartigen LKA-System auf Basis eines Bulk-HTS als Magnetfeldquelle und einer Torsionswaage als Kraftmesssystem genutzt. Dieses System - **Super**conducting High-precision **Lo**rentz **Fo**rce Measurement **S**ystem (Super-LOFOS) - wurde dann erfolgreich aufgebaut und getestet.

Die Neuerung des Super-LOFOS besteht in der integrierten Kühlung von Bulk-HTS und KMS sowie im modularen Aufbau. Die integrierte Kühlung löst das bisherige Problem der Beschränkung und des Einflusses der Magnetsystemmasse der bisherigen LKA-Systeme und gewährleistet eine berührungslose Kühlung des KMS.

Die integrierte Kühlung des Super-LOFOS wurde experimentell getestet. Bei Kühlung mit flüssigem Stickstoff bzw. Helium werden auf der Stirnfläche des Super-LOFOS magnetische Flußdichten von $B_T = 100\,\mathrm{mT}$ bzw. $B_T = 1{,}2\,\mathrm{T}$ erzeugt. Weitere Super-LOFOS-Experimente zeigen, wie kryogene Temperaturen und die Magnetisierung die Funktionalität des KMS beeinflussen. Bei einer Neukonzeption des Super-LOFOS sollten insbesondere die optoelektronische Positionsmessung bei kryogenen Temperaturen und Magnetfeldern $> 1\,\mathrm{T}$ abgesichert sein, sowie das KMS beim Magnetisieren des Bulk-HTS ausreichend starr fixiert werden können.

Damit erweitert die vorliegende Arbeit die Einsetzbarkeit der LKA für gering elektrisch leitende und langsam strömende Fluide auf $(\sigma \cdot u) = (1\text{-}10)\,\mathrm{S\,s^{-1}}$, sowie macht hochpräzise Kraftmessungen bis $1\,\mathrm{nN}$ unter kryogenen Bedingungen möglich. Darüber hinaus stellt das entwickelte Messsystem Super-LOFOS einen tragbaren Magnetfeldgenerator dar, der für NMR- und MRT-Technologien, Drug Targeting, und magnetische Trennungsverfahren einsetzbar ist.

Abstract

Lorentz Force Velocimetry (LFV) is a technique to measure the velocity of electrically conducting fluids. The advantage of LFV is that this non-invasive measurement method is particularly well suited for use on hot and opaque liquids as well as aggressive electrolytes. LFV for saline water - the model electrolyte - was successfully demonstrated using permanent magnet (PM) configurations without an iron yoke magnetic flux guide, but with targeted magnetic flux guidance (Halbach-array) and a high-precision force measurement system (FMS) based on interferometric measurements of magnet system (MS) deflection and electromagnetic force compensation balance.

Still, PMs are limited with regard to the surface magnetic flux density to $0.5\,\mathrm{T}$, despite using the strongest currently available PM compound (Nd-Fe-B), and a mass of $1\,\mathrm{kg}$ due to the FMS specifications. In the LFV experiments, PMs were placed at $3\,\mathrm{mm}$ distance to the flowing saline water, thereby achieving an effective interaction of the generated magnetic field with the flowing saline water. In the case of hot and aggressive electrolytes (e.g. acids, lyes, molten salts, and glass melts) placing a PM close to the flow channel is not possible due to the thick insulation walls. The electrical conductivity of these electrolytes are $\sigma < 10\,\mathrm{S\,m^{-1}}$ and their inherent flow velocities are $u < 1\,\mathrm{m\,s^{-1}}$.

To extend the LFV for weakly conductive electrolytes, it is required to generate a magnetic field over $1\,\mathrm{T}$. A bulk high-temperature superconductor (HTS) can generate the magnetic field of several teslas and therefore can significantly enhance LFV performance, replacing previously used PMs.

This thesis aims to integrate the bulk HTS into the LFV considering the critical links between the functionality of bulk HTSs and the FMS with the end goal to design, manufacture, and test a novel LFV system using bulk HTS.

How bulk HTSs can be implemented into the LFV and which challenges are accompanied by this was experimentally investigated. Initially, the bulk HTS feasibility for the LFV application was demonstrated, for the first time, using a simplified liquid nitrogen cooling. In addition to the experiment, a 3D numerical model as a fast and accurate tool was developed to calculate the necessary trapped magnetic flux densities B_T for LFV measurements of the model electrolyte with $(\sigma \cdot u) = 10\,\mathrm{S\,s^{-1}}$.

The obtained results were used to develop a novel LFV system using bulk HTS as magnetic field generator and a torsion balance as FMS. This LFV system - **Super**conducting High-precision **Lo**rentz **Fo**rce Measurement **S**ystem (Super-LOFOS) - was then successfully designed, manufactured, and tested.

The Super-LOFOS novelty lies in using an integrated cooling for the bulk HTS and FMS as well as in the modular cryostat structure. Using integrated cooling solved the FMS mass limitation to carry the bulk HTS magnet system. Furthermore, integrated cooling enabled for contact-free refrigeration of bulk HTS and FMS, thereby excluding FMS constrains due to the direct thermal coupling. The modular cryostat structure allowed us to use the available facility and makes it possible to adapt future modifications (e.g. alternative cooling solution).

The Super-LOFOS integrated cooling solution was validated experimentally. Using nitrogen and helium cryogenic liquids, the magnetic flux density of $B_T = 100\,\mathrm{mT}$ and $B_T = 1.2\,\mathrm{T}$ were generated at the Super-LOFOS front surface, respectively. Further Super-LOFOS experiments revealed how cryogenic temperatures and magnetization affect the functionality of FMS - an integral part of the Super-LOFOS. For a new Super-LOFOS concept one has to address the opto-electronic position measurement at cryogenic temperature and magnetic field $> 1\,\mathrm{T}$ as well as protect the FMS from magnetic field influence during bulk HTS magnetization.

This thesis also extends the LFV applicability for weakly-conducting and slow-flowing electrolytes $(\sigma \cdot u) = (1\text{-}10)\ \mathrm{S\,s^{-1}}$ as well as enabling high-precision force measurements up to $1\,\mathrm{nN}$ under cryogenic temperatures. Furthermore, the developed Super-LOFOS provides a portable magnetic field generator, which can be used for NMR and MRI technologies, magnetic separation, and drug targeting applications.

Contents

Acknowledgments

I am thankful to the Research Training Group (RTG) №1567 "Lorentz Force Velocimetry and Lorentz Force Eddy Current Testing" within the German Science Foundation, Deutsche Forschungsgemeinschaft (DFG) for funding and allowing me the opportunity to obtain my PhD within this program. A portion of this work was performed at the National High Magnetic Field Laboratory, which is supported by the National Science Foundation Cooperative Agreement No. DMR-1644779 and the State of Florida.

Furthermore, there are several individuals to whom I would like to express my sincere gratitude for their assistance and support:

Dr. Bernd Halbedel, who supervised my research and has been incredibly supportive of my development as a scientist and engineer, afforded me a lot of responsibility, and helped me to rethink the problems as opportunities.

Prof. Thomas Fröhlich for encouraging me to carry out Lorentz force measurement experiments as well as for constructive and stimulating discussions.

Dr. Na Yan, who introduced me to the experimental Lorentz force measurement technique and was continuously supportive throughout our collaborative work to combine the working principles of a torsion balance with a superconductor, acting as trap field magnet.

Dr. Frank Werfel and **Uta Flögel-Delor**, (ATZ®, Torgau) for giving me the wonderful opportunity to perform the high magnetic field tests on bulk superconductors. Especially, I am grateful that I was allowed the freedom to design and conduct experiments independently. Additionally, I want to thank **Renè König**, **Peter Schirrmeister**, and **Viktor Kantarbar** (also ATZ®, Torgau) for their technical support in sample preparation and help during the initial assembly of Super-LOFOS.

Prof. Wei Guo, who hosted and supervised my scientific stay at Florida State University, USA. **Dr. Dima Abraimov**, **Dr. Anatolii Polianski**, and **Van Griffin**, for valuable discussions and their experimental support with high-field measurements in the Applied Superconductivity Center at Florida State University. **Brian Mastarcci**, **Nathaniel Garceau**, and **Hamid Sanavandi** (also of Florida State University) for many fruitful scientific discussions at work and numerous enjoyable social activities after work during my scientific stay abroad.

Dr. Jan Jaroszynski, for his hospitality and day-and-night experimental assistance during the high-field tests at National High Magnetic Field Laboratory in Tallahassee. Furthermore, I would like to say thank-you for the financial support needed to cover the travel expenses.

1 Introduction

1.1 Motivation

The world is making a transition toward the fourth industrial revolution (Industry 4.0), which aims to automate, control, and optimize industrial processes. It is crucial to accurately measure process variables such as temperature, pressure, or flow rate to improve the reliability of accounting for the amount of material and resource usage and consumption, facilitate stricter control of production processes, and ensure energy as well as cost savings.

Flow rate measurements through an opaque wall or in an opaque fluid as well as in hot or chemically aggressive fluids present a technical challenge, since classical flow measurement techniques are restricted or cannot be applied.

LFV was introduced in the framework of the Deutsche Forschungsgemeinschaft DFG funded project Research Training Group (RTG) №1567 "Lorentz Force Velocimetry and Lorentz Force Eddy Current Testing" and has shown significant potential as a non-invasive technique for flow rate measurements in liquid metals, which are highly electrically conductive ($\sigma = 1 \times 10^6 \, \mathrm{S \, m^{-1}}$) as well as hot and agressive fluids [1, 2]. The LFV working principle relies on measuring the force, namely the Lorentz force, that is generated by the relative motion of an electrically conductive fluid through a transversely applied magnetic field. The LFV flowmeter consists of two integral parts: a magnet system (MS) generating a magnetic field in the fluid as well as a FMS carrying this MS and measuring the resulting force.

LFV was successfully used under laboratory and plant conditions for continuous casting of liquid metals such as steel [3], aluminum [4–6], sodium [7], and tin [8]. Using LFV, it was possible to precisely determine, control, and dose the amount of hot molten metal, thereby increasing production quality and reducing energy consumption [5].

LFV was also applied to the flow rate measurement in saline water as a model electrolyte [9–11]. In contrast to liquid metals, electrolytes have a significantly lower electrical conductivity ranging from $1 \, \mathrm{S \, m^{-1}}$ to $100 \, \mathrm{S \, m^{-1}}$ and slow velocity in the range of $0.2 \, \mathrm{m \, s^{-1}}$ to $3 \, \mathrm{m \, s^{-1}}$. Although saline water was used as a model fluid, LFV technol-

ogy is promising for applications on aggressive electrolytes such as acids, lyes, molten salts, and glass melts, where direct flow rate measurements during the production process have received scant attention due to the harsh process conditions. For instance, in the case of glass melts, process control is realized via model-based *in-situ* temperature measurements [12–14] or by determining the weight of the final product [15].

Transitioning LFV from liquid metals to electrolytes required using a high-precision ($>1\,\mu N$) FMS based on interferometric measurements of MS deflection and electromagnetic force compensation balance as well as Halbach-array PM system [11, 16] with targeted magnetic flux guidance. A concern, however, is that a PM has two limitations: the first is that even the strongest available Nd-Fe-B PMs provide a limited magnetic field up to $0.5\,T$ [17], the second is a mass constraint of $1\,kg$ imposed by the FMS [18]. In LFV experiments the PMs were placed at $3\,mm$ distance to the flowing saline water, thereby providing effective interaction of the magnetic flux density with the flow volume. However, in the case of aggressive electrolytes (e.g. glass melts), the realization of close magnetic interaction with the fluid is not possible due to the large isolation walls and slow flow velocity of such fluids ($\ll 1\,m\,s^{-1}$) [19]. Therefore, pragmatic improvements are required:

1) use a stronger magnetic field source with magnetic flux densities over $0.5\,T$,

2) deploy a novel FMS with a force measurement resolution below $1\,\mu N$.

A bulk HTS can generate a magnetic field which is one order of magnitude stronger than a PM [20, 21] and therefore is a suitable candidate to improve LFV performance. However, the use of bulk HTS is underpinned by the cryogenic cooling, vacuum, and magnetization technology, which must also comply with the FMS (another integral part of the LFV system). A new FMS based on torsion balancing was developed in a parallel Ph.D. work by Na Yan [22] and achieved the force measurements resolution of $2\,nN$ at room temeprature (RT).

1.2 Thesis aims and layout

The main purpose of this dissertation is to integrate bulk HTS into the LFV experimental setup considering requirements regarding cooling and magnetization as well as predict the critical links between the functionality of bulk HTSs and the FMS with the end goal to design, manufacture, and implement a novel and improved LFV system for application on low-conducting and slow-flowing electrolytes.

Chapter 2 explains how bulk HTS can be used as a strong magnetic field source and which challenges are accompanied by this. It also discusses the recent technological achievements and challenges of current bulk HTS applications.

Chapter 3 introduces LFV including the fundamentals and the achieved state of the art. This chapter also describes how LFV has evolved over the three RTG phases and how bulk HTS can be used to increase LFV performance.

Chapter 4 presents, for the first time, the experimental proof-of-principle of using bulk HTSs for the LFV application. In addition to the experiment, a 3D numerical model was developed as a fast and accurate tool to predict the LFV performance.

Chapters 5-6 contain the major part of this work, focusing on designing and manufacturing a novel LFV system using bulk HTS, which is called Super-LOFOS. The main issues regarding Super-LOFOS requirements, assembling, and implementation tests are discussed in detail.

Chapter 7 summarizes the obtained results and provides recommendations for future scientific development and research.

2 Strong and compact magnetic sources

2.1 Superconductivity: history and basic definitions

2.1.1 Discovery of superconductivity

In the year 1908, Heike Kamerlingh Onnes was the first person able to liquefy helium, spurring intense investigations on electrical properties of materials in the newly accessible low-temperature range[1]. The most remarkable finding of Leiden's laboratory appeared in 1911, when Onnes[2] and his co-workers observed that the dc resistance of an ultrapure mercury wire vanished at about $4.2\,\mathrm{K}$ to a value below the resolution of the measuring device [25]. It was noteworthy that the resistance vanished abruptly as the temperature was lowered, rather than monotonically approaching zero. This fact implies that the sample undergoes a new extraordinary state, which Onnes called *Superconductivity*. The temperature at which the transition to superconductivity emerges is termed the *critical temperature*, T_c.

In successive experiments, the Leiden group also found other metal elements to be superconducting. Moreover, it was observed that very high currents can pass through the sample until a certain current density value [25], which nowadays is termed as *critical current density*, j_c. Onnes demonstrated that a persistent current flows in the closed-loop coil as long as it remains below its T_c. Therefore, Onnes aspired to design a very powerful magnet that can generate magnetic fields of $10\,\mathrm{T}$ [23]. However, this plan failed due to the loss of the superconductivity at fields less than $50\,\mathrm{mT}$ [26]. Continued investigations [27] at Onnes's laboratory revealed that superconductivity in pure metals suddenly disrupted when an external magnetic field reaches certain value - *critical magnetic field B_c*.

---

[1]Helium is liquefied at about 4.2 K, however Onnes was able to extend temperature range down to 1.7 K by reducing the vapor pressure of the helium bath [23].

[2]In 1913, H. K. Onnes received Nobel prize "for his investigations on the properties of matter at low temperatures which led, inter alia, to the production of liquid helium" [24].

2.1.2 Importance of magnetic properties

Meissner effect. It was believed that the superconductor is a 'perfect conductor' and its properties are defined only by the disappearance of the dc resistance below the critical temperature. Meissner and Ochsenfeld [28] observed that when a superconducting bulk is cooled below its T_c in a magnetic field, it expels the magnetic flux. Figure 2.1a) illustrates their observation - *Meissner effect* - using a field-dependent *magnetic polarization*, J:

$$J = B_A - B_{in}, \tag{2.1}$$

where B_A is the *applied magnetic flux density* and B_{in} - *internal magnetic flux density* in the superconductor. The polarization is equal and opposite to B_A up to the critical magnetic field, B_C (this also means $B_{in} = 0$). For larger fields, superconductivity disrupts and the sample returns to the normal conductive state. For instance, the metallic element lead (Pb) exhibits the Meissner behavior with the critical magnetic field of $B_c = 0.05\,\text{T}$ (see Figure 2.1 a) [29].
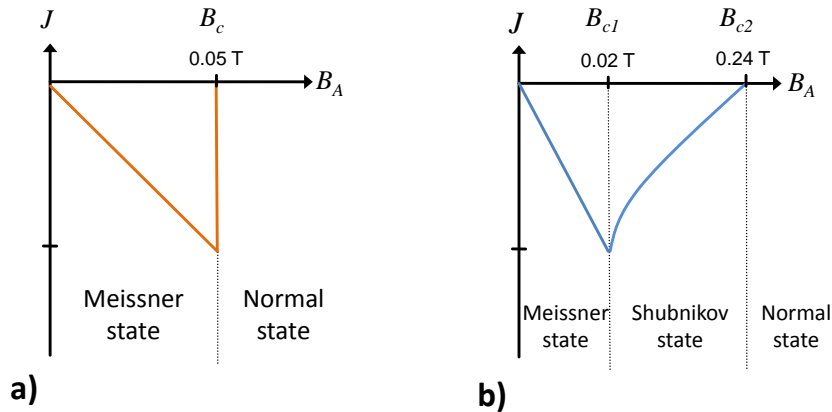
Figure 2.1: Field-dependent polarization of the superconductors at $4.2\,\text{K}$ as a function of the applied magnetic filed: **a)** - Type I superconductors (pure Pb); **b)** - Type II superconductors (PbIn alloy). Data of critical fields are used from [29].

Shubnikov's experiments. Since then, great experimental and theoretical efforts were devoted to studying the magnetic properties of continuously emerging superconducting metals and alloys. In this context, the most prominent experimental work was performed by Shubnikov *et al* [30, 31] in preparing ultra-pure specimens[3] and

---

[3]Shubnikov group prepared single-crystal metals and single crystals of single-phase alloys Pb-Tl and Pb-In of high quality, e.g. without defects [30, 31].

precisely controlling the alloying [32], which enabled them to identify a new magnetic state where the superconductivity preserves at the magnetic field.

Figure 2.1 b) shows the magnetic behavior of a ultra-pure alloy (for example Pb-In): the magnetic flux is zero in the interior of the sample until a *first critical magnetic field*, B_{c1}. Then, a certain portion of the magnetic flux density penetrates the sample and magnetization monotonically decreases as the field is applied, before reaching a *second critical magnetic field*, B_{c2}, above which the superconductivity vanishes. Shubnikov *et al* concluded that an alloy behaves quite differently in comparison to a metal element, for example, lead.

Today, the field interval $B_{c1} < B_A < B_{c2}$ is called *mixed* or *Shubnikov* state, but V. Ginzburg mentioned[4] that Shubnikov's experiments were "a factual discovery of Type II superconductors" [33].

2.1.3 Type II superconductors

Much later, a partial interpretation of Shubnikov's experimental results was provided by Abrikosov[5] [29], who discerned that based on the Ginzburg-Landau theory [34, 35] all superconductors can be divided into two types, depending on the ratio:

$$\kappa = \lambda_p/\xi \tag{2.2}$$

where κ is the *Ginzburg-Landau parameter*, λ_p is the *penetration depth* of the magnetic field and ξ is the *coherence length* between electrons in Cooper pair. It should be stressed that κ depends on the sign and value of the surface energy σ_{ns} at the interface between normal and superconducting state. The threshold value used for superconductor classification is as follows [34, 35]:

$$\kappa = 1/\sqrt{2}. \tag{2.3}$$

Thus, for *Type I superconductors* $\kappa < 1/\sqrt{2}$ and the surface energy is positive. In case of *Type II superconductors*, $\kappa > 1/\sqrt{2}$ and $\sigma_{ns} < 0$. As a rule, Type I superconductors are pure metallic materials, whereas Type II superconductors are metallic alloys or other complex matter.

However, a remarkable insight of Abrikosov's work was a detailed elaboration of

---

[4]V. Ginzburg, who shared a Nobel prize together with A. Abrikosov and A. Leggett in 2003, explained Shubnikov's contribution at Conference in 2004 [33].

[5]In 2003, A. Abrikosov received Nobel prize "for pioneering contributions to the theory of superconductors and superfluids" [24].

the magnetic properties for defect-free Type II bulk superconductors. Author deduced that for the Shubnikov state the magnetic flux density penetrates in to the interior of the superconductor in a form of *quantized vortices*. Figure 2.2 a) shows the schematic of an isolated Abrikosov vortex in an isotropic superconducting material. Each vortex consists of a *supercurrent loop* with an effective radius of λ_p, surrounding a *normal filament* with a radius of ξ, which confines a quantum of the magnetic flux:

$$\Phi_0 = \frac{h_p}{2e} \;=\; 2.1 \times 10^{-15}\,\mathrm{T\,m^2}, \tag{2.4}$$

where h_p and e are fundamental physical constants - the Planck constant and the electron charge, respectively. The magnetic flux density is maximum within the normal filament and exponentially decreases with distance, as sketched in Figure 2.2 b).
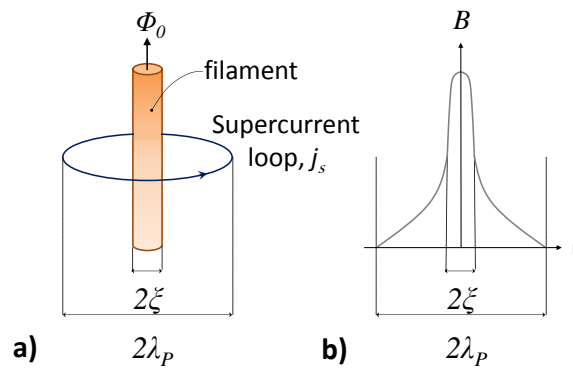
Figure 2.2: **a)** Schematic representation of an isolated Abrikosov vortex in an isotropic superconductor. Φ_0 is quantum of the magnetic flux, λ_p is the penetration depth of magnetic field and ξ is the coherence length. **b)** Distribution of the magnetic flux density B within the vortex.

2.1.3.1 Phase diagram of Type II superconductors

Figure 2.3 shows a field-temperature phase diagram of the Type II superconductors. It comprises a Meissner phase, where the magnetic field is fully expelled from the bulk superconductor at low applied magnetic fields $B_A < B_{c1}$. Above B_{c1}, a magnetic flux density penetrates the superconductor in a form of the Abrikosov vortices: each one confines a quantum of the magnetic flux, Φ_0 (see Eq. 2.4). With a further increase of B_A, the number of vortices n also increases, determining an internal magnetic flux density:

$$B_{in} = n \cdot \Phi_0. \tag{2.5}$$

Finally, when B_A approaches B_{c2}, the vortex nearest-neighbor separation becomes less than 2ξ. This means that the superconducting region between vortex filaments vanishes and the superconductor returns the normal state.

Figure 2.3: Phase diagram of Type II superconductor in $B - T$ coordinates, where B_{c1} and B_{c2} is first and second critical field, respectively, T_c is a critical temperature, B_A is an applied field, and B_{irr} is a irreversibility field.

Note, Abrikosov considered the mixed state in a context of an equilibrium: the distribution of vortices complies with a uniform internal field. Thus, in order to achieve a uniform B_{in}, vortices distribute themselves in a regular lattice called th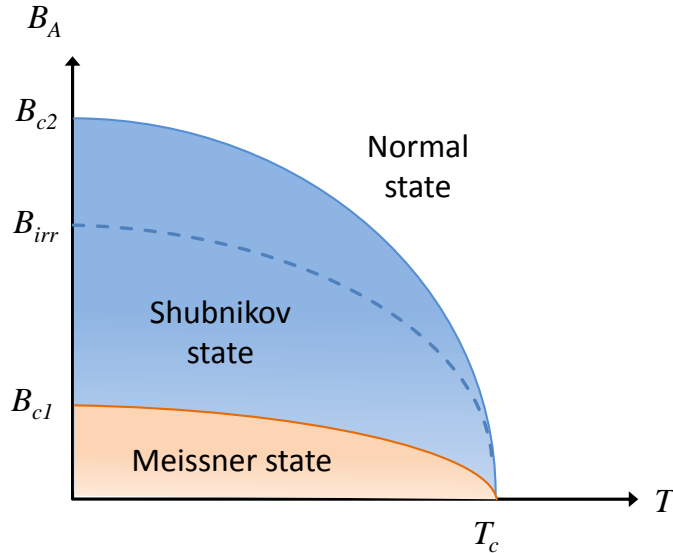e *vortex lattice* due to the repulsive interaction between each vortex supercurrent and the magnetic field induced by other vortex supercurrents [36]. The vortex distribution, in particular, has been confirmed by various experimental techniques. For example, Figure 2.4a) shows the vortex lattice of the ultra-pure NbSe$_2$ single crystal at $4.0\,\mathrm{K}$ for applied field of $0.1\,\mathrm{mT}$ and $0.3\,\mathrm{mT}$ obtained by magneto-optical imaging [37]. The evidence clearly indicates that separation of the vortex lattice is inversely proportional to the applied field.

In general, any variation of the magnetic flux within a superconductor is accompanied by energy loss. Fortunately, the flux pinning (e.g. interaction of the Abrikosov vortices with imperfections/defects in a superconductor) can resist this motion and sustain an induced current, j_c without loss. However, j_c depends on the applied flux density B_A and the temperature T. Thus, when the induced current density exceeds the j_c, the vortex lattice (or part of it) begins to move, thereby inducing losses [38]. The magnetic field value at which $j > j_c$ is called the *irreversibility field* B_{irr} and gen-
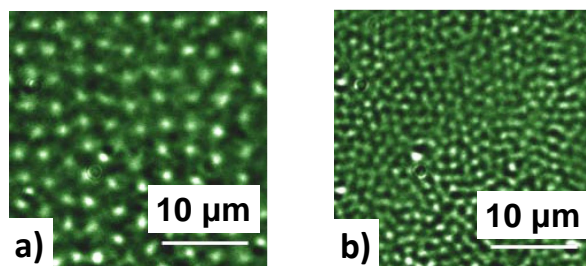
Figure 2.4: **a)** Magneto-optical images of vortex lattices in a NbSe$_2$ single crystal at 4.0 K under field cooling condition: **a)** $B_A = 0.1\,\mathrm{mT}$ and **b)** $B_A = 0.3\,\mathrm{mT}$ [37].

erally increases with decreasing temperature [39]. B_{irr} at given temperature presents so-called *irreversibility line* $B_{irr} - T$ (schematically delineated in Figure 2.3), which determines the upper limit of magnetic or current currying applications.

2.1.3.2 Irreversible magnetic behavior and field trapping

The vortex motion, which arises as a result of the equilibration process or varying of the applied field, is driven by the Lorentz force:

$$\vec{f_L} = \vec{j} \times n \cdot \Phi_0 = \vec{j} \times \vec{B}, \tag{2.6}$$

where $\vec{j}$ is the induced current density, which is perpendicular to the applied magnetic field $\vec{B}$. If there is no restraining force, vortices move unimpeded through the sample generating a *flux flow* resistance [40]. Moreover, after the applied field is removed, vortices also leave the sample and no magnetic flux density remains therein. Such a scenario occurs only in defect-free specimens. Accordingly, one expects a reversible magnetic behavior. For instance, an ultra-pure Nb-Ta alloy exhibits the reversible magnetic polarization $\vec{J}$ [41], shown in Figure 2.5.

However, the polarization of the Nb-Ta alloy that contains some distortions in the crystal structure[6] becomes irreversible: Figure 2.5 compares both cases. The irreversible behavior of the latter sample is a consequence of the interaction of vortices with crystal distortions.

At first, the higher applied field is required to let vortices penetrate the sample: thus, the polarization of distorted Nb-Ta alloy has a lower minimum. Secondly, positive polarization even when the applied field B_A is completely removed indicates that a certain portion of the magnetic flux density is trapped at the crystal distortions, which

---

[6]The distortions in the crystal structure appear, in general, as a results of processing.
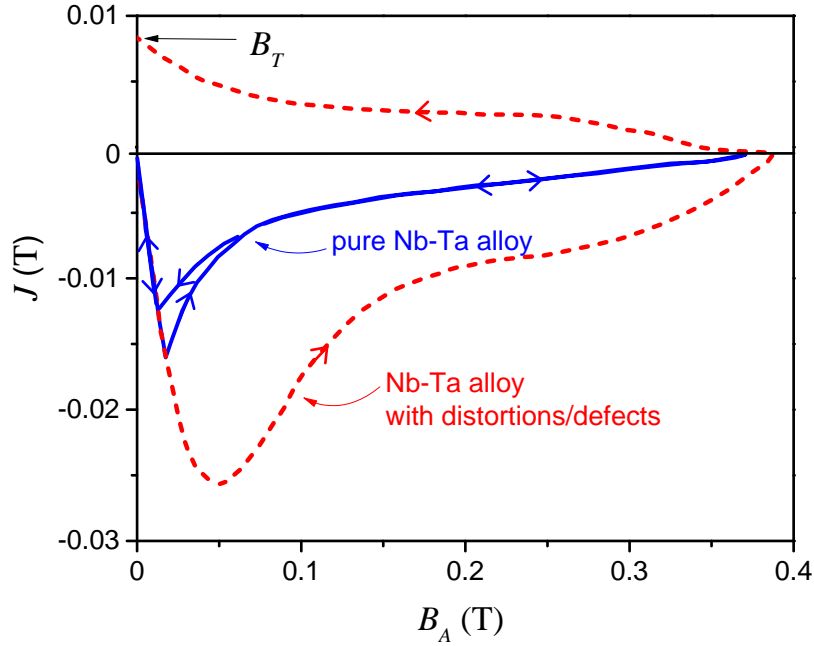
Figure 2.5: Magnetic polarization J of the ultra-pure Nb-Ta alloy (solid line) and Nb-Ta alloy with distortions (dashed line) as function of an appplied magnetic flux density B_A. Data is reproduced from [41].

act as *pinning centers*. This trapped magnetic flux density hereinafter is referred to as *trapped field B_T*.

2.1.3.3 Critical state models

The irreversible magnetic behavior and trapped magnetic fields were also observed in many other experiments on Type II superconductors. It inspired Bean [42, 43] to propose a model which provides a phemenological understanding of such experimental findings. Bean made several assumptions:

1) critical current density j_c flows in a macroscopic region of the superconductor, where the penetrated field is presented,

2) this critical current density is independent of the applied field,

3) in regions without the penetrated field $j_c = 0$,

4) it considers only the Shubnikov state disregarding the B_{c1} and the Meissner state,

5) superconductor has the magnetic permeability of free space μ_0.

Thus, the magnetic behavior of a Type II superconductor in an alternating magnetic field can be described using the Maxwell relation (Ampere's Law), where critical current density j_c and magnetic field B are coupled as follows:

$$\nabla \times \vec{B} = \mu_0 \cdot \vec{j_c}. \tag{2.7}$$

Accordingly, $\vec{B}$ and $\vec{j_c}$ are mutually perpendicular and either one can be determined knowing the value of the other. In one-dimensional cylindrical coordinates, Eq. 2.7 simplifies to

$$\frac{dB}{dr} = \mu_0 \cdot {}^\theta j_c \tag{2.8}$$

In a case of an infinitely long cylindrical superconductor with the radius R the integration of Eq. 2.8 gives the maximum value of the trapped field along the z-axis:

$$B_{max}^z = \mu_0 \cdot {}^\theta j_c R. \tag{2.9}$$

This field is called a *full penetration field B_p*.

Figure 2.6 illustrates the emblematic example of the magnetic flux density and the current density profiles upon the gradually alternating applied field:

a) with the increasing of the applied field B_A, internal field B_{in} (see Eq. 2.5) penetrates from the superconductor periphery and approaches the center; it has a slope consistent with j_c,

b) at $B_A = B_p$, B_{in} reaches the superconductor center,

c) larger B_A leads to further increase of B_{in},

d) upon removal of B_A, B_{in} is inverted and the current changes its sign.

At $B_A = 0$, certain portion of B_{in} with a characteristic triangular distribution remains in the superconductor.

In summary, Bean model is the simple and convenient way to describe the electromagnetic behavior of Type II superconductors. It has been successfully applied by many researchers to interpret their experimental data, though it has several limitations:

1) Bean model does not consider the Meissner state,

2) it does not explain the microscopic origin of pinning and it disregards effect of flux creep (vortex flux motion caused by thermal activation),
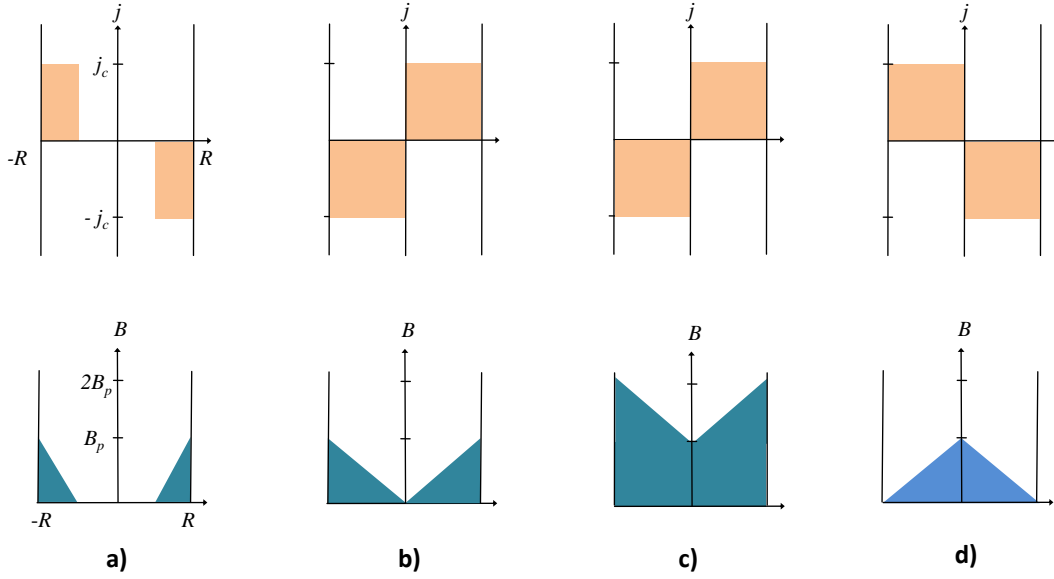
Figure 2.6: The current density (top) and magnetic flux density (bottom) profiles upon the gradually alternating applied field: **a)** as the applied field B_A increases, internal field B_{in} (see Eq. 2.5) penetrates from the superconductor periphery and approaches the center, it has a slope consistent with j_c. **b)** at $B_A = B_p$, B_{in} reaches the superconductor center. **c)** larger B_A leads to further increase of B_{in}. **d)** upon removal of B_A, B_{in} is inverted and the current changes its sign. At $B_A = 0$, certain portion of B_{in} with a characteristic triangular distribution remains in the superconductor.

   3) it assumes a constant j_c, although j_c strongly depends on the applied magnetic flux density B_A.

More realistic models of the magnetic behavior of a Type-II superconductor consider j_c, including its strong dependence on a magnetic field and temperature [44–46]. Hence, based on experimental observations, Kim *et al* [46] proposed an empirical equation:

$$j_c(B) = \frac{j_{c0}}{1 + \frac{B}{B_0}},\tag{2.10}$$

where j_{c0} is the magnitude of critical current density without an applied magnetic field, and B_0 is the magnetic flux density when j_c reduces to half of j_{c0}. The modification of Eq. 2.10 considering temperature dependence can be expressed as:

$$j_c(B, T) = \frac{j_{c0}(T)}{(1 + \frac{B}{B_0})^{\beta}},\tag{2.11}$$

where T is the temperature and β is a material-dependent constant [44].

The material-dependent constants can be estimated using the trapped field profile of the bulk or by fitting the experimental $j_c(B, T)$ curves, which must be measured from a small sub-sample of the bulk superconductor. Although the latter approach delivers accurate data of $j_c(B, T)$ and allows for more precise prediction of the bulk superconductor magnetic performance, experimental efforts as well experimental equipment needed are greatly increased.

2.1.4　High-temperature superconductors (HTSs) and their application

High-temperature superconductors.　The industrial application of superconductors still had a barrier: the superconducting characteristic, such as $[T_c, j_c, B_{c2}]$ required a liquid helium as coolant and a complex fabrication technology. In this sense, only niobium-based alloys with critical temperature up to $T_c = 18\,\mathrm{K}$ [36] were considered for a solenoid design due to the relatively high value of $B_{c2} = 22\,\mathrm{T}$ at $4.2\,\mathrm{K}$. Actually, Kunzler *et al* [47] demonstrated that superconductivity in Nb_3Sn is preserved under $j_c = 100\,\mathrm{A\,m^{-2}}$ at $8.8\,\mathrm{T}$ and $4.2\,\mathrm{K}$. Later, niobium-based superconductors will find their niche for various types of solenoid designs, for instance NMR [48] and fusion magnets [49, 50].

The landmark publication of Alex Müller and Georg Bednorz[7] [51] drastically changed the development of superconductive science and technology. Müller and Bednorz synthesized a ceramic perovskite of Ba-La-Cu-O to be superconducting at $35\,\mathrm{K}$. This work triggered worldwide enthusiasm for research on copper-containing oxides with the aim to raise the critical temperature. Thus, the groups of Paul Chu at the University of Houston and Maw-Kuen Wu at the University of Alabama at Huntsville obtained T_c of $52\,\mathrm{K}$ for Ba-La-Cu-O by applying an external pressure. The most remarkable experimental results were obtained by the Houston group when they "pressurized" the sample internally by substituting yttrium for lanthanum, achieving superconductivity at about $92\,\mathrm{K}$. This allows the use of the liquid nitrogen (LN_2) for cooling, which is far less expensive and also less complicated than the use of the liquid helium. Later, other copper-containing oxides containing Bi, Tl or Hg were found to superconduct with a record of $134\,\mathrm{K}$ in Hg-Ba-Ca-Cu-O at ambient pressure and $164\,\mathrm{K}$ at $30\,\mathrm{GPa}$ [52, 53].

Scientists are keen on developing a superconductor, which functions well at room temeprature (RT), however we are still waiting for the breakthrough research, although

---

[7]In 1987, A. Müller and G. Bednorz received Nobel prize "for their important break-through in the discovery of superconductivity in ceramic materials" [24]
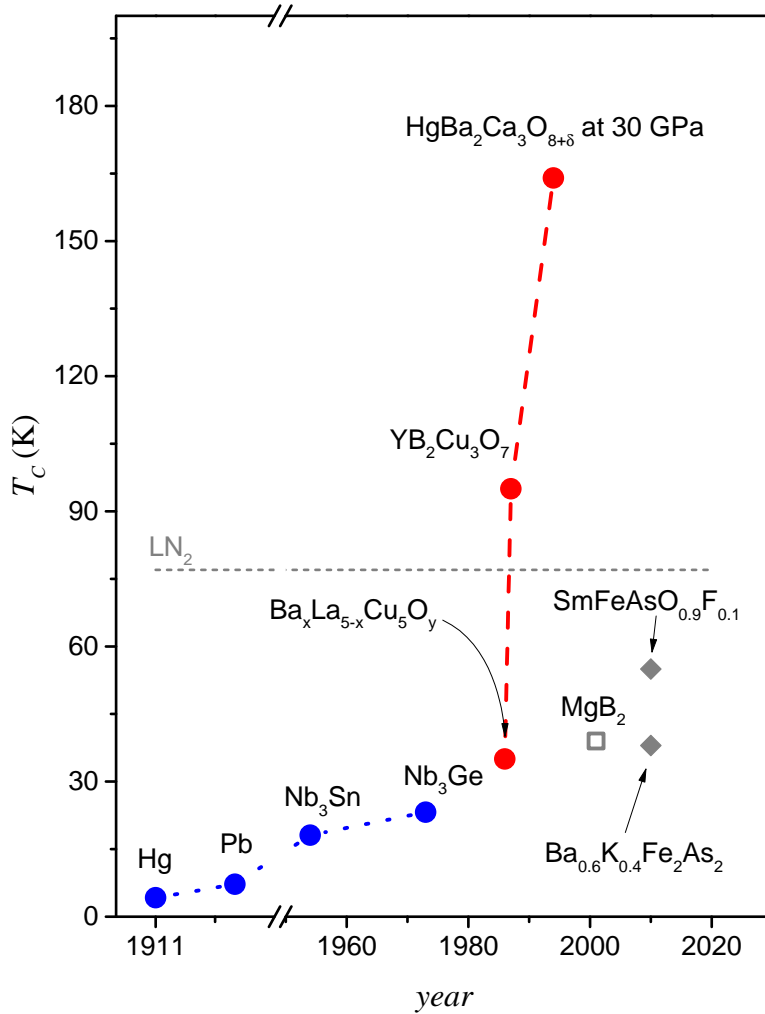
Figure 2.7: Evolution of the T_c for selected superconductors. Dashed arrow is guide for eyes. Data are collected from [36, 40].

a few exotic discoveries are being made on the way there, such as metallic hydrogen [54]. Nevertheless, in the superconductivity community a material that superconducts at temperatures higher than LN$_2$ temperatures is referred to as *high-temperature super-conductor (HTS)*.

An impressive leap of the the critical temperature for selected copper-containing oxides is illustrated in Figure 2.7. It also compares how the T_c has evolved among other technically important superconductors[8]. Of these, iron-pnictides, for example, Sm-Fe-As-(OF) or (Ba-K)-Fe-As have been considered for a applications using magnetic fields due to their high critical fields, low anisotropy, and large grain boundary angle to sustain high j_c [55, 56]. However, commercial manufacture of iron-pnictides

---

[8]Extended compilation of superconductors and their T_c can be found in [36, 40].

is currently not available.

Remarkably, the unexpected discovery of superconducting MgB_2 with $T_c = 39\,K$ appears to offer an alternative to Nb-based and copper-containing oxide systems due to its simple and inexpensive fabrication [57]. Furthermore, the availability of MgB_2 in the form of multifilamentary round wire is promising for companies which manufacture cables. For example, industrial developments of MgB_2 applications are summarized in [58].

Application of HTSs.   The emergence of HTSs, especially the copper-containing oxides, encourages engineers and scientists to study the fundamental physical aspects as well as explore the practical applications. Developing commercially profitable HTS systems and devices greatly motivates further research, which in turn introduces the principles of superconductivity to various fields of applications. High-speed electronics, logic, microwave circuits, and generators are just a few examples of applications incorporating thin film HTS technology. Please also refer to the textbooks [36, 40, 41, 59] for further examples.

Using HTSs technology to develop high-field solenoids and manufacture power transmission cables are still the main applications, which is why HTS must be provided as wires and tapes. Since copper-containing oxides are ceramic, a major difficulty lies in the manufacturing of a long-length and flexible wire or tape from this brittle material.

Apart from being researched under laboratory conditions, the currently most profitable industrial markets for superconductor-based solenoids and transmission cables (mainly Y-Ba-Cu-O and Bi-Sr-Ca-Cu-O) are health care, particle accelerators, and fusion and power transmission. Please also refer to [26, 40, 60] for more information on wire and tape fabrication as well as other engineering aspects.

2.2 Trapped Field Magnet (TFM)

2.2.1 Introduction

Though being somewhat in the shadow of long-length superconductors, bulk HTSs found their own market across magnetic-force-based applications [61, 62]. In particular, these applications owe the remarkable progress in material fabrication and readiness of ancillary technologies, e.g. refrigeration, vacuum, and magnetization. Among superconductors available in a bulk form, the light rare-earth LRE-Ba-Cu-O (Light rare earth elements (LRE) = Y, Sm, Nd, Gd) promises to be a much better

work material than bismuth compounds or a magnesium diboride [61, 63]. For this dissertation we choose to discuss only the superconductor type Y-Ba-Cu-O, because it is a most studied system.

There is a vast amount of literature available on bulk HTSs and their applications (useful publications are [38, 61, 62, 64–69]). These application are based on following properties:

- *large current-carrying capability and low thermal conductivity* allow for superconducting magnetic-energy storage (SMES) and fault current limiters [61],

- *diamagnetic or hysteretic behavior* allow for magnetic shielding [61, 62], levitation [61, 70], magnetic bearing [61, 64, 65, 71], electrical rotary machines [69], etc.,

- *high field-trapping capability* allow for the portable and strong magnetic field generator, NMR and MRI technologies [62, 72, 73], drug targeting [62], magnetic separation [67], etc.

Recently, Durrell *et al* revised ongoing research and application developments of bulk superconducting technology. Considering a good market and feasibility potential, Durrell *et al* discerned the most relevant applications and discussed the aspects of current and future challenges. These applications are:

- magnetic shielding for high-field equipment,

- ultra-light superconducting rotating machines with high torque,

- portable high-field systems for medical devices,

- portable and compact high-field magnets.

The application using portable and compact high-field magnets revitalizes Onne's idea of strong magnet systems. In fact, the magnetized bulk HTS represents the Onnes's "closed-loop coil"[9] without a directly coupled power supply. After appropriate cooling and magnetization,HTSs can serve as (portable) strong quasi-permanent magnets and are referred to as *Trapped Field Magnets (TFMs)*.

2.2.2 Examples of TFM

Early TFM prototypes were built in Japan. For example, a schematic of a TFM is shown in Figure 2.8 a) [74]. It consists of a Y-Ba-Cu-O bulk, which is encapsulated

---

[9]Note, so far there is no technology to produce a closed-loop coil out of HTS wire/tapes
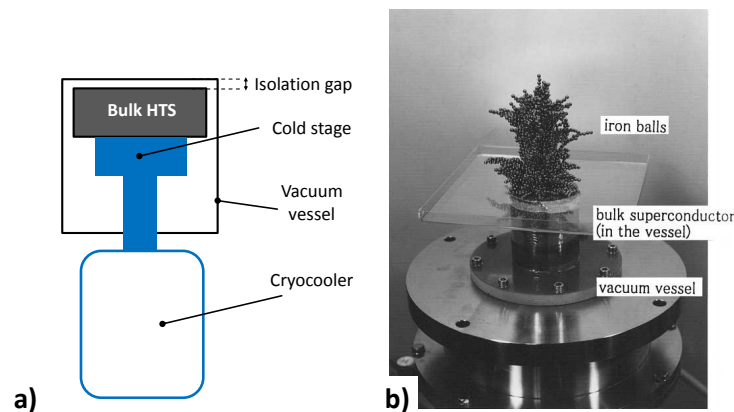
Figure 2.8: TFM system consisting of Y-Ba-Cu-O bulk, vacuum vessel and cryocooler: **a)** Schematic and **b)** photograph [74]. Bulk HTS has diameter of 35 mm and thickness of 14 mm. After the magnetization, trapped field of 0.8 T was generated and attract iron balls.

within the vacuum vessel and is refrigerated by a cryocooler. This TFM generates a field of 0.8 T on the outer surface of the vacuum vessel at 30 K. To demonstrate this, Figure 2.8 b) shows a photograph of the top section of the TFM prototype, where ferromagnetic balls are attracted by the magnetized bulk HTS.

Oka [67] modified TFMs to make them viable for industrial applications. Of these, the largest and most profitable potential industrial use will be for portable [75, 76] or desktop [77, 78] TFMs. Currently, such systems continue to be improved considering various technical aspects:

- enhancement of the trapped magnetic field by improving HTS materials and arrangements,

- miniaturization (volume and mass) of the equipment,

- adopting commercial cooling technology (e.g. cryocooler),

- the developing a compact magnetization system - pulse magnetization.

A brief survey of the recent state-of-the-art TFMs with the main parameters is presented in Table 2.1. In 2009, Saho *et al* [76] developed a portable TFM system and achieved a peak trapped field of 5.2 T outside the vacuum vessel from the 45 mm diameter Gd-Ba-Cu-O bulk. Saho *et al* used a Stirling-cycle cryocooler for cooling below 40 K and quasi-statically magnetized the TFM by applying 6 T from a superconducting solenoid. Later, Yokoyama *et al* [78] reported trapped field of 3 T at the surface

Table 2.1: Comparison of the main parameters for the different portable and desktop TFM.

Parameters/TFM References	portable TFM-I Saho *et al* [76]	portable TFM-II Zhou *et al* [75]	desktop TFM Yokoyama *et al* [78]
Peak B_T, (T) outside vessel	5.2	1.7	1.3
Peak B_T, (T) at bulk surface	7.2	3.0	3.2
Isolation gap, (mm)	2.8	4	3.8
Bulk HTS	Gd-Ba-Cu-O	Gd-Ba-Cu-O	Gd-Ba-Cu-O
Diameter, (mm)	45	60	30
Thickness, (mm)	90	15	12
	stack of bulks	single bulk	single bulk
Cryocooler	Stirling-cycle	Stirling-cycle	Stirling-cycle
Operating T, (K)	36	51	55.6
Magnetization	static	single-pulsed	multi-pulsed
Mass, (kg)	9.5 (w/o compressor)	n.k.	26

of the 60 mm diameter Gd-Ba-Cu-O bulk, yet utilizing a compact Stirling cryocooler (CryoTel® CT, Sunpower Inc.) and a single-pulse pulse field magnetization (PFM). In addition, Zhou *et al* [75] also obtained the peak trapped field of about 3 T using the same type of cryocooler, yet magnetizing a 30 mm diameter Gd-Ba-Cu-O bulk with multi-pulse, multi-temperature PFM [75].

Nevertheless, although high B_T can be reached at the surface of the bulk HTS surface, it rapidly decreases (up to 30-60 %) with distance. Therefore, it is important to ensure the small magnetic distance ("isolation gap", see Figure 2.8 a) when engineering
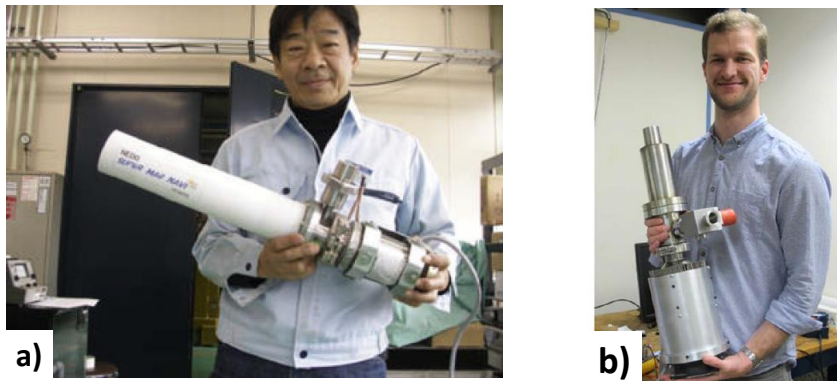

Figure 2.9: Two examples of the portable TFM: **a)** TFM exploiting static magnetization developed by Hitachi [76], **b)** TFM utilizing pulse-field magnetization developed by Cambridge Bulk Superconductivity Group [62, 75].

a vacuum vessel [61].

Figure 2.9 shows examples of two portable TFMs, developed by Saho *et al* [76] and Zhou *et al* [75]: both TFMs are light enough that one person can carry it. Still, while different circumstances have to be considered when comparing those systems to each other, it is immediately clear that TFM establishes a novel type of a magnetic field generator which is drastically different from a permanent magnet or solenoid.

2.2.3 Comparison of magnetic field generators

Figure 2.10 qualitatively compares different magnetic field generators: PM, solenoid, and bulk HTS. The advantages of bulk HTS are outlined with regard to performance and compactness. Here, each field generator is considered in detail.
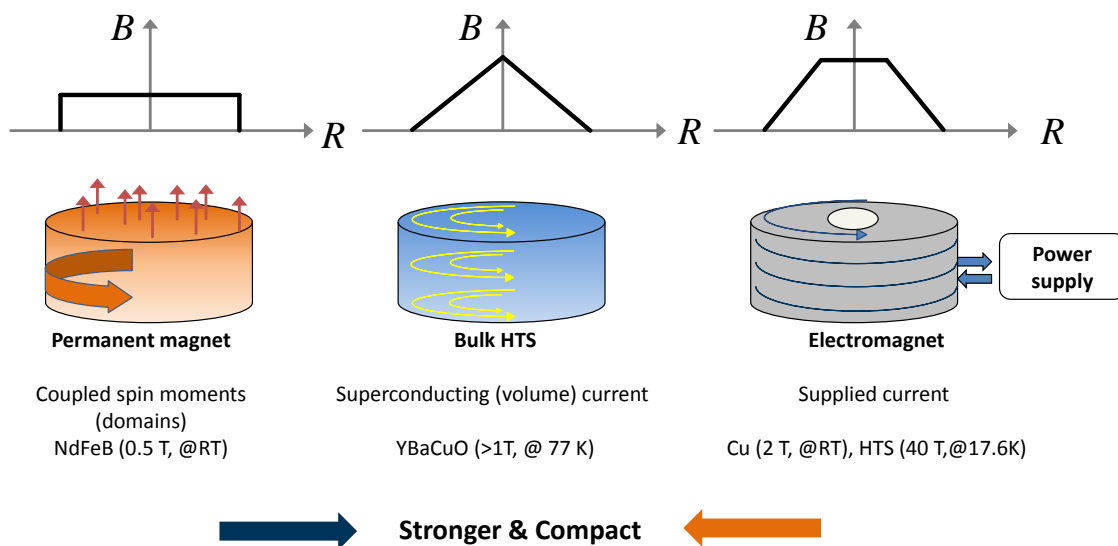

Figure 2.10: Comparison of the magnetic field generators. Graph is adapted from [79].

Permanent magnets (PM).   In case of the permanent magnet (PM), the magnetism is based on domains, which arise due to intrinsic magnetic moments (spins). The magnetism of PM is therefore limited by the atomic properties, which means that the magnetic polarization of PMs is independent of the volume and depends only on material properties.

Usually, large remanent polarization J, high Curie temperature T_{curie} and strong anisotropy field H_A are prerequisites for an ideal permanent magnet. Hence, a large

magnet moments of 3*d*-elements (e.g. Fe, Co) combined with high anisotropy fields of rare-earth elements (e.g. Nd, Dy, Sm) are beneficial for PM production [17, 20]. However, the performance of a magnetized permanent magnet significantly depends on the fabrication process and topological microstructure. One thus characterizes the PM by extrinsic parameters, such as a coercive field $^{J}H_c$, remanence B_r and the energy density $(BH)_{max}$ [17]. So far, RE-Fe-B (RE = Nd, Dy, Pr, where Nd-Fe-B is the most common compound) represents a strongest permanent magnet with:

$$(BH)_{max} \approx 400\,\mathrm{kJ\,m^{-3}}. \tag{2.12}$$

This value, however, approaches the technical limit of this compound [17]:

$$(BH)_{max} \approx 720\,\mathrm{kJ\,m^{-3}}, \tag{2.13}$$

whereas a theoretical limit is:

$$(BH)_{max} \approx 960\,\mathrm{kJ\,m^{-3}}. \tag{2.14}$$

It implies that for even stronger permanent magnets, novel materials with better extrinsic properties are required. However, less progress in the improvement of $(BH)_{max}$ is expected [17] for the near future.

Bulk HTS *vs.* **PM.** The magnetism of bulk HTS originates from the supercurrents circulating macroscopically throughout the sample (see Section 2.1.3). In other words, the bulk HTS operates like a coil: a current, once induced, flows through the length scale of the sample and is equal to the superposition of supercurrents - critical current density, j_c. When bulk HTS is fully magnetized, j_c flows over the entire volume of the sample, producing a characteristic conical distribution of the magnetic flux density. It also means that the bulk HTS polarization increases with the sample volume, which is in contrast to the permanent magnet.

Due to the different origin of the magnetism, it is difficult to compare a permanent magnet and the bulk HTS using intrinsic or extrinsic magnetic parameters. For instance, the volume magnetic polarization J or magnetization M (defined as $M = \mu_0 \times J$) is easy to define for PM, while defining the magnetic moment of a macroscopic current loop for a superconductor is somewhat confusing [39]. It would be more reasonable to compare the factual engineering parameters - surface magnetic flux density of PM and bulk HTS. Hence, off-the-shelf products - Nd-Fe-B permanent magnet

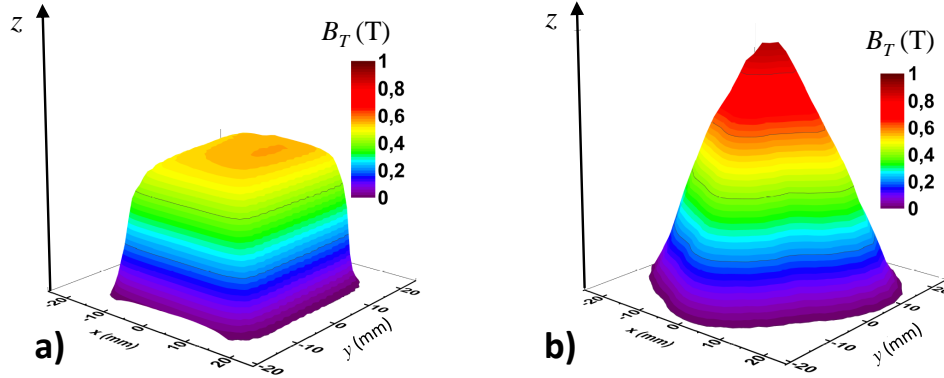(MagnetWorld®, Jena) and Y-Ba-Cu-O bulk HTS (ATZ®, Torgau) - were selected for this purpose.

Figure 2.11: Comparison of the *z*-component surface magnetic flux density B_y for **a)** Nd-Fe-B permanent magnet (MagnetWorld, Jena) and **b)** Y-Ba-Cu-O bulk HTS (ATZ®, Torgau). The activation of the bulk HTS was performed following a field cooling magnetization with $B_A = 1.5\,\text{T}$ at $77\,\text{K}$.

Figure 2.11 presents the B_T magnetic flux density[10] measured 1 mm above the surface of each magnet. Both magnets have comparable dimensions: Nd-Fe-B (N48) is a cube with a side of 30 mm and mass of 200 g, while Y-Ba-Cu-O is a disc with diameter of 46 mm and 60 mm and thickness of 16 mm and 60 mm and mass of 160 g. The bulk HTS was activated following a FC magnetization with $B_A = 1.5\,\text{T}$ at $77\,\text{K}$.

It is immediately clear that the maximum magnetic flux density of the Y-Ba-Cu-O bulk HTS exceeds that of Nd-Fe-B. When appropriately cooled and magnetized, bulk HTS is capable of trapping magnetic fields which are an order of magnitude stronger than those which a PM can provide. (records trapped magnetic fields are debated in Section 2.2.8).

Bulk HTS *vs.* **solenoid.**   In contrast to conventional or superconducting solenoids, bulk HTSs are much more compact and do not require a direct, continuous powering. Furthermore, the generation of a strong magnetic field appears in a free space, unlike being confined within a solenoid bore [62, 68, 80].

Conclusion.   Comparison of permanent magnet, solenoid, and bulk HTS can be summarized when laying out a diagram of the generated field as a function of size and cost [67], as shown in Figure 2.12. Bulk HTSs, acting as TFMs, are advantageous

---

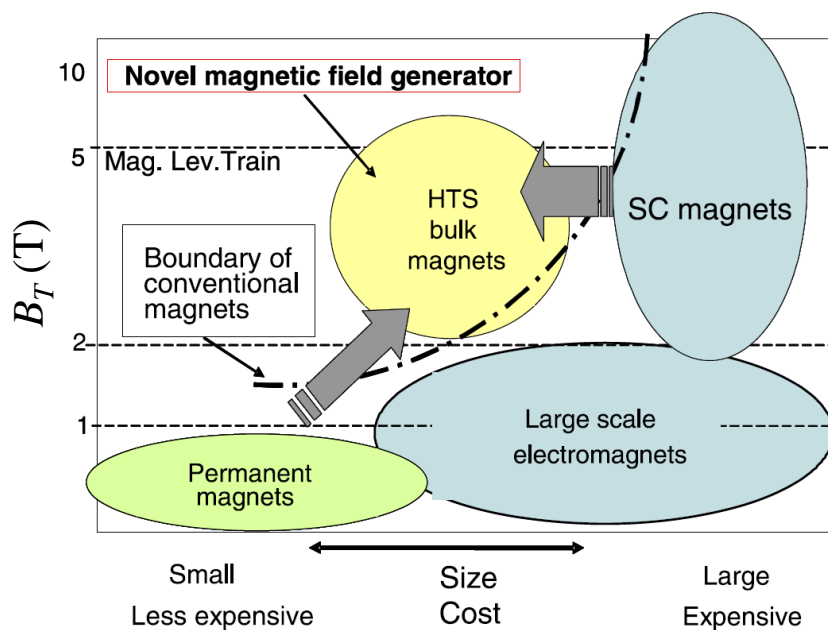[10]Hereafter B_T indicates the B_z - component of vector B

Figure 2.12: Oka's diagram for industrial market position of HTS bulk magnet among other magnetic field generators [67]. Bulk HTSs, acting as TFMs, are advantageous magnet sources over conventional counterparts, if the high field generation, size and cost are prioritized requirements.

magnet sources over convectional counterparts, if the high field generation ($> 1\,\mathrm{T}$), size and cost are prioritized requirements.

2.2.4 Fabrication

In pioneering years, Y-Ba-Cu-O bulk was synthesized using a common ceramic processing called solid state reaction or sintering. However, the polycrystalline materials obtained were of poor quality, because randomly oriented grains within the material limit j_c, which greatly narrows the range of practical applications. The latter fact was disappointing and scaled down ambitions of practical utility. A high j_c flowing in a large current loop is primary requirements for profitable magnetic application using bulk material [63].

A breakthrough in the fabrication of Y-Ba-Cu-O bulk occurred after introducing a melt texturing growth (MTG) [81]. In order to produce Y-Ba-Cu-O the material was melted and then allowed to recrystallize, which still gives us the term "melt-textured" to describe the crystalline structure of Y-Ba-Cu-O as opposed to the structure obtained using metallurgical or ceramic texturing techniques [38]. Later, significant contributions to this process were made by Salama *et al* [82] and Murakami *et al* [83]. Over

the last decades, the MTG underwent a number of modifications and now has many variants. The main goal of all processing methods was to obtain large and well-aligned grains to increase the value of the critical current density j_c.

Today, a large single-grain Y-Ba-Cu-O bulk is produced using a top-seeded melt growth (TSMG) [84], which is outlined in Figure 2.13. This method has been intensevely studied and improved in several research groups: a summary of processing details and properties can be found in [38, 63, 85]. To date, several companies (see Table 2.2) commercially produce standard bulk HTSs with a capacity over 1000 samples per year [62].
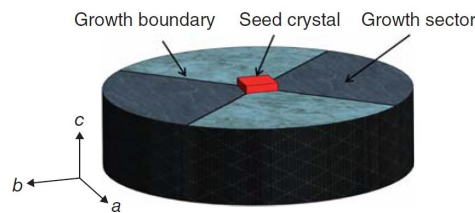

Figure 2.13: Schematic of the top seed melt technique (TSMG) with the delineated location of the seed, grain sectors, and boundaries. Courtesy of F. Werfel [86]

Admittedly, TSMG takes advantage of an extraordinary feature of the Y-Ba-Cu-O material phase diagram [60]. The superconducting $YBa_2Cu_3O_x$ (Y123) phase lies within the non-superconducting Y_2BaCuO_5 (Y211) phase. As a result, the latter composition forms first during the thermal annealing. One could argue that this is a serious drawback. However, the Y211 concentration scales with the critical current density [87]. A Y211 particle is of slightly greater dimension than ξ (radius of the vortex filament), which makes Y211 particles ideally suited to pin the magnetic flux quantum. Still, further refining and homogeneous distribution of Y211 within the Y123 matrix [38] can lead to even better pinning performance due to a short coherence length in Y-Ba-Cu-O. Hence, one introduces Pt or CeO additions to reduce Y211 size [38].

In brief, TSMG comprises two stages: melt-textured growth and oxygenation. At first, a seed is placed on the top of the pressed precursor powders, which are a mixture of the superconducting Y123 phase and non-superconducting Y211 phase. Then, this pressed powder is heated up to the melting points of the powders with subsequent slow cooling with prescribed temperature gradient. The main requirement for the seed is a higher melting point regarding the precursor powder and compatible structural/chemical parameters [88, 89]. In case of Y123, single crystals (or thin films) of Sm123 or Nd123 are used. Figure 2.13 depicts usual TSMG setup with seed, four

growth sectors, and growth boundaries. It is important to align the *c*-axis of the bulk orthogonally to the sample surface. Then, the seed acts as a heterogeneous center and promotes the epitaxial crystallization of a single crystal (single grain). In the following stage, textured bulk is annealed in an oxygen atmosphere: This modifies the oxygen stoichiometry and makes Y-Ba-Cu-O superconducting. The critical temperature of the samples thus obtained varies from 90 K to 93 K depending on various factors, e.g. quality of the precursor powders, melt-processing, and oxygenation.

Meanwhile, other LRE systems attract attention due to better magnetic properties at 77 K [85, 91, 92], although they require additional efforts in fabrication. Thus, Fuchs *et al* [90] compared the trapped field capability of LRE-Ba-Cu-O down to 77 K using B_{irr} as criterion. It is shown in Figure 2.14. When B_A is applied along the bulk *c*-axis, Y-Ba-Cu-O yield a modest $B_{irr} \sim$ 5 T at 77 K, while higher B_{irr} are documented for (Sm,Nd, Gd)-Ba-Cu-O. Still, their fabrication requires an appropriate seed technology [63]. It is important because the use of single crystal seeds like Nd123 or Sm123 is challenging due to the limited temperature window during the melting process. Secondly, an additional control of solid solution formation is needed, because of a substitution of LRE-element with Ba lattice sites and vice versa [38]. Thus, an oxygen controlled melt growth (OCMG) was developed [93, 94] followed by a significant improvement [91, 92] and commercialization by Nippon Steel® [95]. The company
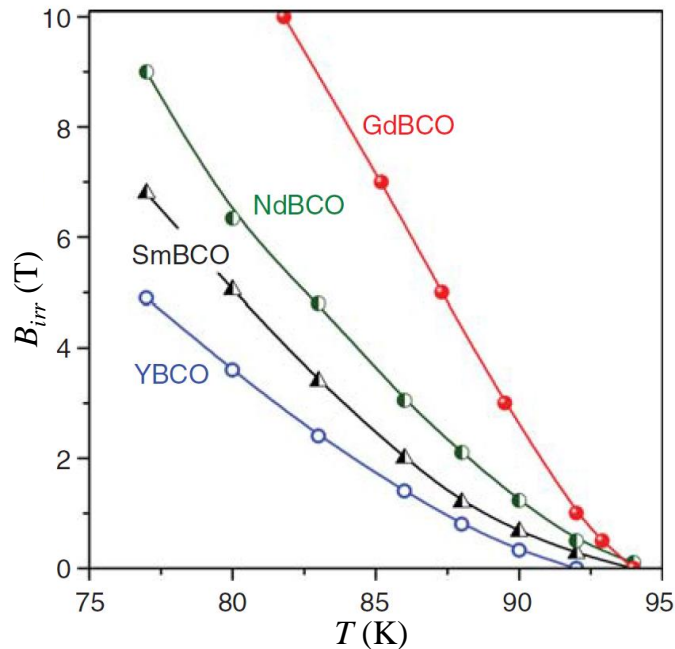

Figure 2.14: The irreversivility field B_{irr} as function of temperature (down to 77 K) for different LRE-Ba-Cu-O systems [90].

Figure 2.15: Photograph of two Gd-Ba-Cu-O bulk discs with diameter of 150 mm and 60 mm
grown using oxygen controlled melt growth (OCMG) by Nippon Steel® [91, 92].

produces large single-grain Y-Ba-Cu-O and Gd-Ba-Cu-O bulks with diameters up to
150 mm. Figure 2.15 shows an example of Gd-Ba-Cu-O bulk discs with diameters of
150 mm and 60 mm [91, 92].

Note, the fabrication of the single-grain LRE-Ba-Cu-O with diameters above 80 mm
demands a material-controlled peritectic temperature gradient to prevent the parasitic
nucleation and an unnecessary grain growth [63]. Since the latter treatment is cost-
and time-consuming, the diameter of a standard LRE-Ba-Cu-O varies from 30 mm to
60 mm. Still, an increase in size of a single-grain bulk HTS does not automatically
lead to the increase of B_T [63, 96] as it is predicted by the Bean formula (see Eq. 2.9).

Nevertheless, the choice of a suitable LRE123 system for large-scale applications
might depend not only on the magnetic properties and the size. Werfel *et al* [61]
and Hlacek *et al* [97] pay attention to the economic factors, considering the prices
for raw materials, their recycling, fabrication time, efforts, and logistics. Therefore,
the Y-Ba-Cu-O system remains preferred for large-scale applications due to its price-
performance ratio. Table 2.2 overviews the price and typical trapped field for off-the-
shelf products among companies to date.

Table 2.2: Overview of the standard off-the-shelf bulk HTSs.

Company	LRE-system	Dimension Ø/thickness (mm)	B_T at 77 K (T)	Price (€)	Effective price* $(Tg^{-1}€^{-1})$
ATZ®, Germany [86]	Y-Ba-Cu-O	30/10	1.1	300	0.07
CAN Superconductors®,	Y-Ba-Cu-O	28/10	0.8-1	280	0.05-0.07
Czech Republic [98]	Y-Ba-Cu-O	56/16	1.2-1.4	650	0.03-0.04
Nippon Steel®,	Gd-Ba-Cu-O	60/20	2	5000	0.3
Japan [95]	Gd-Ba-Cu-O	100/20	n.k.	12600	n.k.

*With ρ_{HTS} = 6,38 g/mm³ [99].

2.2.5 Trapped field mapping

To characterize the magnetic potential of bulk HTSs two non-invasive characterization methods are known:

1) the levitation force measurement [97],

2) the trapped field mapping [100].

The trapped field mapping is fast, cheaper (because it requires less cooling) and has a long tradition for levitation applications [97]. However, it depends on the experimental setup and the quality of the permanent magnet system used. In contrast, trapped field mapping - measurement of the trapped magnetic flux density distribution - has been identified as reliable and reproducible method to characterize bulk HTSs [100]. Usually, liquid nitrogen is deployed for refrigeration, whereas an electromagnetic coil [63] such as the Weiss magnet is used for magnetization.

An exemplary equipment for the trapped field mapping is schematically shown in Figure 2.16. It includes electromagnetic coils for magnetization Figure 2.16 a), a LN_2 cooling bath and a scan Hall-probe facility. The latter can be either a system with 3D step-scanning or a system with a rotating array of Hall probes, Figure 2.16 b) [100] and Figure 2.16 c) [96] respectively. As a result, the distribution of the trapped magnetic flux density can be measured in the xy-plane at fixed z-distance. An example of $B_{T,y}(x,z)$ in shown in Figure 2.11 b).
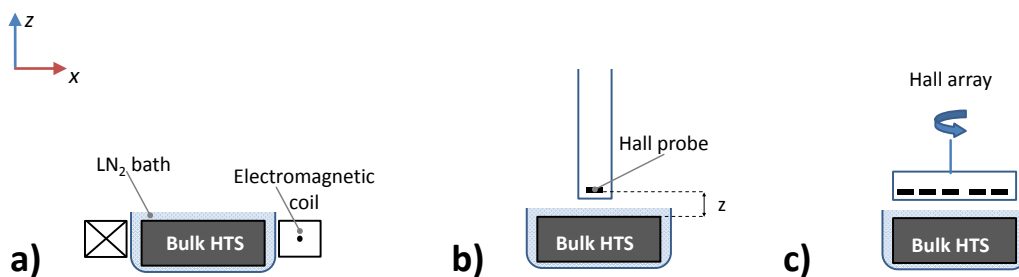

Figure 2.16: Schematic equipment of the trapped field mapping showing: **a)** a magnetization of the bulk HTS, following by the 3D scanning of the trapped magnetic flux density B_T either with **b)** 3D step-scanning system and one Hall-probe or **c)** a rotating array of Hall probes.

2.2.6 Magnetization

Static magnetization.   As a rule, a large-bore superconducting solenoid is useful to magnetize the TFM. In this case, the applied magnetic field increases and decreases

slowly, thereby ensuring a quasi-static regime with constant temperature. Therefore, magnetization using the superconductive solenoid is called a static magnetization.

The static magnetization can be done in so-called *field cooling (FC)* and *zero-field cooling (ZFC)* regimes, where the applied field is directed along the superconductor's *c*-axis. Figure 2.17 sketches both regimes. In the case of ZFC, the superconductor is cooled below its T_c and then the external magnetic field $2B_A$ is applied. In FC, B_A is applied at first, and then the superconductor is cooled below its T_c. Both regimes can magnetize a superconductor to its theoretical maximum magnetization. However, in case of FC, the magnitude of the applied field is equal to the target trapped field, whereas for the case of ZFC the required field that is applied is twice the strength [42]. Thus, FC is more favorable from a practical point of view [62, 101].

The static magnetization enables the sample exploration of the field trapping capability, but it is very expensive for the magnetization in high magnetic fields ($> 2\,\mathrm{T}$). Furthermore, such a facility (magnet) is available only at specialized laboratories, e.g. National High Magnetic Field Laboratory (NFMFL), Tallahassee, USA [102] or Tsukuba Magnet Laboratory, Tsukuba City, Japan [103]. Furthermore, it is time-consuming because the applied field is removed at a low ramp rate to avoid thermal instabilities [38]. A ramp rate of $0.1\,\mathrm{T\,min^{-1}}$ or less has proven to be most effective [21, 104].

Pulse field magnetization.   An alternative to the static magnetization is the pulse field magnetization (PFM). Here, the pulsed magnetic field on the order of milliseconds is applied to a bulk by discharging the energy stored in a capacitor bank through a copper magnetizing coil [101]. PFM is fast, compact, relatively inexpensive and offers *in-situ* or portable magnetization of TFM. The rapid dynamic motion of the magnetic flux induces significant heat, which warms up the bulk HTS and affects the trapped field [101] Thus, trapped fields obtained by PFM are usually lower than those obtained by a static magnetization. The current record of $5.2\,\mathrm{T}$ at $29\,\mathrm{K}$ has been reported by Fujishiro *et al* [105].

Current research on PFM optimization continues to be carried out. It focuses on various PFM parameters, such as the environmental temperature [106, 107], pulse duration, amplitude of the applied field [108], thermal conductivity of the bulk HTS [101, 109], the type of the magnetizing coils used [110, 111], etc. Several novel PFM approaches have been suggested: sequential pulsed field application (SPA) [112], an iteratively magnetizing pulsed field method with reduced amplitude (IMRA) [113], and a modified multi-pulsed technique with stepwise cooling (MMPSC) [105, 114–
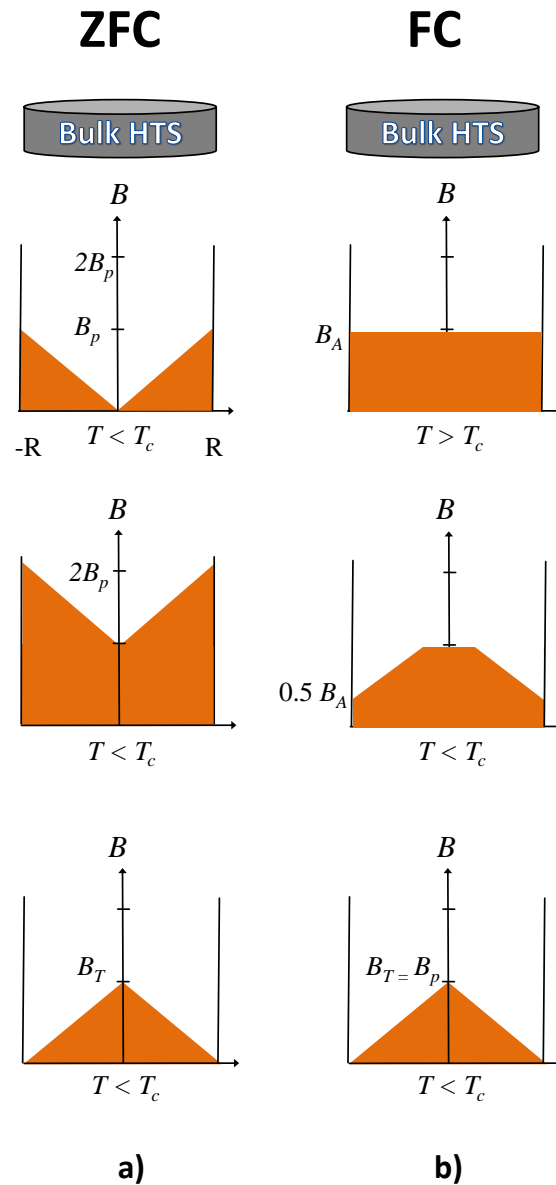
Figure 2.17: Distributions of the magnetic flux density $B(r)$ in the bulk HTS during and after magnetization using Bean model [42, 43]. **a)** Zero field cooling: for a superconductor, which is cooled below its T_c, magnetic field of magnitude equal to a full penetration field, B_p is applied (top panel). Then this field is increased to $2B_p$ (middle panel) following its decrease to zero. As a result, field $B_T = B_p$ is trapped by the bulk HTS (bottom panel). **b)** Field cooling: the superconductor is kept above T_c in the presence of an applied magnetic field B_A (top panel). Then, the bulk HTS is cooled below its T_c followed by slow decreased of the applied field B_A (middle panel shows the case with of $0.5\,B_A$). Ultimately, the trapped field is also equal to the applied field $B_T = B_p$ (bottom panel).

116]. Recently, Cambridge Bulk Superconductivity Group [75] using portable TFM (see Section 2.2.2) [75] achieved the trapped magnetic field of 3 T exploiting a "flux leap phenomenon" induced by heat generation [117]. An extensive review about the magnetization of the TFM, including PFM and its modifications is given in [101].

2.2.7 Cooling

2.2.7.1 Cooling with cryogenic liquid

A straightforward way to cool bulk HTS is to immerse it into the open liquid nitrogen (LN_2) bath. Indeed, such a simple method continues to be utilized in many demonstration experiments. However, this method consumes a huge amount of LN_2 owing to tremendous heat losses and is fairly impractical for application. Moreover, the direct contact of the bulk HTS with the LN_2 may degrade its superconducting properties: frost and moisture that form as a result of thermal cycling can penetrate into the holes and cracks in the near-surface of the bulk, potentially causing damage [61].
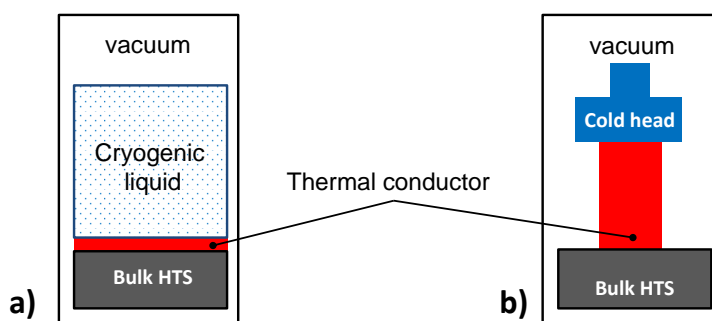

Figure 2.18: Schematics of the cooling systems of the TFM system: **a)** cooling with a cryogenic liquid, **b)** cooling with cryocooler.

A pragmatic way of cooling and maintaining the bulk HTS at desired cryogenic temperature is to use a solid conductive cooling. In this case, the bulk HTS is enclosed in a vacuum cryostat and is attached to the cold stage of a cooling source, e.g. cryogenic liquid tank or cryocooler cold head. Figure 2.18 presents schematics for both cases: the cryogenic liquid tank has been utilized in MagLev cryostats [118], where the cryogenic liquid is LN_2. The cryocooler cold head is used in portable and desktop TFMs [75–78].

There is a long tradition in laboratory research of cooling with cryogenic liquids, where latent vaporization heat fuels the main heat transfer process. The main advantages are large cooling power and simplicity in cryogenic design. However, it requires availability or regular supply of cryogenic liquids and learning to handle them.

Liquid helium (LHe) and liquid nitrogen (LN$_2$) are common cryogenic liquids, although other cryogenic liquids can be used. For example, liquid hydrogen with a high latent vaporization heat is a suitable coolant at temperatures below 20 K, especially for transport applications where H$_2$ is major fuel [119]. Neon is very well suited to cool rotating machines operating around 27 K [120]. Table 2.3 lists common cryogenic liquids, identifying their main properties.

Table 2.3: Properties of common cryogenic liquids. Data is taken from [99]

Cryogenic liquid	Boiling Point, B.P. (K)	Latent heat of vaporization at B.P., $(kJ\,l^{-1})$	Cost per liter $(\text{\texteuro}l^{-1})$
^{4}He	4.23	2.59	9.50 [121]
N$_2$	77.36	160.60	0.58 [121]
Ne	27.10	103.50	not known (n.k.)
H$_2$ (para)	20.26	31.54	n.k.

2.2.7.2 Cryocooler

The use of a cryocooler[11] excludes risks and efforts associated with cryogenic liquids and is more attractive for practical applications [66, 67]: Instead of using evaporating cryogenic liquids, the cryocooler uses electricity [123]. Thus, the deployment of the cryocooler offers a user-friendly "plug-and-play" configuration. However, cryocoolers are usually restricted to net cooling power and, therefore, require accurate cryogenic design.

So far, there is no customized cryocooler for direct application in bulk superconductivity, but cryocoolers are well-established and thoroughly tested for use in space technologies and military industries [124, 125]. A useful article explaining a basics of cryocoolers and related thermodynamic systems is given in [125], whereas an extensive review about cryocooler applications is described in [124]. The review [126] is restricted to cryocoolers for superconducting devices.

In fact, Stirling, Gifford-McMahon, and pulse tube cryocoolers were already used for TFM systems [75–78, 127], but the choice of a suitable cryocooler strongly depends on the specifications of a particular application.

---

[11]Cryocooler (cryogenic cooler) is a standalone device that actively cools a sample down to cryogenic temperatures [122].

Stirling. The long history of the Stirling refrigerators in cooling infrared equipment has resulted in great advancement. Today, high-efficient Stirling cryocoolers are available in a small size and convenient geometry [125]. A standard Stirling cryocooler includes a pressure wave generator and a cold head. Optionally, the pressure wave generator can be connected directly to the cold head, forming a so-called *integral cryocooler*. However, often the pressure wave generator is separated by a so-called split hollow line and cryocoolers are called *split croycoolers* [123]. The advantage of integral cryocoolers lies in their compactness and efficiency, although they also strongly vibrate and are noisy. Generally, a lower vibration level is attributed to the split configuration. Also, the split cryocooler allows for several options regarding the cold head and compressor orientation. This is crucial because a cryocooler's cooling performance will often diminish unless it is positioned with the cold end pointing downward [128]. The examples of both configuration are presented in Figure 2.19 a-b).
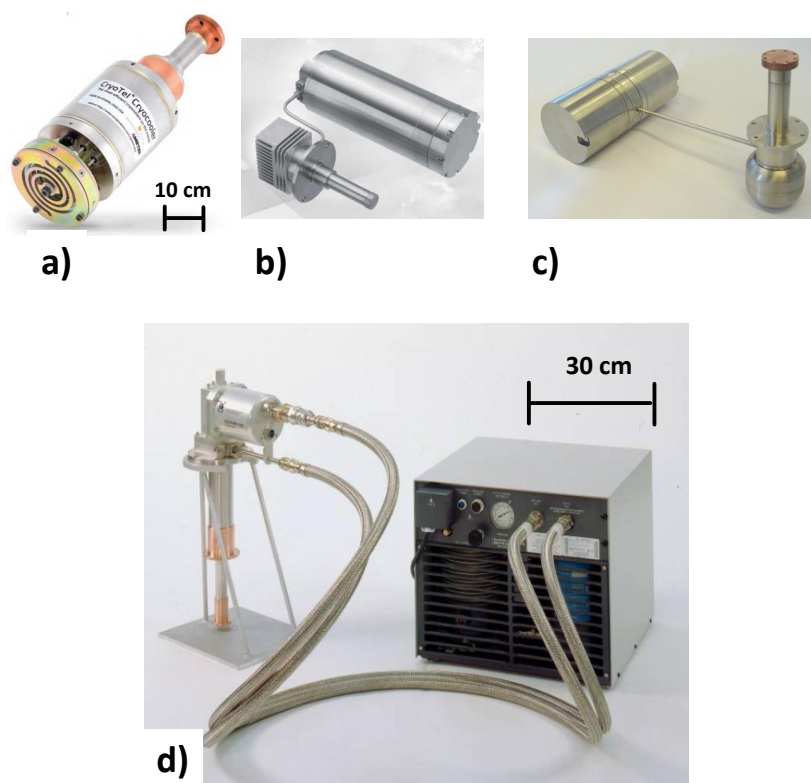
Figure 2.19: An example of a close-cycle cryocoolers: **a)** integral Stirling (CryoTel® CT, Sunpower Inc., USA) [129], **b)** split Stirling cryocooler (AIM®, Germany) [130], **c)** pulse tube (Thales®, France) [131], **d)** Gifford-McMahon [123].

Commercial Stirling cryocoolers with a mass up to 5 kg usually have a cooling power in the range of 1-10 W at 77 K. They are able to reach temperatures from 40 K to 65 K

and mostly operate at frequencies corresponding to the electric line 50 or 60 Hz [123, 124, 132].

Pulse tubes. The pulse tube refrigerator is in some ways similar to the Stirling cooler, but it does not use moving components. Figure 2.19 c) shows an example of a light pulse tube manufactured by Thales®, France. The nature of this device is reviewed elsewhere [133–135]. With the introduction of the orifice concept by Mikulin *et al* [136] the relocation of the orifice [137] and other improvements allowed to achieve an efficiency, comparable to Stirling cryocoolers. The separation of the cooling and heating cycle is realized via a slug of helium gas that acts as the displacer. Thus, the pulse tube cryocooler has an inherent potential to increase of the lifetime of a cryogenic device, reliability and reduce of the vibration level.

Gifford-McMahon. The operating principles of the Gifford-McMahon (GM) cold head is the same as for the Stirling cryocooler. However, the GM cryocooler operates at much lower frequencies ranging between 1-5 Hz. These cryocoolers are always split cryocoolers and consist of a compressor package and a cold head package. The compressor package consists of a hermetic compressor to pump helium in circuit, an air or water cooler to absorb the heat of compression and a complex oil rejection system in order to avoid oil and oil vapor inside the cold head. The cold head package includes the working cylinder with the displacer, the regenerator, and a valve system [123]. The main downside of GM is that they are about 10 times larger and heavier than the Stirling and pulse tube coolers (see Figure 2.19). However, they provide much higher cooling powers at 80 K and or lower temperatures, e.g. 2-20 K.

Lightweight cryocoolers whose mass is not larger than 5 kg[12] are good candidates for TFM refrigeration.

Table 2.4 lists suitable crycoolers and compares their main characteristics such as mass, heat lift Q_c, vibration level, and price. Nevertheless, all cryocooler have different limitations on the allowable magnetic field interface. For the split type cryocooler, the cold head is almost unaffected by the magnetic field, while compressor might operate improperly due to the harm of the permanent magnetic materials in the motor [138, 139]. It may cause some level of worse vibration performance [140].

The effect of magnetic field on cryocooler. The operation and efficiency analysis of the cryocooler exposed to magnetic fields were considered in [131, 138]. It was

---

[12]The mass limitation of 5 kg is a compromise to ensure that the entire TFM systems remains portable.

Table 2.4: Overview selected cryocoolers with the mass of 5 kg [141].

Manufacturer:	AIM®	CryoTel®	CryoTel®	Thales®
Model	SL150	DS 1.5	MT	LPT 9510
Type	Stirling	Stirling	Stirling	Pulse tube
Q_c, (W)	1.5	1.4	5	1.4
Mass, (kg)	2.3	1.6	2.1	2.1
Vibration, (g, rms)	9.5	4.5	n.k.	0.5
Price, (k€)	15.0	18.4	22.8	20

revealed that the magnetic induction in order of 20-50 mT is critical. In addition, the integral cooler (CryoTel® CT, Sunpower Inc.) and its controller was tested in uniform magnetic fields suggesting that the performance was only moderately influenced by up to 45 mT [129].

Manufacturers thus recommend to either increase the distance between the cold head and the compressor or to shield the compressor. However, shielding the compressor would reduce the efficiency by 20 % as compared to the nominal efficiency [129–131, 140]. The cryocooler of the portable TFM is paused during the PFM and is therefore not affected. For static magnetization, the cryocooler can be placed at a greater distance to the cold head.

Vibration. Another drawback of cryocoolers are vibrations, which can not be correctly predicted because they can not be accurately modeled. Vibrations can be reduced by selecting a suitable cryocooler type and configuration as well as the appropriate mechanical connection to the cold object. Pulse tubes vibrate less (e.g. Thales®, France, see Table 2.4) and are favorable when choosing a cryocooler, whereas cooling with a liquid cryogen is the better choice for precise force measurements in LFV when vibrations must be avoided.

2.2.8 Record trapped fields

A number of high trapped field experiments were reported in the literature. Particularly, Nariki *et al* [142] reported the trapped field of 4.30 T between two Gd-Ba-Cu-O bulk samples at 77 K. Furthermore, by lowering the temperature, Gruss and collaborators [143] achieved the trapped magnetic field of 16 T at 24 K in the middle of the Y-Ba-Cu-O double-sample-stack combining effects of intrinsic reinforcement, i.e. Zn- and Ag-dilution, and external thermal compression by a steel tube. Later, Tomita and Murakami [144] reported a trapped field of 17.24 T at 29 K in a similar stack of

pristine Y-Ba-Cu-O bulks, but impregnated with the resin and Wood's metal[13] as well as wrapped with carbon fiber. A current record of the trapped magnetic field of 17.60 T (at 26 K in the middle of double-sample-stack Gd-Ba-Cu-O bulks) was achieved by the Cambridge Bulk Superconductivity Group [21].
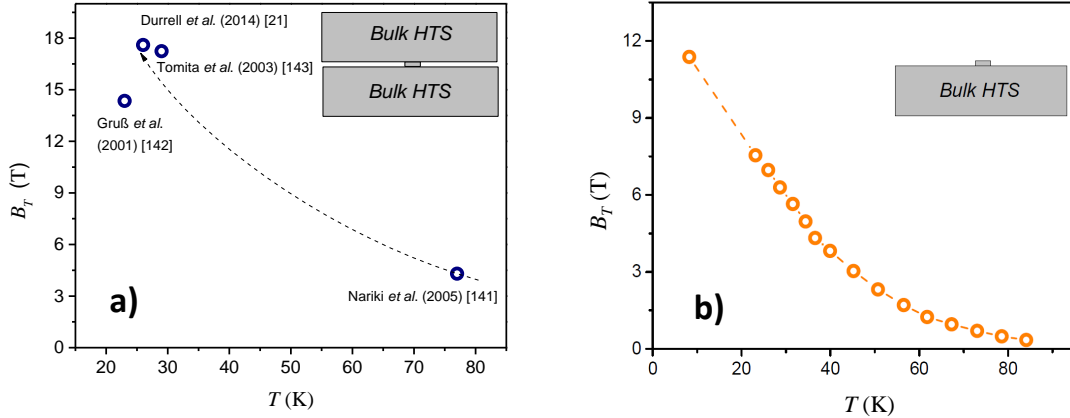

Figure 2.20: **a)** Record trapped field B_T for double-sample stack samples as function of the temperature. Dashed arrow is guide for eyes. **b)** Temperature dependence of the trapped magnetic field for the a single bulk HTS. Data is reproduced from [20].

The discussed trapped field values were obtained between the assembly of two bulk HTS samples. However, the magnetic field generated at the surface of one bulk HTS is a desirable requirement of the TFM for many practical applications, such as LFV, NMR, MRI, and drug targeting. As a rule, a trapped field ranges from 1.0 T to 3.1 T at liquid nitrogen temperatures [38, 142]. Again, with reducing the temperature B_T is remarkably enhanced. For instance, Ikuta *et al* [85] demonstrated 8 T at 40 K for Sm-Ba-Cu-O bulk HTS, whereas 11.4 T at 17 K for Y-Ba-Cu-O bulk HTS was achieved by Dresden group [20, 104].

Figure 2.20 a) collects the trapped field as a function of the temperature for double-sample stack configurations, despite different samples and applied conditions. Figure 2.20 b) plots temperature dependence of the trapped field at the surface of the single Y-Ba-Cu-O bulk reported by Müller *et al* [20].

However, the maximum trapped field for double-sample stacks or single bulk HTSs is not limited by the superconducting and magnetic properties of the material, rather by the poor mechanical properties due to their brittle behavior [21, 61]. Many experimental works reported the fracturing of bulk HTS during magnetization [104, 146, 147],

---

[13]Wood's metal is a eutectic, fusible alloy consisting of of 50 % bismuth, 26.7 % lead, 13.3 % tin, and 10 % cadmium by weight with a melting point of approximately 70 °C [145].

especially, "record" experiments [21, 143, 144].

2.2.9 Limitations of TFM at low temperature

Mechanical stability. The bulk of LRE-Ba-Cu-O is ceramic and has low tensile strength σ_B. Typically, σ_B of unreinforced LRE-Ba-Cu-O bulk lies in the range of 20 MPa to 50 MPa [63, 66] and depends on the fabrication process. During MTG processes many detrimental macro-defects such as cavities, voids and cracks are formed. These formations have a positive effect on fabrication, because they significantly reduce the time required for an oxygenation procedure [148]. However, formed defects also result in a wide variation of performance from sample to sample and experiment to experiment [21]. Thus, the sample fracturing during the magnetization has been reported in many works [104, 146, 147]. In some cases, mechanical damage at the surface of the bulk HTS was directly observed. In other cases, degraded or irregular distribution of the trapped magnetic flux density was reported. This means that the sample underwent some internal damage (e.g. crack inside the volume). An example of Y-Ba-Cu-O bulk with a crack after high field measurements is shown in Figure 2.21.

The fracture behavior occurs when bulk HTS is magnetized and subsequently cooled from RT down to cryogenic temperatures. Thermally induced stress can either generate new cracks or worsen existing ones [147]. It is especially important to discern cracks as they occur upon the initial cool-down process, since the magnetization process further stresses the material, impacting mechanical stability. The material stress is caused by Lorentz forces that arise when an induced supercurrent interacts with an externally applied magnetic field. In fact, these forces act on the flux lines, which are anchored to the pinning centers within a crystal lattice. Hence, an equally large force is transferred to the crystal lattice and the collective effect of these forces causes the mechanical deformation [38, 147]. Moreover, as the applied field magnitude is increased or decreased, Lorentz forces can exceed the tensile strength of the material, causing mechanical failure.

For cylindrical bulk, however, a simple estimation of maximum trapped field can be found using the following relation [144]:

$$\frac{\sigma_B}{(\text{MPa})} = 0.282 \cdot \frac{B_T^2}{(\text{T}^2)}. \tag{2.15}$$

According to Eq. 2.15 fracturing is expected at fields of 7-13 T. Therefore, mechanical
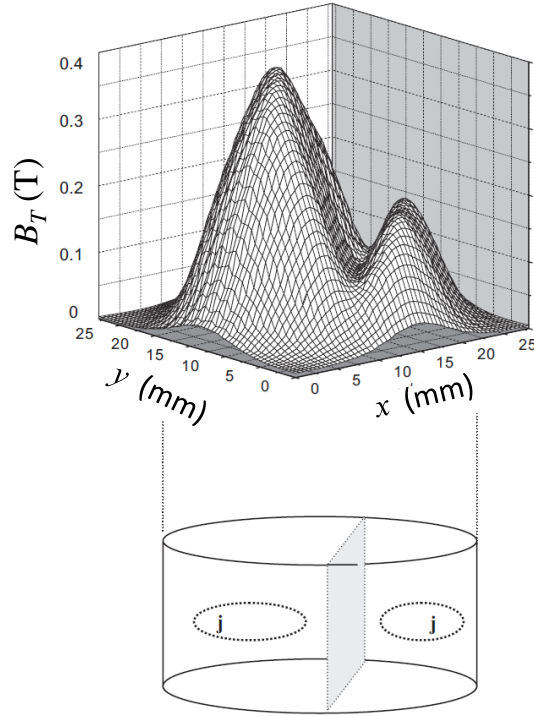
Figure 2.21: **a)** Distribution of the trapped magnetic flux density B_T after high field measurements. **b)** sketch of the bulk HTS illustrating the crack and two regions with supercurrent loops j [38].

stabilization is an issue to be resolved. Generally, there are several strategies to avoid sample fracturing during magnetization:

- internal reinforcement (increasing the fracture toughness by extra processing),

- external reinforcement, e.g. banding with metal ring,

- combination of the two.

Internally, the mechanical strength of the bulk HTSs can be improved by resin impregnation [149] and adding silver [150, 151]. These treatments reduce the number and size of microcracks and increase the fracture strength of bulk LRE-Ba-Cu-O from 30 MPa up to 70 MPa [149–151]. However, a different thermal contraction between the bulk HTS and resin may disturb the near-surface of the bulk during thermal cycles and/or magnetization. In addition, Floegel-Delor *et al* [152] proposed to combine resin impregnation with copper deposition technique, wherein copper atoms diffuse into the holes and cracks in the near-surface of the bulk. Alternatively, mechanical properties of the bulk Y-Ba-Cu-O were improved after a two-step, buffer-aided top

seeded infiltration and growth (BA-TSIG) technique [153] instead of TSMG. In this case the Ag-dilution or resin impregnation are unnecessary, which in turn considerably reduces the cost of bulk HTS fabrication.
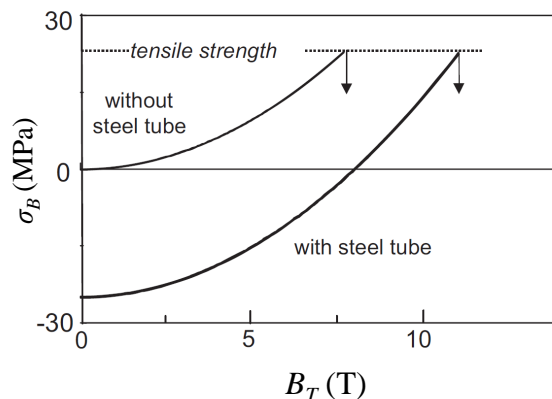
Figure 2.22: Dependence of the tensile stress σ_B on the trapped field B_T in bulk HTS unreinforced and reinforced with a steel tube. Due to the compressive pre-stress much higher trapped fields are achievable without fracturing. Data is taken from [38].

An external action of reinforcement is to encapsulate the bulk HTS within a metal tube [104, 143] or to wrap it with carbon fiber [144]. In this case, the sample is compressed in ab - plane at the interface between the bulk and metal owing to the thermal contraction difference during cooling from RT to the prescribed cryogenic temperature. Figure 2.22 illustrates the effectiveness of the metal tube reinforcement with the regard to tensile stress, σ_B of the bulk HTS as function of the trapped field, B_T. It is assumed that a critical tensile strength is 30 MPa. Thus, in case of unreinforced bulk, σ_B scales with squared trapped field in accordance with Eq. 2.15. However, when a metal tube is used, negative stress compresses the bulk as it is cooled down to cryogenic temperature at the absence of a trapped field. As the trapped field is increased, this negative stress decreases, changing the sign at prescribed B_T and crosses $\sigma_B(0)$ at considerably higher fields [38]. Compression can be further improved by shrink-fitting [21] or enforcing with Fe-Mn-Si shape memory alloys [154].

A good candidate for the tube reinforcement is a non-ferromagnetic metal, which has a coefficient of thermal expansion higher than bulk HTS, while large enough stiffness and yield strength to withstand strong mechanical forces. Thus, the best choice is an austenitic stainless steel alloy, such as American Iron and Steel Institute (AISI) 304[14].

---

[14]In Germany AISI 304 steel is defined by designations given in Euronorm EN 10088. This designation follows the the material number (Werkstoffnummer) 1.4301.

The AISI 304 steel has high Young's modulus (i.e. $E = 200\,\text{GPa}$ [99]) and low magnetic susceptibility at low temperature (i.e. $\chi \approx 10^{-3}$ at $77\,\text{K}$ [99]). Also, it readily available in a form of thin-wall tube, however, the AISI 304 is sensitive to the cryogenic temperature cycling (also welding) and can transform into a martensitic phase, which is ferromagnetic.

In addition to the experimental efforts on bulk HTS reinforcement, there is considerable progress to the problem using analytic and numerical methods. Early reports [146, 147, 155, 156] mainly considered the electromagnetically induced stress on bulk HTS during magnetization, while in the later works [157–162], numerical models are continuing to improve (e.g. include temperature influence) and remedy reinforcement approaches. However, to realistically model the problem more information is necessary regarding the real thermal and mechanical properties of bulk HTS (and also reinforcement metal) at low temperatures.

Flux jumps and thermal instability. Nonetheless, if the bulk HTS remains mechanically holistic during magnetization, it may undergo a thermo-magnetic instability, which can lead to a partial or complete suppression of B_T [38]. This instability occurs because of the flux reconfiguration (or *flux jumping*) towards the equilibrium and is accompanied by sudden heating of a superconductor[38]. Such scenario is a frequent phenomenon of Type II superconductors. For example, the experimental visualization of flux jumping has been demonstrated in magneto-optical imaging experiments [163]. The origin of flux jumps has been explained in a frame of the adiabatic model [164], which compares the thermal diffusivity D_{th} and magnetic diffusivity D_m. In case of $D_m > D_{th}$ the heat generated in the superconductor due to the motion of the magnetic flux cannot be effectively cooled and results in the abrupt reduction of j_c. This, in turn, leads to the reduction of the B_{in} upon ramping the B_A to zero.

Nevertheless, record experiments of the high trapped field [143, 144] have been conducted using the static FC magnetization. This means that the adiabatic model (assuming instant conversion of the magnetic energy change into the released heat) cannot be applied. Mints and Brandt [165] developed a dynamic model ($D_m < D_{th}$) concerning a thin slab in the transverse magnetic field and determined the criterion of the first flux jump:

$$B_{j1} \propto \sqrt{\frac{j_c h}{\dot{B}_A}}, \tag{2.16}$$

where j_c is a critical current density, h is heat transfer coefficient to the coolant and $\dot{B}_A$ is the field ramp rate at which the applied field is reduced to zero. Thus, the

remedy to the flux jumping problem was to slowly reduce the applied field during the FC magnetization and to improve the "cryo-stability" of the superconductor, e.g. impregnated with the Wood's metal [144].

Later, the Krabbes group experimentally elaborated the flux jump phenomenon in Y-Ba-Cu-O bulk HTSs under conditions of the high magnetic field and low temperature. Their results are illustrated in Figure 2.23, which presents the measured B_T of the 4-mm-diameter Y-Ba-Cu-O bulk as function of temperature T. At temperatures below 20 K B_T is limited by flux jumps (B_{j1} are presented as single data point). It is also shown that B_{j1} decreases with decreasing temperature. However, in these experiments comparable diffusivity $D_m \approx D_{th}$ were documented suggesting that neither adiabatic or dynamic model cannot describe the experimental data.
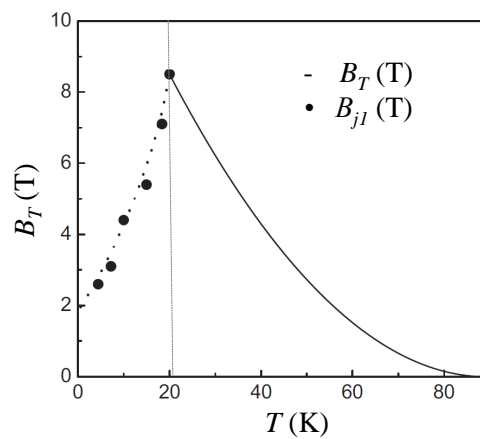
Figure 2.23: Temperature dependence of trapped field B_T in the 4-mm-diameter Y-Ba-Cu-O bulk. Flux jumps with the first flux jump field B_{j1} occur below 20 K. Data is adopted from [38].

Summarizing, bulk HTSs are capable of trapping fields over 16 T [21, 104, 144], but the tendency of mechanical fracturing during magnetization and magneto-thermal instability is a severe challenge to their practical applications. Furthermore, record trapped fields were achieved on specially processed and best-performing samples. The latter fact inevitably leads to high costs (see Table 2.2). For practical applications, however, a standard off-the-shelf and highly-reproducible bulk HTS is highly desired.

3 Lorentz Force Velocimetry: state of the art

This chapter introduces Lorentz Force Velocimetry (LFV) - a contactless method of flow rate or velocity measurement technique, which was thoroughly researched within the Deutsche Forschungsgemeinschaft DFG funded project Research Training Group (RTG) №1567 "Lorentz Force Velocimetry and Lorentz Force Eddy Current Testing" and ran nine years from 2010 - 2018. After shedding light on the working principle and possible industrial applications, the focus is then laid on LFV with regard to electrolytes[1] and various associated technical issues. In particular, the evolution of LFV key sub-systems with a primary emphasis on magnet system (MS) development is discussed in detail.

3.1 Fundamentals

The LFV working principle relies on measuring the Lorentz force that is generated by the relative motion of an electrically conductive medium through a transversely applied magnetic field. The theory of LFV was formulated in [1] and expressed through the scaling law:

$$F_L \propto \sigma u B^2 V, \tag{3.1}$$

where the Lorentz force F_L depends linearly on electrical conductivity σ, mean flow velocity u, magnetic flux density B and a characteristic volume V, which determines the interaction of the magnetic field with the flowing and electrically conductive medium. By measuring the resulting reaction force for a prescribed magnetic flux density and known electrical conductivity, it is possible to determine the mean flow velocity of the fluid. It should be stressed that Eq. 3.1 holds for stationary flow or for the steady state motion of a solid conductor of a constant cross section [1, 2]. The principle of LFV is illustrated in Figure 3.1: The primary magnetic field is generated by a magnet and

---

[1]Electrolyte is defined as a nonmetallic electric conductor in which current is mainly carried by the movement of ions [166].
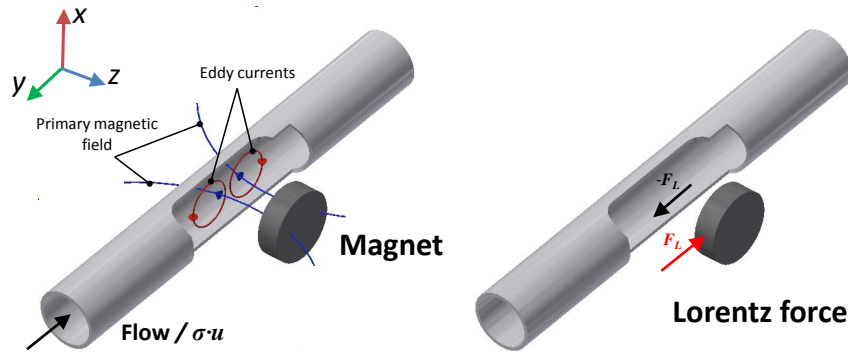
Figure 3.1: Lorentz force velocimetry principle illustrating the interaction of the magnetic field and the liquid flow with electrical conductivity σ and velocity u.

when the electrically conducting liquid passes through magnetic field of the magnet, the interaction between induced eddy currents and the primary magnetic field causes a retarding force to act on the flow [1]. In accordance with Newton's third law, a force (shown by the F_L vector) with a magnitude equal to the retarding force $(-F_L)$, but in the opposite direction, acts on the magnet along the flowing direction.

3.2 LFV application and categorization

Figure 3.2 shows a map of the LFV applications in terms of the resulting Lorentz force, F_L with respect to the product $(\sigma \cdot u)$ as applied to various weakly and strongly conducting fluids.

Here, F_L was calculated according to Eq. 3.1, assuming $B = 0.1\,\mathrm{T}$ and $V = 1 \times 10^{-3}\,\mathrm{m^3}$. Thus, taking into account a significant difference in the electrical conductivity σ and flow velocity u, LFV is categorized into three project areas: liquid metal, solid metal and electrolytes. These projects are represented as patterned rectangles on the LFV map (see Figure 3.2) and are briefly reviewed below.

Liquid metal. It has been shown that LFV works well for liquid metals due to their relatively high electrical conductivity $(\sigma \approx 1 \times 10^6\,\mathrm{S\,m^{-1}})$ and flow velocity $(u \approx 10\,\mathrm{m\,s^{-1}})$. It quickly progressed from the technical demonstration on a Ga-In-Sn eutectic alloy, which is liquid at room temperature, toward the LVF demonstrators and prototypes for continuous casting of steel [3], liquid aluminum [4–6], sodium [7], and tin [8] under laboratory and plant conditions. Notably, above-mentioned practical LFV investigations on liquid metals at elevated temperatures were consistent with magnetohydrodynamic numerical simulations [167, 168] and the experimental
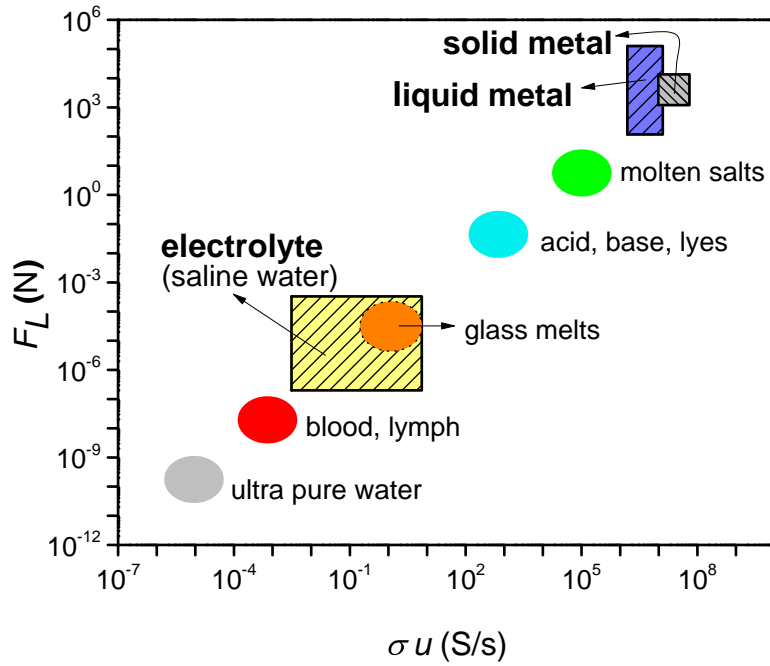
Figure 3.2: Application overview of the LFV for relevant fluids or solid metals. Generated Lorentz force, F_L is calculated according to Eq. 3.1 (with $B = 0.1\,\text{T}$ and $V = 1 \times 10^{-3}\,\text{m}^3$) using reported value of electrical conductivity, σ and mean flowing velocity, u .

dry-calibration [169].

Dry-calibration is done by replacing a fluid flow with the controlled motion of a solid metal where the geometry is fixed and the conductivity is known. Thus, dry-calibration is a straightforward way of carrying out LFV measurements. Other factors to consider are the choice of equipment and a thorough understanding of the critical links between fundamental LFV theory [1] and practical applications. For example, Sokolov *et al* studied the influence of high magnetic Reynolds numbers[2], Re_m by varying the velocity and applied magnetic field [170]. It was found that linear dependence in Eq. 3.1 is preserved for the $Re_m \leq 4$. This means that, in case of higher Re_m (i.e. mean velocity of the conductor changes faster than magnetic diffusion time), measured Lorentz forces are suppressed, leading to errors in the velocity measurements.

Solid metal. LFV also comprises Lorentz force eddy current testing (LET) [171, 172], where the focus lies on inspecting non-destructive defects or flaws in moving metal, e.g. a specimen of a layered aluminum. Further investigations on LET were continued

[2]Magnetic Reynolds number is defined as the ratio between advection and magnetic diffusion

in several Ph.D. works using numerical simulations [173, 174], experiments [175, 176] and inverse calculation to re-construct the defects [177]. Useful review about LET technique can be found in the text books [178, 179] and recent papers [180–182].

For these two areas it is sufficient to use PM MS, since $(\sigma \cdot u) \sim 1 \times 10^6 \, \mathrm{S \, s^{-1}}$, which consequently results in $F_L > 1 \, \mathrm{N}$. Furthermore, these PMs as well as force sensors are commercially available and can be easily combined to measure the force of a corresponding measuring range.

Electrolytes. The world's first LFV laboratory demonstrations on electrolytes were performed in [9–11, 16]. In these works, the saline water modeled the electrolytes with the product of electrical conductivity and mean flowing velocity of $(\sigma \cdot u) = 1 \, \mathrm{S \, s^{-1}}$. This, in turn, led to the force measurements below $1 \, \mathrm{\mu N}$ and required special high-precision force measurement techniques. Force measurements with this type of resolution set a strict limitation on the dead load, which is needed to carry a MS. A more detailed account of LFV on electrolytes and associated technical challenges are given in the following Section 3.3.

3.3 LFV on electrolytes: technical issues

LFV on electrolytes focused on developing of the experimental setup that includes three main sub-systems (see insert of Figure 3.3):

1) *channel facility* containing a fluid, the velocity of which is to be determined,

2) *MS* generating a magnetic field in the channel,

3) *FMS* measuring a resulting Lorentz force and carrying the MS.

Each sub-system was developed within an autonomous Ph.D. project of DFG-funded RTG №1567. Beginning in the year 2010, three Ph.D. projects [183–185] - the first generation - dealt with the question of whether or not LFV can be applied to electrolytic flows. The second generation [18, 186, 187] continued to optimize the corresponding sub-systems, while the aim of the third generation – current generation – is to further extend the LFV measuring range. How the LFV research evolved and which line of questioning each sub-system developed is discussed below.
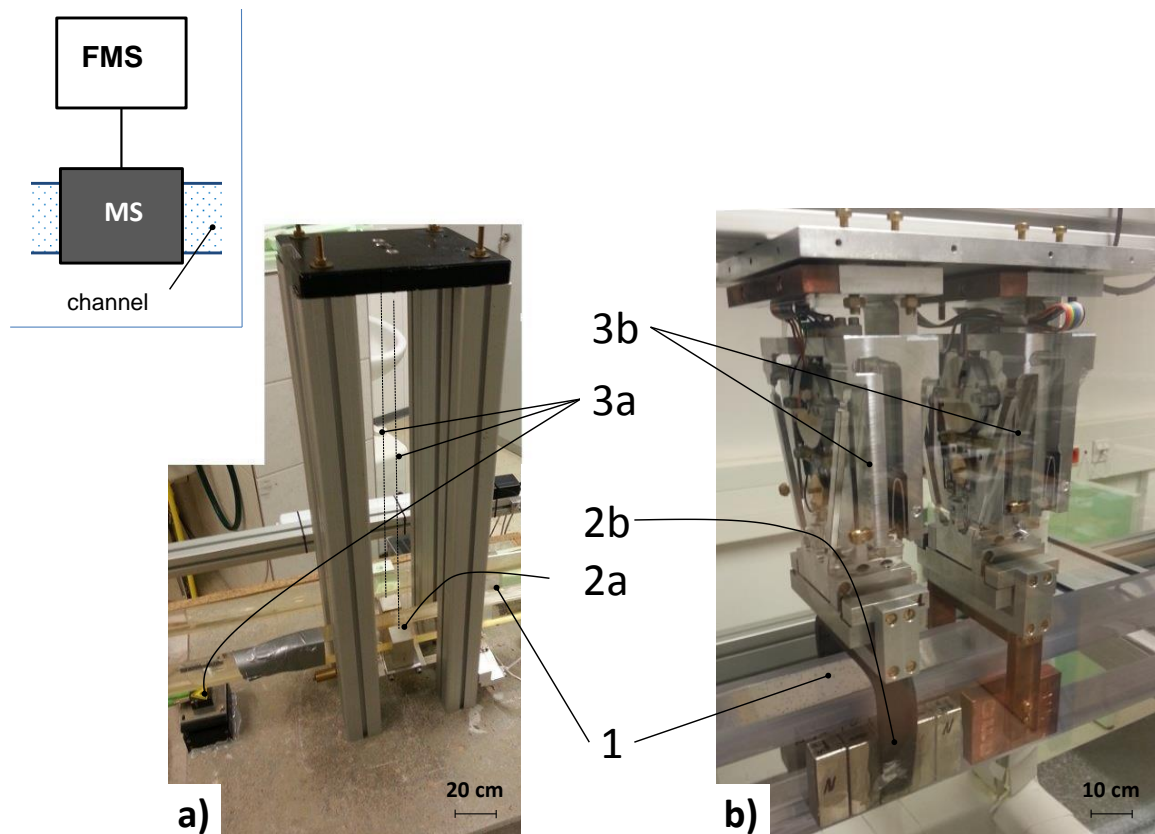
Figure 3.3: **Insert** Schematics of the LFV experimental setup comprising three sub-systems: channel, force measurement system (FMS) and magnet system (MS). The main part of the LFV setup for the first **a)** and second **b)** generations of the RTG. Both setups have (1) the channel with saline water, whereas the first setup consists of (2a) permanent magnet blocks [183] and (3a) Pendulum Force Measurement System (PFMS) (tungsten wires and inteferometer [184]). The second setup consists of (2b) *Halbach* MS [183], and (3b) off-the-shelf force sensor [16].

3.3.1 Channel facility

A horizontally aligned channel facility with the controlled flow of saline water as model fluid was developed and built in [185]. This type of facility was chosen because it is the typical setup in industry, while saline water was chosen for experimental convenience. Further details about the channel facility can be found among Ph.D. theses [183, 185, 186, 188].

The first generation was able to numerically show and experimentally verify that a turbulent flow of saline water can be effectively approximated with a motion of the solid conductor with identical geometrical parameters, electrical conductivity, and prescribed velocity [183]. Later, Wiederhold *et al* [189] tested the LFV with saline water with $\sigma < 20 \, \mathrm{S \, m^{-1}}$ at different flow profiles and regimes reporting insignificant

influence of the laminar to turbulent transition to the LFV measurements. This result, however, means that although the electrolyte flow is laminar or turbulent, it can be effectively modeled or experimentally represented using the motion of a solid conductor.

3.3.2 Force measurements

Thus, Lorentz forces were measured in the horizontal direction. The use of LFV for electrolytes was demonstrated by Wegfrass *et al* [10] during the first generation. Authors utilized a Pendulum Force Measurement System (PFMS), as shown in Figure 3.3 a). Here, the PM blocks were suspended by parallel tensioned tungsten wires, which were mounted on an aluminum frame. The PFMS was adapted to the channel with controlled saline water flow and the force was measured in terms of a displacement using a laser interferometer.

Later, Diethold *et al* [190] replaced the PFMS with a single state-of-the-art weighing cell, the working principle of which relies on the Electromagnetic Force Compensation Balance (EMFC). This extended the force resolution down to $1\,\mu N$ within the range of $\pm\,100\,\mu N$. However, the environmental disturbances such as temperature, seismic noise, vibration, and related other errors significantly affected the LFV measurements.

During the second generation, two identical EMFC weighing cells were proposed to form a Differential Electromagnetic Force Compensation Balance (DEMFC) [18, 191]. Figure 3.3 a) shows both EMFCs mounted on an aluminum frame and adapted to the electrolyte channel: The first EMFC carried the MS, while the second one carried a non-magnetic copper dummy (with a similar geometry, but identical weight). Accordingly, one EMFC measures both the Lorentz force and the cumulative errors, whereas the second measures only the errors. The difference between them indicates the target Lorentz force. The resolution in this case was ameliorated down to $20\,nN$ [191].

Nevertheless, the force resolution using the DEMFC is significantly affected by the temperature, mechanical vibrations, and tilting effects of the mechanical structure. Another serious drawback of DEMFC is the mass limitation of the dead load [184, 192]. In fact, the EMFC consists of a mechanical and an electromagnetic part (i.e. the voice coil actuator) comprising permanent magnets [184]. The mechanical part is made of aluminum and has a complex inner structure. The mechanical properties of this structure determine the dead load - the allowable mass of the MS. The mechanical properties of the EMFC's were analyzed in [184, 192]. Authors calculated the maximum permissible dead load of $3\,kg$. However, this value was reduced to $1\,kg$ due to a compromise between the MS mass and required force resolution.

3.3.3 Permanent magnet system

The first generation [183] performed the selection, design, and optimization of MS simultaneously with the FMS developments [184]. Werner [183] provided a comprehensive analysis of the suitable magnetic sources for LFV on electrolytes, where MS mass was limited to 1 kg: Author compared the magnetic networks both of the PM and current-carrying coils and found that PMs are rather favorable because of their compactness and low weight. PMs do not require power supplies or external heat dissipation (e.g. water cooling), which are further advantages.
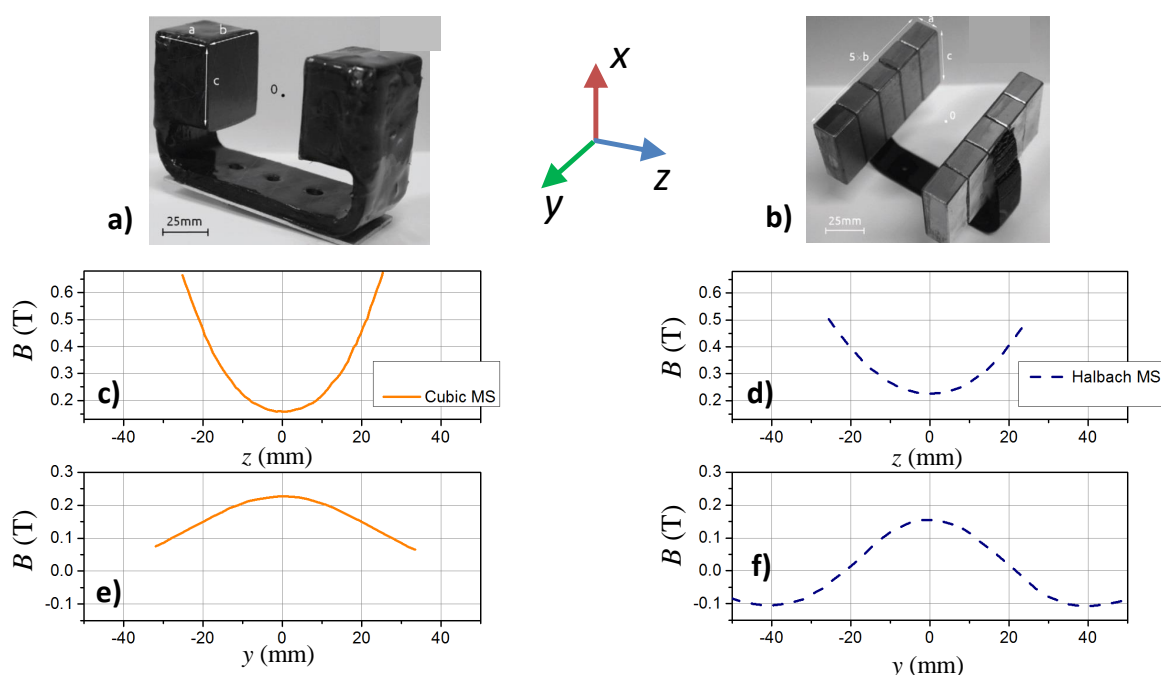
Figure 3.4: MS configurations: **a)** - *Cubic*, **b)** - *Halbach*. Comparison of the distributions of magnetic flux density: **c), d)** along z-axis and **e), f)** along y-axis .

As a result, *cubic* and *Halbach* configurations of the MS without an iron yoke as magnetic circuit for the magnetic field return were proposed in [183] and are shown in Figure 3.4 a-b). *Cubic* MS consists of double cubic Nd-Fe-B magnets that are arranged opposite to each other through the yoke. *Halbach* MS is built from double Halbach arrays arranged opposite to each other, where one side consists of five rectangular Nd-Fe-B magnet blocks. Both MSs were designed and manufactured based on numerical simulations in combination with a special algorithm [193], that considered the ratio between the Lorentz force and MS weight (force-to-mass ratio) as an optimization parameter. It was revealed that the lightweight carbon fiber yoke is more efficient than

the iron yoke[3] due to the force-to-mass ratio [183].
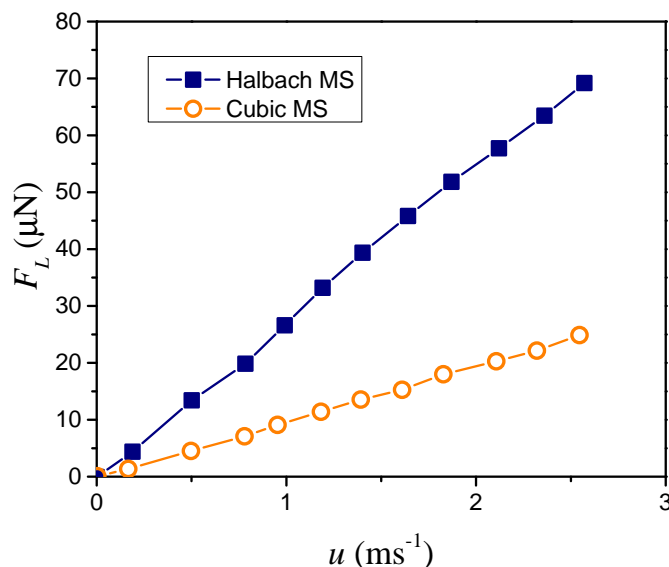
Figure 3.5: Comparison of the Lorentz force generated when using *Cubic* and *Halbach* MS, measured with flowing saline water of $\sigma = 6\,\mathrm{S\,m^{-1}}$. Data reproduced from [11].

The magnetic flux distribution B (along z-axis and y-axis) between the magnetic poles of each MS with the same mass of $1\,\mathrm{kg}$ are compared in Figures 3.4 c-f). As anticipated, $B(z)$ yields a pronounced minimum in the middle for both MSs, but the minimal magnetic flux density of the *cubic* MS is lower than the magnetic flux density for the *Halbach* MS. The reason is the larger stray field of the *cubic* MS. Furthermore, two qualitatively different dependencies are observed for $B(y)$: The *cubic* MS has a broad peak, while *Halbach* MS exhibits one positive peak at the middle and two negative minimums at the sides. Such a Halbach configuration significantly mitigates the stray fields and concentrates the magnetic flux density three times in alternating directions through the channel.

Although the peak magnetic flux density of the *cubic* MS is higher than that for the *Halbach*, the *Halbach* MS is more efficient for LFV, because the $B(y)$ of *Halbach* MS generates five vortices of eddy currents in the fluid, whereas the $B(y)$ of *Cubic* MS only generates two vortices. Moreover, numerical simulations by Werner and Halbedel [193] and consequent experimental validation by Halbedel *et al* [11] demonstrated that utilizing the *Halbach* MS led to the enhanced the F_L by a factor of 2.8. Figure 3.5 compares an effect of the magnetic field generation using *cubic* and *Halbach* MSs, when LFV measurements with $\sigma = 6\,\mathrm{S\,m^{-1}}$ and varying velocity were carried out [11].

---

[3]The iron yoke is commonly used to guide the magnetic flux.

3.3.4 Discussions

The LFV technique for electrolytes was demonstrated to be a feasible measurement method using the special channel facility with saline water and continually improving the magnet and force measurement systems. Specifically, the limited range of the electrical conductivity from $0.06\,\mathrm{S\,m^{-1}}$ to $10\,\mathrm{S\,m^{-1}}$ and flow velocity from $0.2\,\mathrm{m\,s^{-1}}$ to $2.5\,\mathrm{m\,s^{-1}}$ was tested using saline water.

However, for practical applications on the relevant electrolytes, it is required to extend the LFV measuring range to the lower electrical conductivity and slower velocity. Table 3.1 lists electrolytic liquids, where LFV is highly favorable, with reported values of σ, u and calculated F_L. In addition, Figure 3.2 (see page 45) shows several examples of these electrolytic liquids together with the solid metals, liquid metals, and saline water [10, 11, 16] on the LFV application map. In contrast to the saline water, some liquids flow more slowly and have an even smaller electrical conductivity, e.g. blood and ultra-pure water. Other electrolytes (e.g. glass melt, acids, base, lye, and molten salt) not only share a low value of $(\sigma \cdot u)$, they are hot, opaque and aggressive, thereby impeding the close location of the magnet at the channel. Since the magnetic field rapidly decays with increasing distance between the magnet and the outer channel wall, a larger gap between the MS and the channel results in smaller magnetic flux densities in the fluid. This, in turn, is a serious challenge for LFV applications, when aggressive fluids with low values of $(\sigma \cdot u)$ are matter of interest.

Bulk HTSs, acting as portable TFM (see Chapter 1 and Table 1.3), exhibit a potential to provide magnetic flux densities an order of magnitude higher than conventional permanent magnets and are, therefore, highly attractive for the LFV on electrolytes [196]. The prospective idea to employ TFMs has been proposed in several previous works on LFV [9, 10, 16, 200**?**].

Table 3.1: Classification of aggressive and opaque fluids with respect to the measurement forces resulting from Eq. 3.1 (with $B = 0.1\,\mathrm{T}$ and $V = 1 \times 10^{-3}\,\mathrm{m^3}$)

Industrial sector	Fluid type	σ ($\mathrm{S\,m^{-1}}$)	u ($\mathrm{m\,s^{-1}}$)	F_L (N)
Solar power plants	Molten salts	10^2 [194]	10^3 [195]	1
Chemistry	Acid, base, lyes	10^2[196]	1 [196]	10^{-3}
Glass/Semiconductor	Glass melts	10^1 [19, 197]	10^{-2} [19]	10^{-6}
Medicine	Blood, lymph	10^{-1} [198]	10^{-2} [198]	10^{-8}
Pharmacy/Food	Ultra pure water	10^{-6} [199]	1 [199]	10^{-11}

3.3.5 Prior consideration of Bulk HTSs for LFV

In order to gain an understanding of a practical utilization of TFM and their potential, Halbedel *et. al.* [**?**] considered commercial Y-Ba-Cu-O bulks[4] to form MS for LFV. Authors experimentally measured the trapped fields following a FC magnetization. This involved applying a field of 2 T and cooling to 77 K with LN_2. Figure 3.6a) shows the experimental equipment for magnetization [201] consisting of a superconducting magnet with 300-mm-room-temperature bore (CYOGENICS Ltd., London, UK) [202] and the open styropol bath with LN_2. The distribution of the magnetic
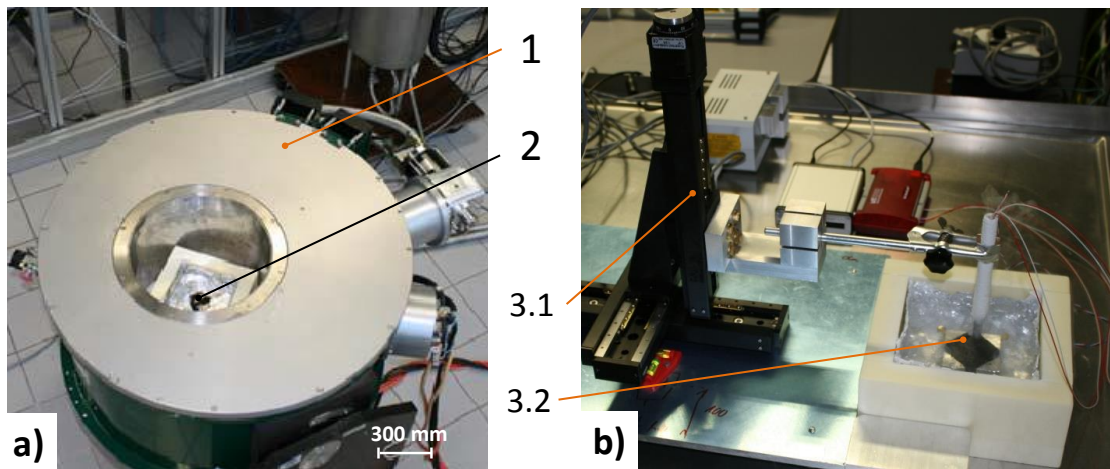
Figure 3.6: **a)** Experimental equipment for magnetization of bulk HTSs. It includes (1) a superconducting solenoid with 300-mm-room-temperature bore and (2) the LN_2 bath styropol box containing bulk HTS [201]. **b)** The Hall mapping setup, which consists of (3.1) a three-axis motorized positioner and (3.2) the cryogenic Hall probe.

flux densities, $B_{T,exp}$ of the magnetized HTS bulks were scanned using a Hall mapping setup, which includes a cryogenic Hall probe (Arepoc s.r.o., Slovakia), a three-axis motorized positioner (Standa Ltd., Lithuania) and Labview® software (see Figure 3.6 b).

The obtained data was used to evaluate the anticipated Lorentz forces using numerical simulation, developed in master thesis by Klaiber [201]. Admittedly, Klaiber adopted the previous model of LFV for electrolytes developed during the first generation by Werner [183], but replaced a permanent magnet with a bulk superconductor customizing the Bean model [42] to a form of

$$j_c = c \cdot B_{T,sim} + d \tag{3.2}$$

---

[4]Y-Ba-Cu-O bulks in form of cylindrical discs and rectangular blocks were purchased from ATZ®, Torgau [86] and CAN Superconductors®, Prague [98].

where j_c is the critical current density, $B_{T,sim}$ - the simulated trapped field, whereas c and d are fit variables to satisfy

$$B_{T,exp} - B_{T,sim} = min. \tag{3.3}$$

It was found that using bulk HTSs nearly double the F_L as compared to the Nd-Fe-B counterparts with the same mass. This result was significant, because it does help to recognize the potential of bulk HTSs for LFV application. Furthermore, simulation studies [201, 203] promise even superior F_L, when bulk HTS is magnetized below 77 K and traps the field one order of magnitude higher.

Consequently, the second generation [187] of the MS-project endeavored to implement bulk HTSs into the LFV experimental setup. At that time, a project strategy assumed development of the bulk HTS MS as an independent sub-system. This concept involved placing the bulk HTS into the compact and light cryostat, which can be attached to the EMFC in the same manner as Halbach MS. It also means that the cryostat must meet two main requirements:

1) cooling and retaining the bulk HTS at temperatures below 77 K;

2) a weight of less than 3 kg (see Section 3.3.2).

However, after consulting with various companies that produce cryogenic equipment[5], it became apparent that engineering and building a cryostat which satisfies both requirements is greatly challenging, requiring a compromise between two options:

a) cryostat of 3 kg operating within 300 K - 77 K temperature range

or

b) cryostat of 10 kg, but operating within the 300 K - 5 K temperature range.

To better understand the trapped field behavior at temperatures below 77 K and other associated technical issues, e.g. magnetization and maintenance, Weidner [187] continued the experimental investigations on the bulk HTSs using two of the heavy cryostats.

Specifications, manufacturing, and testing of these cryostats have been contracted out to ILK Dresden [204], who designed a LHe/LN$_2$ bath cryostat for LFV application.

---

[5]The design concept for the cryostat for LFV application was discussed with three companies specialized in cryostat design and manufacturing. These are ATZ® (Torgau), ILK (Dresden) and VOSKAM® (Oldenburg).
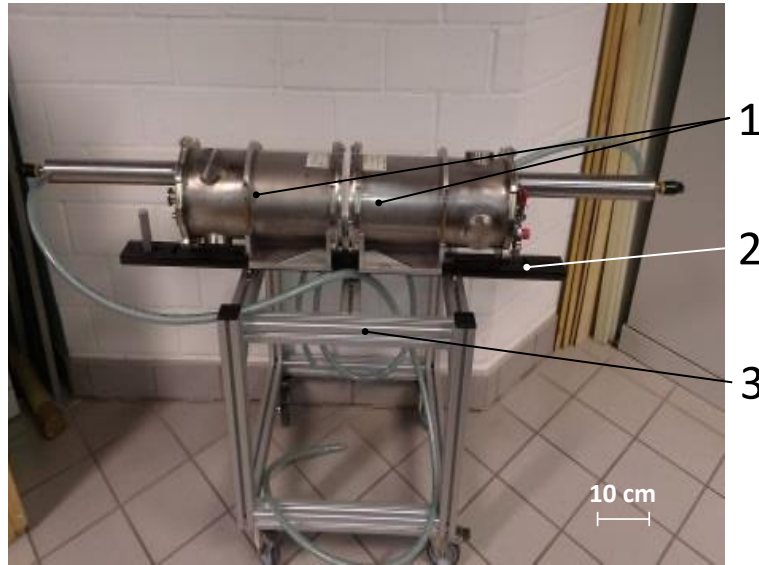
Figure 3.7: (1) Two LHe/LN2 cryostats arranged face-to-face. ILK Dresden [204] was commissioned to manufacture the cryostats as depicted. The cryostats are mounted on the (3) optical bank which is fixed to the (3) table.

This cryostat is capable of cooling down one bulk HTS to $80\,\mathrm{K}$ using LN_2 and maintaining this temperature for $2\,\mathrm{h}$ [204]. Temperatures below $77\,\mathrm{K}$ are achieved using LHe, but this requires a continuous LHe supply [204].

Figure 3.7 shows two LHe/LN$_2$ cryostats purchased from ILK Dresden [204]. Each cryostat weighs approximately $10\,\mathrm{kg}$ and resembles a portable TFM with conductive cooling (cf. Figure 2.18, Section 2.2.7), but instead of cryocooler, the tank with liquid coolant is used for the refrigeration.

As a result, a maximum trapped field of about $1.4\,\mathrm{T}$ following FC magnetization ($B_A = 5\,\mathrm{T}$ at $22\,\mathrm{K}$) was achieved with $46\,\mathrm{mm}$ diameter Y-Ba-Cu-O bulk HTS [187]. Much lower trapped field, in comparison to other portable TFMs (see Table 2.1, Section 2.2.2) is due to the large isolation gap of $12\,\mathrm{mm}$ between bulk HTS surface and the outside wall of the vacuum vessel.

Nevertheless, the research during the second generation was limited to several trapped filed measurements on bulk HTSs, but without considering the practical integration of bulk HTS with the actual FMS (EMFC), since the allowable EMFC dead load and the excessive cryostat mass contradict each other.

3.4 Chapter summary

This chapter reviews the LFV state-of-the-art, specifically focusing on LFV on electrolytes. It is directly followed by the evolution of the LFV key sub-systems with a primary focus on MS. Particularly, after introducing the MS based on PMs it is argued that for the product of $10\,\mathrm{S\,s^{-1}} > (\sigma \cdot u) > 1\,\mathrm{S\,s^{-1}}$ a stronger magnetic source is required. Thus, the bulk HTS is considered as a potential candidate to replace the actual Halbach MS. Nevertheless, the presented studies were limited to:

1) the experimental investigations on Y-Ba-Cu-O bulks, mainly focusing only on measurements of the trapped field distribution,

2) the Lorentz force using the bulk HTS was calculated using the adopted numerical model, but the prove of the working principle of the LFV setup was not experimentally verified and

3) the presented numerical model does not properly exploit the critical state model, instead it makes use of linear fit of the experimental data by varying fit parameters.

Therefore, the further course of this thesis verifies the idea of using bulk HTSs for application in LFV and set initial requirements for an advanced LFV system.

4 Proof-of-principle: LFV using bulk HTS

4.1 Introduction

A bulk HTS, acting as strong TFM, is a promising MS to be integrated to the LFV techniques on electrolytes. It is important, however, to examine the feasibility of bulk HTSs as a substitute for existing Nd-Fe-B PMs in LFV applications: The bulk HTS magnet has a characteristic feature of generating a conically-shaped trapped magnetic flux density, B_T, distribution, that has a sharp field gradient [42]. Whether this feature adequately replicates the LFV theory [1] (Eq. 3.1) is an issue to be answered.

This chapter presents, for the first time, the realization of LFV using bulk HTS. To eliminate technical challenges associated with mass excess and handling, LFV experiments were performed utilizing:

1) dry calibration facility (see Section 3.2),

2) MS, assembled from two bulk HTSs with simplified cooling,

3) off-the-shelf load cell as FMS.

4.2 Experimental

4.2.1 Experimental facility: dry-calibration

Figure 4.1 shows a schematic diagram and photograph of the experimental setup used to test LFV using the bulk HTS MS. The setup consists of five main components: (1) bulk HTS MS, (2) load cell, (3) metal rod, (4) linear drive and (5) aluminum rack. The experimental procedure is fully automated: an IBA-Automation environment controls the linear drive and is used for data acquisition [3]. The linear drive executes a repetitive motion of the metal rod with a prescribed constant velocity. At first, it moves downwards, then reverses its direction and moves back to its initial position.
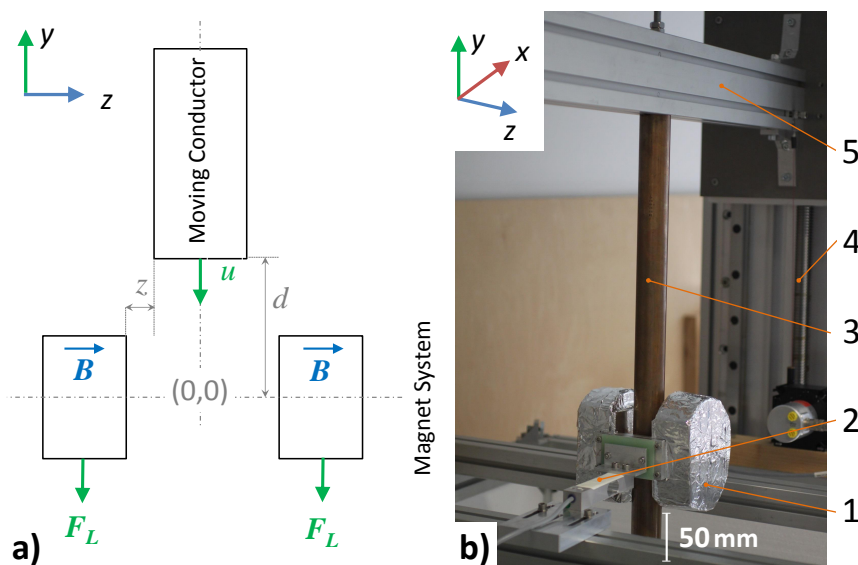
Figure 4.1: **a**) Schematic of the LFV proof-of-concept. **b**) Photograph of the realized LFV experimental setup, which consists of five main components: (1) HTS MS, (2) force sensor, (3) metal rod, (4) linear drive and (5) aluminum rack.

The cylindrical long metal rods have a length of 1000 mm and a diameter of 40 mm. Two types of metal rods were used: copper with an electrical conductivity of $\sigma_{Cu} = 58.96\,\mathrm{MS\,m^{-1}}$ and aluminum alloy (AlMgSi) with $\sigma_{Al} = 19.43\,\mathrm{MS\,m^{-1}}$ [3]. The mean velocities of the copper rod were $u = [54; 64; 76; 81]\,\mathrm{mm\,s^{-1}}$. For the aluminum rod, F_L-measurements with only two velocities of $u = [70; 81]\mathrm{mm\,s^{-1}}$ were possible, due to its lower conductivity and limitations related to the resolution of the present LFV measurement system. Note, the metal rod starts its motion being $d = 165\,\mathrm{mm}$ distant from the center of the bulk HTS MS, whilst the distances between the surfaces of the bulk HTS and the metal rod is $z = 12\,\mathrm{mm}$ on both sides, as shown in Figure 4.1 a).

4.2.2 Force measurement set-up

A commercial load cell (Model PW6D, Hottinger Baldwin Messtechnik GmbH) combined with an analogue measuring amplifier (SOEMER Messtechnik GmbH) was used for force measurements. The force is measured in terms of a voltage with the accuracy class C3. *In-situ* force-voltage calibration was performed using E2 class certified calibration masses of 5, 10, 20 and 100 g.

It should be stressed that the choice of this particular load cell instead of actual EMFC was favored, because of its robustness, dead load limit and simple structure. The later fact, indeed, was crucial for fast mounting the bulk HTS MS to the load cell upon LFV measurements.

4.2.3 Bulk HTS magnet system (MS)

The bulk HTS MS consists of two Y-Ba-Cu-O samples in the form of a cylindrical disc with a diameter of 46 mm and a thickness of 16 mm, provided by ATZ® [86]. The Y-Ba-Cu-O bulks were encapsulated in an aluminum holder and arranged opposite each other with a distance of 64 mm between. The aluminum holders were wrapped
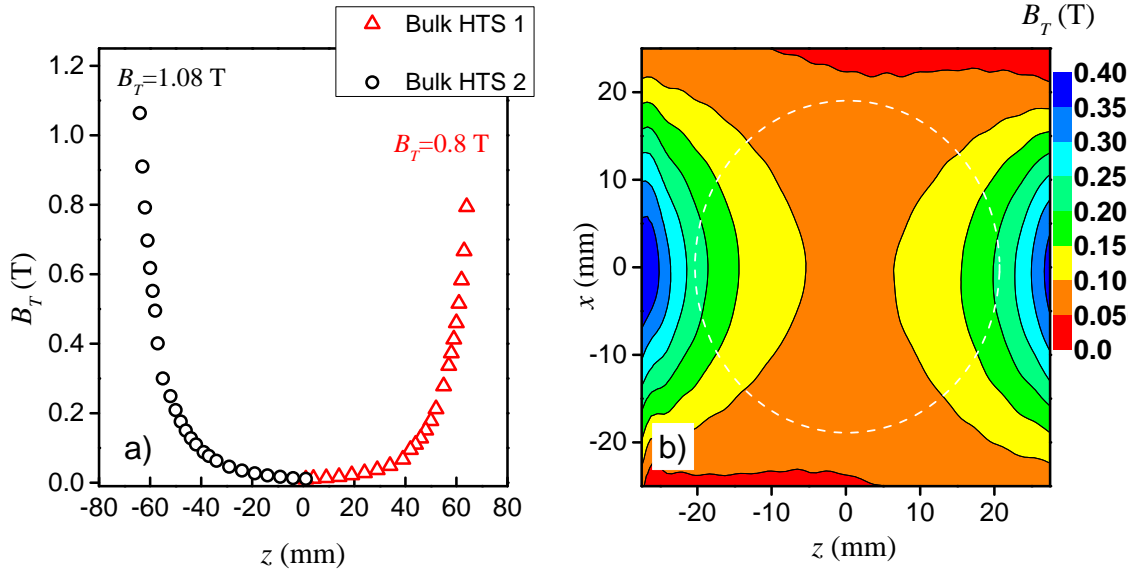
Figure 4.2: **a**) The peak trapped magnetic flux density B_T for each bulk HTS as a function of distance (along the z-axis) with a maximum field of 1.08 T (left) and 0.8 T (right) at the bulk surfaces. **b**) The magnetic flux density distribution $B_T(x, z)$ in the bulk HTS MS gap. The drawn circle indicates the location of the metal rod. Firstly, this was measured for each bulk HTS separately, then for the gap between the two bulks in the HTS MS.

in styrofoam and radiation shielding tape, in order to reduce warming to RT. A plate of fiberglass laminate (type G-10) with a thickness of 10 mm was used to prevent heat transfer from the HTS MS to the load cell.

The bulk HTS MS must be magnetized before coupling with the force sensor. The magnetization was carried out in the RT bore of 5TCFM using FC magnetization: at first, an applied field of $B_A = 1.5$ T was generated; then, the bulk HTS MS was cooled down to 77 K. Cooling was achieved by immersing the entire HTS MS in an open styrofoam container with LN_2, which was refilled periodically, due to the evaporation of LN_2. Afterwards, B_A was ramped down at a ramp rate of 0.092 T min^{-1}. When B_A reduced to zero, the B_T distribution was measured using the Hall mapping.

At first, B_T was measured for each bulk HTS separately, then for the gap between

the two magnetized bulks in the HTS MS. The trapped magnetic flux density[1] B_T for each bulk HTS as a function of distance (along the z-axis) is shown in Figure 4.2 a). A maximum field of $1.08\,T$ (left) and $0.8\,T$ (right) at the bulk surfaces was recorded for each bulk HTS, respectively. The magnetic flux distribution $B_T(x, z)$ in the gap of the bulk HTS MS is presented in Figure 4.2 b). It is qualitatively consistent with data reported in [205–208], where a similar bulk HTS face-to-face arrangement was employed. The relatively large gap between the bulk HTSs in this study was required to enable the unobstructed motion of the metal rod through the bulk HTS MS (see Figure 4.1). In future studies, this gap should be minimized for the proper utilization of the magnetic field, since the maximum trapped magnetic flux density exponentially decreases with increasing distance (cf. Figure 4.2 a). To achieve this, a novel cooling system for the bulk HTS MS must be developed.

4.2.4 Lorentz Force Measurements

When the bulk HTS MS is coupled with the load cell and mounted to the LFV setup, continuous cooling in a LN_2 bath is not possible, because of the mass and volume restriction of the load cell. Hence, it was necessary during the force measurements to extract the bulk HTS MS from its LN_2 bath. The bulk HTS MS holds a trapped field for a specific period of time until it begins to warm up to RT due to the large heat capacity and the sufficiently low thermal losses of this simple constructed bulk HTS MS. During this time, however, the magnetized MS is used only for the LFV measurement with one assigned velocity and require re-magnetization for other velocities. In addition, the temperature of the system during LFV measurements was monitored with a Cernox® sensor.

An example of the periodic rod motion $L(t)$ for a velocity of $u = 54\,mm\,s^{-1}$ and the corresponding time sequence of the Lorentz force measurements is depicted in Figure 4.3 a). The experimental procedure is as follows:

1. $[t_0 = 0; t_1 = 5\,s]$ - extraction of the magnetized bulk HTS MS from the LN_2 bath;

2. $[t_1 = 5\,s; t_2 = 23\,s]$ - coupling with the force sensor and beginning motion of the rod;

3. $[t_2 = 23\,s; t_3 = 500\,s]$ - Lorentz force measurements;

4. $[t_3 = 500\,s]$ - stopping the rod motion and decoupling of the bulk HTS MS.

---

[1]As indicated in Section 2.2.3, B_T indicates the B_z - component of vector $\vec{B}$.
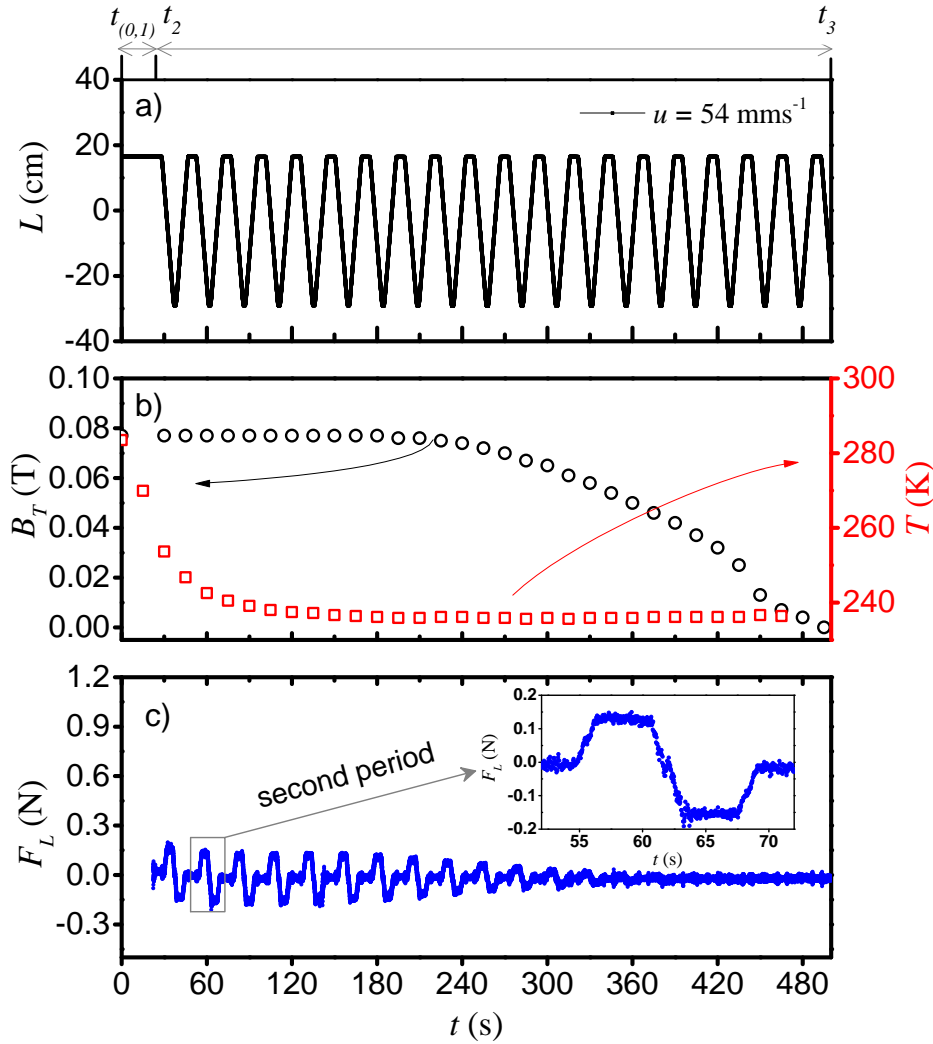
Figure 4.3:
> **a**) An example of the periodic rod motion $L(t)$ with a velocity of $u = 54\,\text{mm}\,\text{s}^{-1}$. The time sequence of the experiments is indicated as follows: $[t_0 = 0; t_1 = 5\,\text{s}]$ - extraction of the bulk HTS MS from the LN_2 bath; $[t_1 = 5\,\text{s}; t_2 = 23\,\text{s}]$ - coupling with the force sensor and start of the motion of the rod; $[t_2 = 23\,\text{s}; t_3 = 500\,\text{s}]$ - LFV measurements, $[t_3 = 500\,\text{s}]$ - stop of the motion and decoupling of the bulk HTS MS.
> **b**) Trapped field B_T at a distance of $7\,\text{mm}$ from the surface of one bulk HTS as function of time t. The field was recorded by a Hall probe right after the HTS MS was pulled out from LN_2 container. In addition, the time dependent temperature behavior of the load cell $T(t)$ (see the arrow, different scales are used) is included.
> **c**) The Lorentz force F_L as a function of time t which acts on HTS MS upon repetitive movement of the metal rod.
> *Inset:* Measured data for $F(t)$ for the second period.

Figure 4.3 b) shows the time dependent data for $B_T(t)$ and $T(t)$ (see the arrow, different scales are used) in the gap of the MS in the vicinity ($z \approx 25\,\text{mm}$, equivalent to $7\,\text{mm}$ from the bulk surface) of the one bulk HTS. $B_T(t)$ remains almost constant up to $240\,\text{s}$, and then gradually reduces to zero due to warming at RT and flux creep. Although, the direct temperature measurement of the bulk HTS during the $F_L(t)$ experiments was not performed, its influence on the HTS bulks is indirectly included in the measured $B_T(t)$ dependence. Still, in order to obtain a correct force signal, the temperature of the load cell was measured: $T(t)$ drops at the beginning from RT down to $240\,\text{K}$ and remains constant.

Figure 4.3 c) shows an example of the measured Lorentz force $F_L(t)$ for the prescribed velocity of $54\,\text{mm\,s}^{-1}$. $F_L(t)$ exhibits a periodic step function behavior with anticipated attenuation due to the above effects. At the beginning, a steep decrease of the amplitude of $F_L(t)$ is attributed to the temperature drop, while gradual attenuation is consistent with the change in $B_T(t)$. Obtaining experimental data under the conditions of constant $B_T(t)$ and $T(t)$ is important, since any changes strongly influence the F_L measurements [16]. Therefore, the estimation of the Lorentz force was calculated for the second period of metal rod motion (see Figure 4.3 c) and its inset), where $B_T(t)$ and $T(t)$ are nearly constant.

The detailed $F_L(\text{t})$ response of the metal rod for the second period is presented in the inset of Figure 4.3 c). Initially, the force is zero, when the metal rod is not moving. Then the metal rod approaches the bulk HTS MS resulting in an increase in F_L. Stationary motion of the metal rod through the bulk HTS MS results in a plateau-like $F_L(t)$. Afterwards, the metal rod reverses the direction, yielding an analogous but negative force. Admittedly, some asymmetry between the positive and negative force signals arises because of asymmetric up- and down-movement (i.e. along z-axis) and off-axis alignment (i.e. along x-axis and/or y-axis), as was stressed in [209].

4.3 Numerical Model

Numerical modelling is a powerful tool to validate and interpret experimental results and is useful for predicting the performance of bulk superconductors in practical applications [101]. To validate the experimental results in this work, a fully 3D model based on the finite-element method (FEM) was implemented using the AC/DC module of COMSOL Multiphysics® 5.3a. The geometry of the model is shown in Figure 4.4, with the same dimensions as the experimental setup described in Section 4.2. The electromagnetic properties of the bulk HTS magnets and the metal rod are implemented
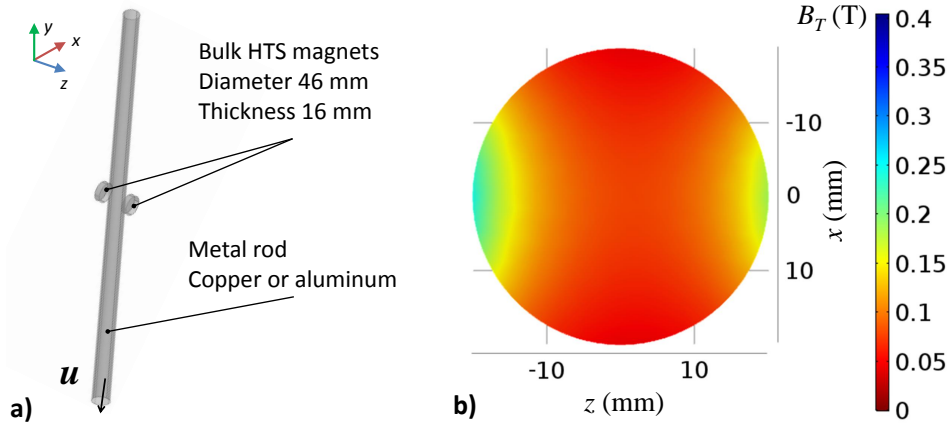
Figure 4.4: **a**) Fully 3D model for the numerical simulation of the fundamental LFV proof-of-concept. The bulk HTS magnets are assumed to be fully magnetized, carrying a constant J_c corresponding to the trapped field measurements of each bulk (see Figure 4.2 a). The movement of the metal rod through the magnets is simulated by applying a velocity (Lorentz term) to the rod subdomain. **b**) Magnetic flux density within the rod cross-section aligned with the center of the bulk HTS MS. The calculated magnetic flux density is consistent with the experimental results shown in Figure 4.2 b).

using the AC/DC module's Magnetic and Electric Fields (mef) interface, satisfying Ampere's law:

$$\nabla \times \vec{H} = \vec{j} \tag{4.1}$$

and current conservation, such that

$$\nabla \cdot \vec{j} = 0 \tag{4.2}$$

The bulk HTS magnets are assumed to be fully magnetized, utilizing the 'External Current Density' node to assume a current density of constant J_c [210]. The value of j_c for each magnet is determined from the experimental trapped field measurements of the bulks (see Figure 4.2 a), where $B_{T,1} = 1.08\,\text{T}$ and $B_{T,2} = 0.8\,\text{T}$, and the following equation based on the critical state model presented by Bean [42, 43] and application of the Biot-Savart law [210] (see also Section 2.1.3.3):

$$B_T = k\mu_0 j_c R. \tag{4.3}$$

In contrast to Eq. 2.9 this equation includes k, which is the correction factor to the simple Bean (slab) approximation due to the finite thickness, t, of a disc-shaped bulk

superconductor:

$$k = \frac{t}{2R} \ln\left(\frac{R}{t} + \sqrt{1 + \left(\frac{R}{t}\right)^2}\right) \tag{4.4}$$

This results in an average, in-field J_c for the two bulks of $j_{c,1} = 9.9 \times 10^7\,\mathrm{A\,m^{-1}}$ and $j_{c,2} = 7.33 \times 10^7\,\mathrm{A\,m^{-1}}$. The resultant magnetic flux density within the rod cross-section across the center of the bulk HTS MS is shown in Figure 4.4 b). The calculated magnetic flux density is consistent with the experimental results shown in Figure 4.2 b).

The movement of the metal rod through the magnets is simulated by applying a "Velocity (Lorentz term)" condition to the metal rod sub-domain in COMSOL Multiphysics®, such that

$$\vec{J} = \sigma(\vec{E} + \vec{u} \times \vec{B}) \tag{4.5}$$

Finally, the force is calculated by

$$\vec{F_L} = \int_V F_y \cdot dV = \int_V (B_x J_z - B_z J_x) \cdot dV \tag{4.6}$$

The calculated force for the two rods for different rod velocities is compared with the experiments in the following section (see Figure 4.5 a).

4.4 Results and Discussion

With the aim to scale the force and the velocity according to Eq. 3.1, a set of LFV measurements with prescribed mean velocities u were carried out. In the case of the copper rod, $u = [54;\ 64;\ 76;\ 81]\ \mathrm{mm\,s^{-1}}$, while for the aluminum rod: $u = [70;81]\ \mathrm{mm\,s^{-1}}$. The results of the Lorentz force measurements obtained experimentally with those calculated numerically are plotted against the velocity for the aluminum and copper rods in Figure 4.5 a). F_L is linearly dependent on the velocity and the electrical conductivity of the moving metal rods, which is consistent with theory (see Eq. 3.1) [1]. Additionally, the F_L values obtained with same-sized copper and aluminum rods for one prescribed velocity, e.g. $u = 81\ \mathrm{mm\,s^{-1}}$, scales as σ_{Cu}/σ_{Al}. Unfortunately, in case of aluminum, the induced Lorentz force approaches the resolution limit of the current simple LFV setup and therefore can result in significant measurement errors.

Furthermore, it is shown that the experimental and simulation results agree well, validating the numerical model (time independent, 3D) as a fast and accurate tool to predict the LFV performance. Thus, the expected F_L with respect to the electrical conductivity of relevant fluids, e.g. solid metals, acids/base and glass melts can be estimated in accordance with Eq. 3.1. It should be noted that the F_L values are valid
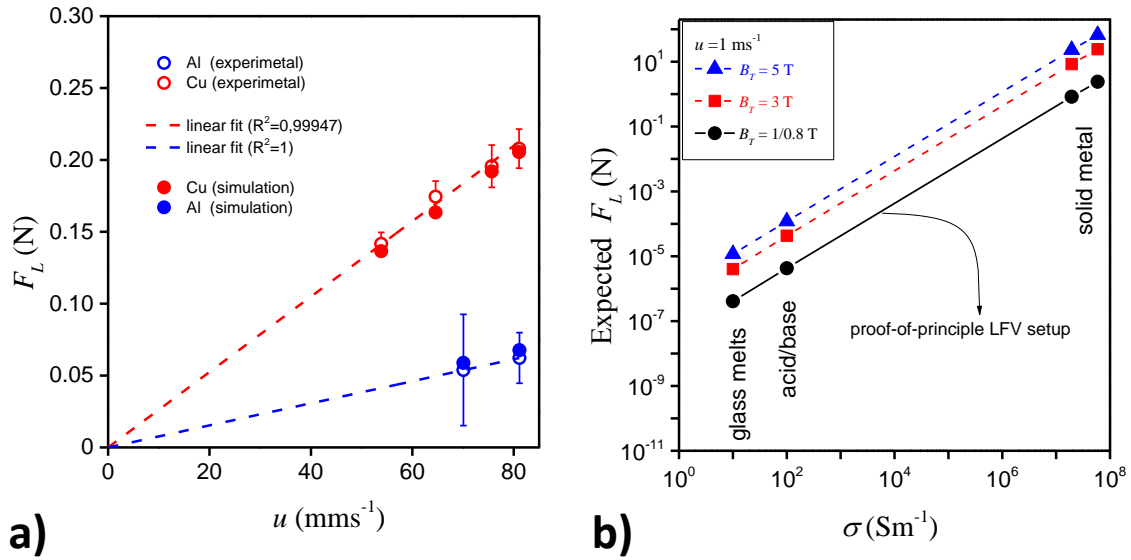
Figure 4.5: **a)** Lorentz Force F_L as function of a velocity u for the copper and aluminum rods. Open circles indicate the experimental results, and the solid circles indicate the simulation results. The dashed lines indicate the linear fit to the experimental results. **b)** Expected Lorentz forces as function of electrical conductivity for relevant fluids, e.g. solid metals, acids/base and glass melts.

only for our particular design of the proof-of-principle LFV setup (see Figure 4.1 a) and may vary for each individual system differently. In particular, the spatial distribution of the magnetic flux density within the interaction volume of the moving conductor. Figure 4.5 b) shows the expected F_L as a function of the electrical conductivity. With use of present proof-of-principle LFV setup (bulk HTS trap $B_T = 0.94$ T, i.e. the average of $1.08/0.8$ T), the generated forces for weakly-conducting and slow-flowing fluids are in the range of µN and below. In particular, $F_L \approx 1 \times 10^{-6}$ N for acids/bases and $F_L \approx 1 \times 10^{-7}$ N for glass melts. It is immediately clear that the use of the bulk HTS MS with higher trapped fields of 3 T and 5 T enhance the resultant F_L over an order of magnitude and thereby the F_L-resolution. This provides evidence that the bulk HTS MS is feasible and serves as a starting point for the future development of a new LFV demonstrator with improved performance.

Still, for practical LFV application to electrolytes, a high-precision force measurement in combination with the bulk HTSs is required.

4.5 Chapter summary

This chapter verifies the use of a bulk HTS MS in LFV using an experimental setup, where the Lorentz force, acting on the moving metal rod, is measured by a load cell that carries the bulk HTS MS. The important conclusions are summarized as follows:

1) The obtained experimental and numerical simulation results agree well, exhibiting the linear relationship between the Lorentz force and product of the electrical conductivity and velocity, in accordance with LFV theory [1].

2) A simple, time-independent 3D numerical model has been developed as a fast and accurate tool to predict the LFV performance. In contrast to the previous model of the second Ph.D. generation, it determines j_c using well-established Bean formulation with the correction factor due to the finite thickness. Nevertheless, dynamic model should be developed in the future that can consider more detailed superconducting properties, including different magnetization process and flux creep effects,

3) To measure velocity of low-conducting electrolytes with $(\sigma \cdot u) = 10\,\mathrm{S\,s^{-1}}$, trapped magnetic flux densities $B_T = 3\,\mathrm{T}$ is required.

Hence, these results serve as a starting point for the future development of a new LFV system with improved performance.

5 Design of new LFV system using bulk HTS

5.1 Introduction and initial specifications

The previous chapter successfully verified the use of bulk HTS technology for LFV applications using simplified LN_2 cooling, but a designer of the improved LFV system must to:

1) generate a stronger trapped field using bulk HTSs,

2) replace the used load cell with the actual FMS – Torsion Force Measurement System (TFMS) [22].

3) integrate the bulk HTS technology with the TFMS considering appropriate bulk HTS magnetization and cooling as well as complying with the TFMS requirements.

To achieve above requirements, the detailed specifications of bulk HTSs and the developed TFMS are considered in the next sections.

5.1.1 Bulk HTSs

Generating high trapped fields and being able to reproduce them (in repeated experiments on the same sample without failure) was a vital next step in using bulks HTS in LFV applications. Despite the long history of developing multi-tesla bulk HTSs [21, 104, 144, 147] (see also Chapter2), it was required to explore the trapped-field capability of bulk HTSs, refining their operating parameters as well as tailoring it to the LFV needs.

Commercial off-the-shelf Y-Ba-Cu-O bulk HTSs from ATZ® [86] were selected for testing and final construction of the bulk HTS-based MS[1]. A series of experiments were conducted at the NFMFL at Florida State University, Tallahassee, USA [102] to:

1) define the mechanical stability and reproducibility of used bulk HTSs and the design required reinforcement,

2) determine the maximum trapped field, identifying the required applied magnetic field B_A and an operating temperature T_{op}

Reinforcement. As introduced in Section 2.2.9, the mechanical stability, rather than superconducting properties is a severe problem for realizing the practical high-field bulk HTSs applications. Among reinforcement strategies [21, 104, 144, 153], an external encapsulation with a stainless steel (AISI 304) tube is a simple and forceful technique [21, 104], whereas other approaches [144] require extra processing and higher production costs.

Still, a record B_T values were achieved once, but were not reproduced with the same sample due to the failure during re-magnetization [21]. The failures were caused by crystal defects (e.g grain boundaries, crystalline defects, voids, cavities, etc.) that emerged in the bulk Y-Ba-Cu-O material during TSMG. These defects are randomly distributed in the volume and can act as weak points during mechanical stresses. Another weak point, however, is imperfect mating between the bulk HTS side surface and the steel tube wall [21, 211]. This implies that the steel tube reinforcement demands a high-precision machining of the bulk HTS and steel tube to provide perfect circumferential interface between them.

Furthermore, using AISI 304 steel has a complementary adverse effect: during first and cycling cooling or upon welding AISI 304 steel can transform into a martensitic phase, which is ferromagnetic [99]. For high-field applications therefore, it is advantageous to use AISI 316[2] steel, since it is less sensitive to ferromagnetic transition during cooling and welding [99]. However, AISI 316 steel is less readily available and is hard to machine.

An aluminum alloy is an alternative choice when machinability is a concern. Furthermore, it has even lower magnetic susceptibility (i.e. $\chi \approx 1 \times 10^{-5}$ at 77 K [99]) than AISI 304/316 steels (cf. Table 5.3). The thermal expansion coefficient of aluminum is comparable with AISI 304/316 steel, although it has lower yield strength.

---

[1]Provided bulk HTSs were grown using TSMG method and typically exhibit $B_T = 1.1$ T at 77 K [118].
[2]In Germany 316 steel has the material number (Werkstoffnummer) 1.4401.

Admittedly, aluminum has only about one third of the weight of stainless steel, which is a clear benefit for the light bulk HTS MS design, in particular, for those to be used in LFV.

Reinforcement experiments. Using the same measurement procedure, separate measurements of trapped fields were carried out on an individual Y-Ba-Cu-O bulk HTS, reinforced with aluminum (sample-AL) and steel (sample-SS) tubes, respectively. Each sample was encapsulated within the corresponding seamless metal tube with a wall thickness of 2 mm using shrink-fitting. Both tubes were commercially available, but were re-machined to provide precise inner diameter tolerance (up to 10 µm). Then, the tubes were heated to the T_{shrink} allowing samples to fit inside. Table 5.1 summarizes further geometrical and physical parameters of both samples.

Table 5.1: Geometrical and physical parameters of the bulk HTS and and reinforcing tubes.

		sample-AL	sample-SS
Y-Ba-Cu-O			
	Diameter (mm)	28.08	28.09
	Thickness (mm)	15.01	19.40
	B_T at 77 K (T)	1.10	1.13
Reinforcement tube			
	Material	aluminum	stainless steel
	Alloying	EN AW 7075	AISI 316
	Inner diameter (mm)	28.01	28.03
	Tube thickness (mm)	1.60	2.00
Shrink-fitting			
	T_{shrink} (°C)	100	300
	Expansion (mm) /RT $-$ T_{shrink}	0.06	0.10
	Compression		
	σ (T=4 K) (MPa)	- 160	- 650

The experimental procedure involved the FC magnetization, applying B_A with successive cooling to an operating temperature $T_{op} < T_c$ (details about B_A and T_{op} are denoted in Figure 5.1). To measure the magnetic field and temperature, both samples were equipped with an array of Hall sensors (HGT-2101, Lakeshore®)[3] and one temperature sensor (CX-1030-SD, Cernox®/Lakeshore®), as shown in the corresponding inserts of Figure 5.1 a)-b), respectively. To stabilize the temperature, a Manganin

---

[3]Sample-SS has five Hall probes and was separated from the sample surface with a G-10 2.5-mm-thin plate, while Sample-Al has only three Hall sensors, but is glued with Stycast® epoxy directly at the surface.

wire-wound heater radially enveloped the sample. The ramp rate during the B_A ramp up was $0.3\,\mathrm{T\,min^{-1}}$, whereas during ramp down it was $0.1\,\mathrm{T\,min^{-1}}$.

Figure 5.1 compares obtained B_T-distributions for sample-SS and sample-Al, respectively. Obtained trapped fields in both cases achieved peak values of about $6\,\mathrm{T}$ and
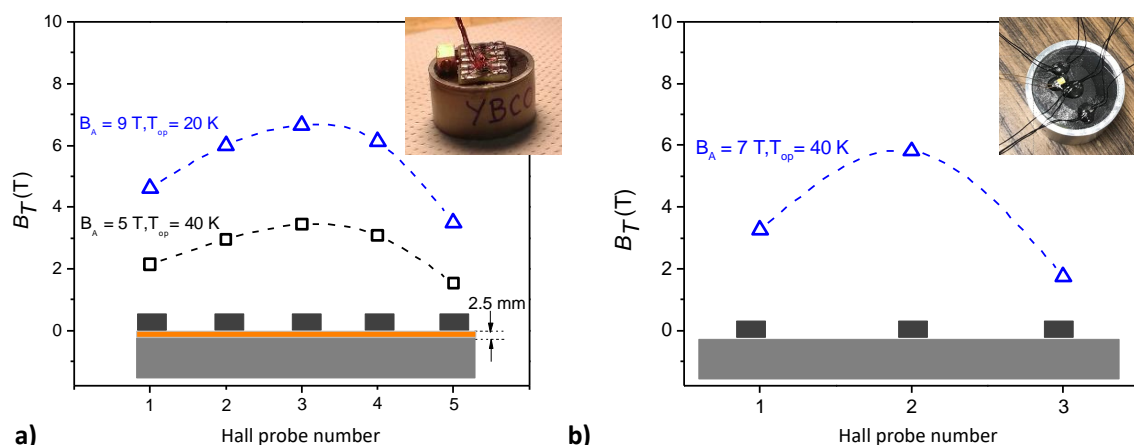
Figure 5.1: The trapped magnetic flux density B_T distributions of the Y-Ba-Cu-O bulk HTS sample followed FC magnetization with $B_A = [5\,\mathrm{T};\, 9\,\mathrm{T}]$, which was reinforced: **a)** with AISI316 steel tube, **b)** EN AW 7075 aluminum tube. *Insert:* corresponding photographs of the sample with Hall probes and Cernox® sensors.

demonstrated clearly that encapsulation with either aluminum or stainless steel tube is equally effective reinforcement for this magnetization parameters. Nonetheless, measured B_T exhibited plane profiles for both samples, suggesting B_T performance can be markedly enhanced when lowering and/or applying higher B_A.

Maximum B_T. To realize a complete flux-trapping capability, measurement on the sample-AL was continued applying higher B_A. Separate trapped field measurements using different FC $(B_A;\, T_{op})$ were conducted as follows:

(1) $B_A = 7\,\mathrm{T}$, $T_{op} = 40\,\mathrm{K}$,

(2) $B_A = 7\,\mathrm{T}$, $T_{op} = 35\,\mathrm{K}$,

(3) $B_A = 9\,\mathrm{T}$, $T_{op} = 25\,\mathrm{K}$,

As a result, Figure 5.2 a) shows that the B_T-distribution evolution followed mentioned magnetization sequences. The maximum trapped field of $7.7\,\mathrm{T}$ was achieved with $B_A = 9\,\mathrm{T}$ at $T_{op} = 25\,\mathrm{K}$. However, during successive magnetization with $B_A = 13\,\mathrm{T}$, the abrupt temperature spike $\Delta T = 30\,\mathrm{K}$ occurred upon removing B_A. It caused the corresponding drop of the measured field at $12\,\mathrm{T}$, as shown in Figure 5.2 b). Such
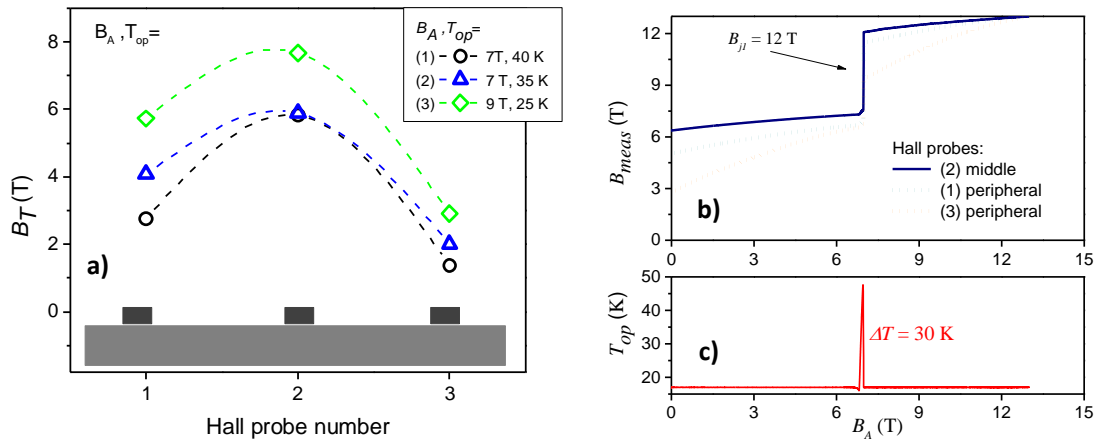
Figure 5.2: **a)** The trapped magnetic flux density B_T evolution of the Y-Ba-Cu-O bulk HTS sample reinforced with EN AW 7075 aluminum tube followed FC magnetization with $[B_A, T_{op}] = [(7\,\text{T}, 40\,\text{K}); (7\,\text{T}, 35\,\text{K}); (9\,\text{T}, 25\,\text{K})]$. **b)** An attempt to trap higher B_T followed the $[B_A, T_{op}] = [12\,\text{T}, 17\,\text{K}]$ showing measured magnetic field B_{meas} as a function of B_A for three Hall probes mounted at the surface: solid line - (2) middle Hall probe, dotted lines (1,3) peripheral Hall probes. Upon B_A ramping down, a drop of the measured field occurred at $B_{j1} = 12\,\text{T}$. **c)** Measured T_{op} as a function of B_A shows an abrupt temperature spike $\Delta T = 30\,\text{K}$ occurred simultaneously with the B_{j1}.

a scenario is the hallmark of the flux jumping phenomenon [21, 147] (see also Section 2.2.9).

In order to identify whether this flux jump had any aftermath, the sample was immediately re-magnetized using a $B_A = 12\,\text{T}$ at $T_{op} = 16\,\text{K}$, but the flux jump occurred again at about 1 T. The visual inspection that followed did not indicate any obvious damage.

Summary. The used commercially available Y-Ba-Cu-O bulk HTSs with relatively simple reinforcement can trap the magnetic field up to 7.7 T at its surface at $T_{op} = 25\,\text{K}$. Higher trapped fields were limited by the mechanical and thermo-magnetic stability. In comparison, the Y-Ba-Cu-O samples that are grown according to the optimal thermo-dynamic approach [212] and exclude any post-treatment for mechanical stabilization were able to trap $B_T = 5\,\text{T}$. The record $B_T = 11.2\,\text{T}$ was achieved only once (but not reproduced) for specially processed Y-Ba-Cu-O bulk HTSs (e.g. doped with Zn and alloyed with silver) [20].

The encapsulation with either an aluminum or stainless steel tube is an equally effective reinforcement. The utilized bulk HTSs were able to generate the reproducible field in the range of 6 T to 7 T. However, operating temperature $T_{op} = 20\text{-}50\,\text{K}$ must

be achieved.

5.1.2 Torsion Force Measurement System (TFMS)

During the second RTG generation, the developed FMS – DEMFC – reached the force resolution of 20 nN. However, due to mass and construction limitations, it cannot be integrated with bulk HTS MS (cf. Section 3.3.5). Therefore, the third RTG generation aimed to further develop the FMS that:

1) enables the force resolution of 1 nN,

2) and is compatible with the bulk HTS technology.

A general strategy to fulfill the stated aim was to measure force using a torsion balance technique. The first step was to develop a Torsion Force Measurement System (TFMS), which can achieve the force resolution of 1 nN at RT.

Initial design and working principle.   The TFMS design and technical aspects were proposed in [213] and were developed in a parallel Ph.D. project by Na Yan [22].

Figure 5.3 a) shows the CAD-model of the TFMS adopted for LFV measurements. It consists of (1) MS (e.g. Halbach PMs), (2) plane-wheel, (3) dummy counterweight, (4) flexure bearing, (5) conical couplings, (6) position sensor, (7) base plate, and (8) channel.

For LFV measurements, the Lorentz force (shown as F_L) acts on the MS that is mounted onto the plane-wheel. This causes the wheel to rotate, which is then detected by the position sensor, the working principle of which will be presented in Section 5.2.4.

Specifications.   The TFMS has a rotating structure, where the plane-wheel carries MS and dummy counterweight. The counterweight has similar geometry and identical mass as the MS. Furthermore, the arm length of the dummy counterweight L_1 is equal to the MS arm length L_2, as schematically indicated in Figure 5.3b). It is expressed as:

$$m_1 \cdot L_1 = m_2 \cdot L_2, \tag{5.1}$$

where m_1 and L_1 are mass and arm length of dummy counter weight, whereas m_2 and L_2 - measures of the MS. Eq. 5.1 claims that TFMS's center of gravity goes through the rotational axis (y-axis). In this sense, TFMS is insensitive against the tilt. It is drastically different from the weighting cells (e.g. EMFC, cf. Section 3.3.2), where
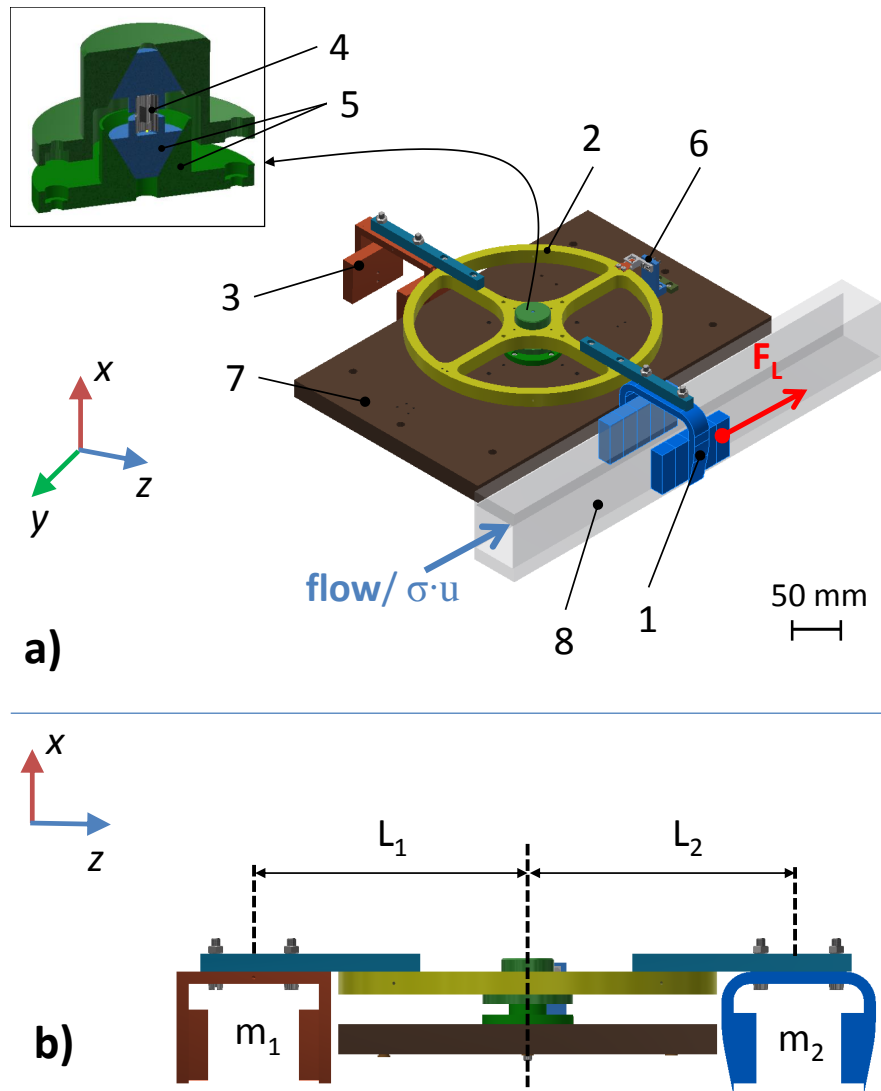
Figure 5.3: **a)** Proposed CAD-model of the TFMS - third generation of FMS - and its arrangement at the channel. It consists of (1) MS (e.g. Halbach PMs), (2) planewheel, (3) dummy counterweight, (4) flexure bearing, (5) conical couplings, (6) position sensor, (7) base plate, and (8) channel. **b)** Front view of TFMS, where length of lever arms as well as mass for dummy counterweight and MS are indicated. CAD-model is adopted by permission of Na Yan [22].

tilting effects in a combination with the dead load induce significant measurement errors [22, 214].

Geometrical parameters (i.e. arm length of $L_{1,2} = 180\,\text{mm}$) and choice of the bearing were determined to provide the low value of the TFMS effective stiffness, and to achieve desired force resolution of $1\,\text{nN}$ [22]. Thus, a commercial flexure bearing (C-Flex pivot bearing, D-10) [215] with the stiffness of $1.17 \times 10^{-2}\,\text{N}\,\text{m}\,\text{rad}^{-1}$ was selected. Further

details of the flexture bearing will be discussed later in Section 5.2.4. Furthermore, this bearing was encapsulated within (5) conical couplings to avoid possible eccentric overloads and ensure the rotation around the y-axis without friction, inclination, and misalignment.

The flexure bearing can sustain the maximum axial (along y axis) load of about 10 kg (101 N), according to its specifications [215]. This implies that the mass limit for carrying the MS is reduced even further because besides the MS the bearing also carries the dummy counterweight and plane-wheel. Ultimately, the maximum mass for carrying the MS remained in the range of 1-3 kg [22].

Conclusively, TFMS was designed and manufactured in a parallel project [22]. The TFMS feasibility and its components (e.g. positioning sensor) was demonstrated achieving the force resolution of 2 nN under laboratory conditions at RT and without magnetic field influence.

5.2 Super-LOFOS concept

Despite the developed TFMS extends a force resolution, the maximum mass ($m < 3$ kg) for carrying the MS is still limited [22]. The bulk HTS-based MS, on the contrary, requires a heavyweight vacuum cryostat[4] to ensure a practical, robust and long-term operation.

5.2.1 Conflict of mass

In order to integrate the bulk HTS technology with the TFMS, a novel concept – *integrated cooling* – was proposed and developed. To achieve *integrated cooling*, the standard bulk HTS (which weighs 150-500 g) is mounted to the TFMS and both are placed within a cryostat. In this case, the bulk HTS and TFMS are cooled and magnetized together.

The *integrated cooling* is a principally different to the previous concept pursued by the second RTG generation (see Section 3.3.5), where the bulk HTS and FMS are considered as independent sub-systems, and solves the problem of *"conflict of mass"*, enabling the cooling and retaining the bulk HTS at temperatures below 77 K. Hereafter, the *integrated cooling* concept is referred to as a **Super**conducting High-precision **Lo**rentz **Fo**rce Measurement **S**ystem (Super-LOFOS).

---

[4]As discussed in Section 2.2.2, a vacuum cryostat for the bulk HTS weighs about 10 kg, due to heavyweight vacuum vessel and a cooling device (see also Table 2.1).
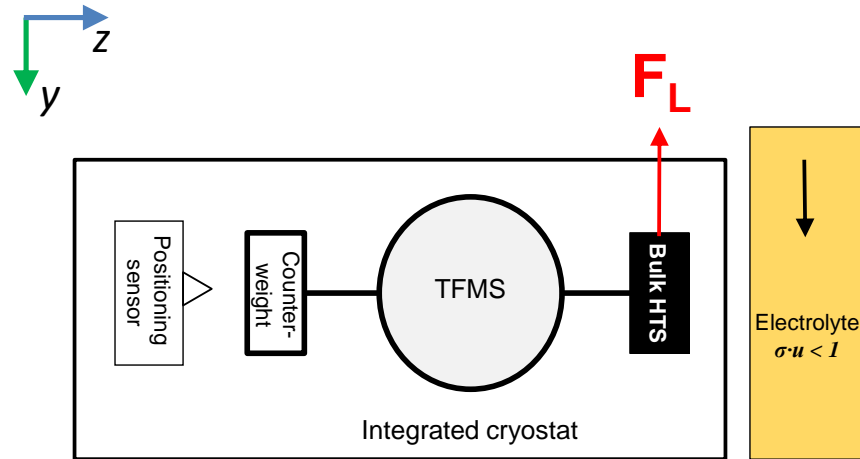
Figure 5.4: The concept of a new, improved LFV system in the vicinity of the electrolyte channel.

The idea of Super-LOFOS was patented by the author *et al* [216] and its concept is presented in Figure 5.4. Instead of Halbach MS, the bulk HTS is attached to the one side of the TFMS lever, while a counterweight, whose mass is equal to the mass of the bulk HTS with comparable geometrical dimensions, is attached on the opposite side. Both systems, bulk HTS and TFMS, are placed in the integrated cryostat, cooled and magnetized simultaneously. Once magnetized, the bulk HTS acts as the TFM, whose B_T is arranged transversely to the measuring channel. Then, force measurements are performed in the same manner as described in the previous section.

However, in the case of *integrated cooling* (when the bulk HTS is attached to the sTFMS) the solid conductive cooling presents a challenge: A direct thermal connection of the bulk HTS with a cold head of a cryocooler or cryogenic liquid tank contradicts with the working principle of sTFMS (i.e. restriction of the rotation) and required an alternative thermal coupling.

5.2.2 Cooling Super-LOFOS: solid-plus-gas conduction

To alleviate the cooling challenge, the solid conductive cooling (cf. Section 2.2.7) was modified to include a gas conduction, which is an effective method to refrigerate the irregularly shaped devices [99]. In this case, TFMS with bulk HTS was placed in a closed single-walled vessel which was filled with thermally-conducting exchange gas. The vessel was then thermally anchored to the cold surface of the cryogenic liquid tank, thereby forming a *solid-plus-gas* conduction.

Alternatively to the cryogenic liquid tank, cooling with cryocoolers was also con-

sidered. However, cryocoolers introduce vibrations which are harmful for the force measurements in the nano-newton range. Furthermore, cryocoolers might operate improperly in high magnetic field (cf. Section 2.2.7.2). Thus, the *solid-plus-gas* conduction for the LFV system used the cryogenic liquid for refrigeration.

The *solid-plus-gas* conduction of Super-LOFOS was realized as a modular structure, which includes:

1) a cooling cryostat storing a liquid coolant, for example LHe,

2) a measuring cryostat housing the HTS and the TFMS.

The simplified schematic of such a modular structure is displayed in Figure 5.5. The cooling cryostat represents the cryogenic liquid tank (cf. Section 2.2.7) with the LHe, which is thermally joined with the measuring cryostat via the solid conduction. The measuring cryostat contains the bulk HTS/sTFMS and is filled with an exchange gas to provide contactless cooling of the bulk HTS. Both cryostats are placed in a vacuum to ensure thermal isolation.
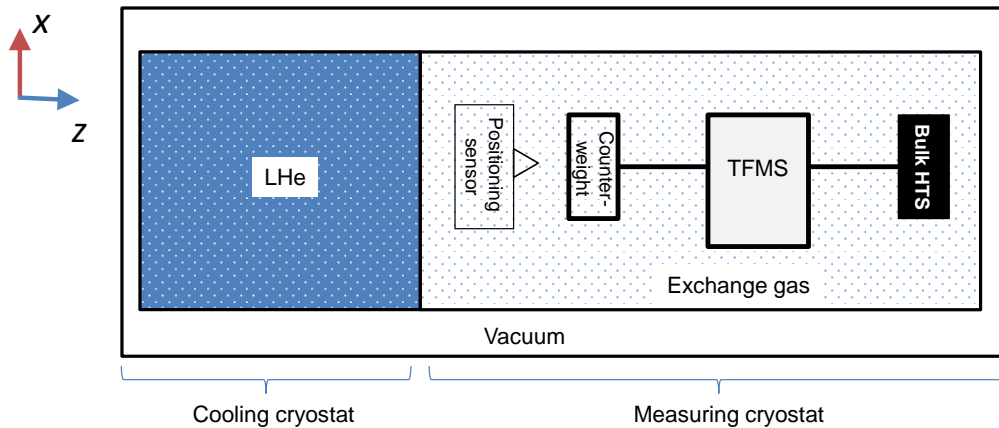
Figure 5.5: The concept of a *solid-plus-gas* conduction for Super-LOFOS, which includes cooling cryostat with LHe and measuring cryostat with an exchange gas.

5.2.3 Magnetizing Super-LOFOS

A superconducting magnet (5TCFM) [202] available at TU Ilmenau was utilized for the FC/ZFC magnetization of the bulk HTS. Figure 5.6 a) shows the 5TCFM, which has the room-temperature bore of 300 mm in diameter and 400 mm in length. The 5TCFM is capable of providing a maximum field of 5 T in the middle of the bore meaning that the maximum trapped field of Super-LOFOS can reach the value of nearly the same

or slightly lower than $B_T \approx B_A = 5\,\text{T}$. This value is below the maximum trapping capacity (i.e. $B_T = 7.7\,\text{T}$, Section 5.1.1) of used bulk HTS and therefore allows for a robust and reliable generation of the magnetic field for the LFV. Furthermore, the bulk HTS of a cylindrical form can be embedded with the aluminum tube, thereby reinforcing it and serving as the sample holder.
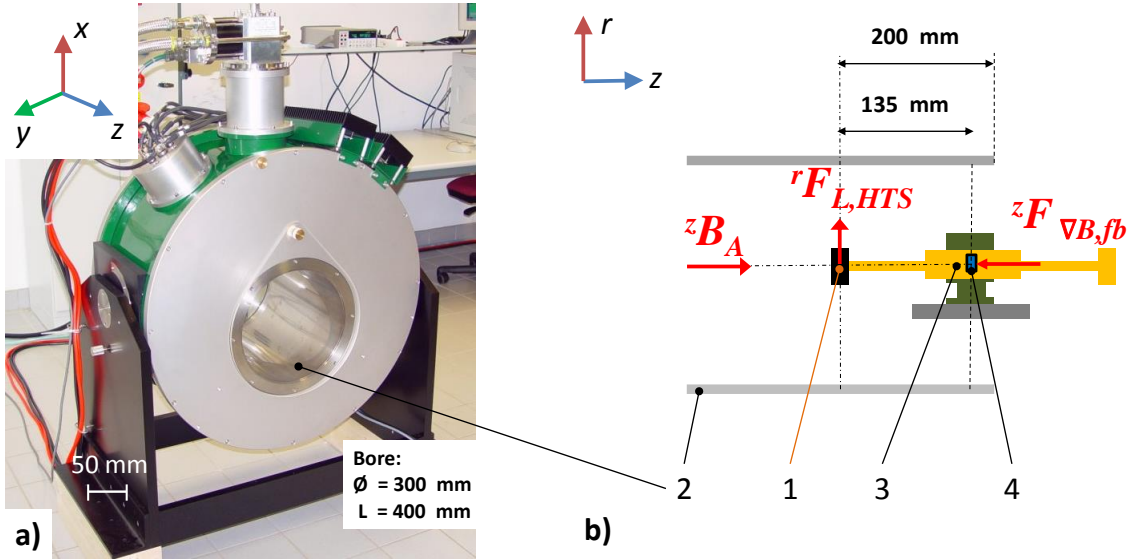
Figure 5.6: **a)** The 5TCFM superconducting magnet [202], which has the room-temperature bore of $300\,\text{mm}$ in diameter and $400\,\text{mm}$ in length and provides the maximum field of $5\,\text{T}$ in the middle of the bore. **b)** The schematic of (2) the magnetic bore in the r-z plane, where the (1) bulk HTS integrated with the (3) TFMS is placed in the middle of the bore. During the magnetization, electromagnetic forces $F_{L,HTS}$ in the radial direction are exerted on the (1) bulk HTS, and magnetic vector gradient forces $F_{\nabla B,fb}$ are exerted on the (4) flexure bearing in the z-direction.

During magnetization, the TFMS is placed in the 5TFCM bore, as shown in Figure 5.6 b). Consequently, following magnetic forces are exerted:

1) Lorentz force $\vec{F}_{L,HTS}$ on the bulk HTS at $T < T_c$[5],

2) magnetic vector gradient force $\vec{F}_{\nabla B,fb}$ on the flexure bearing, since it is made of ferromagnetic material [215].

---

[5]For the case $T > T_c$, the magnetic gradient force $\vec{F}_{\nabla B,HTS}$ is neglected due to the low magnetic susceptibility of the Y-Ba-Cu-O bulk HTS due to the low gradient of the magnetic field B_A in the middle of the room temperature bore.

Bulk HTS Lorentz force. The Lorentz forces acting on bulk HTS at $T < T_c$ can be calculated as:

$$\vec{F}_{L,HTS} = (\vec{j_c} \times \vec{B_A})V, \qquad (5.2)$$

where $\vec{j_c}$ is the induced critical current density in the bulk HTS, $\vec{B_A}$ is the applied magnetic flux density, and the V is the volume of the bulk HTS.

To estimate the Lorentz force, it was assumed that the bulk HTS is located within the homogeneously applied magnetic flux density $\vec{B_A}$ (i.e. $B_A = {}^z B_A$). It was furthermore assumed that the bulk HTS current density ${}^\theta j_c$ is determined by Eq. 2.9 (according to the Bean model, see Section 2.1.3.3). In this case, the maximum Lorentz force has only the radial component and is expressed as:

$$^r F_{L,HTS} = {}^\theta j_c \cdot {}^z B_A \cdot V. \qquad (5.3)$$

Using Eq. 5.3, the calculated $^r F_{L,HTS}$ as function of the applied magnetic field B_A are presented in Table 5.2 for the bulk HTS with the diameter of 48 mm and the thickness of 15 mm.

Table 5.2: Calculated Lorentz forces acting on the utilized bulk HTS with the diameter of 48 mm and the thickness of 15 mm during magnetization at $T < T_c$.

B_A (T)	${}^\theta j_c$ (A m^{-2})	$^r F_{L,HTS}$ (N)
1	8.5×10^7	2.3×10^3
2	1.7×10^8	9.2×10^3
3	2.5×10^8	2.1×10^4
4	3.4×10^8	3.7×10^4
5	4.2×10^8	5.7×10^4

Magnetic vector gradient force. Magnetic vector gradient forces are exerted on the flexure bearing (C-Flex pivot bearing, D-10 [215]), since it is made of the martensitic AISI 420 stainless steel. The D-10 flexure bearing has a mass of $m_{fb} = 1$ g [215] and its geometrical parameters are shown in Figure 5.7. The AISI 420 stainless steel is highly ferromagnetic and has a magnetic volume susceptibility of $\chi = 950$ [217].

During magnetization, the flexure bearing – the key TFMS component – is located in a part of the room-temperature 5TFCM bore, where the applied magnetic field B_A is inhomogenous [218] (see Figure 5.6). This, in turn, leads to a magnetic vector
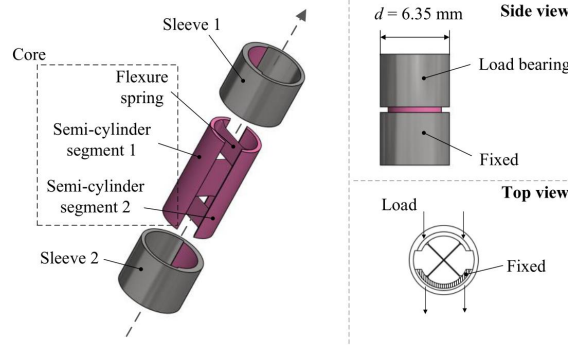
Figure 5.7: Exploded CAD model of the flexure bearing (C-Flex pivot bearing, D-10) [215] with its main parameters. Adopted from [22].

gradient force $\vec{F}_{\nabla B, fb}$ acting on the flexure bearing:

$$\vec{F}_{\nabla B, fb} \;=\; m_{fb} \left(\frac{\chi}{\rho}\right) \frac{((\vec{B} \cdot \nabla)\vec{B})}{\mu_0}, \tag{5.4}$$

where m_{fb} is the flexure bearing mass, χ is the volume magnetic susceptibility and ρ is the density of the material, $((\vec{B} \cdot \nabla)\,\vec{B})$ is the magnetic vector gradient of the magnetic field, $\vec{B}$ is the magnetic flux density, and μ_0 is the permeability of free space.

To estimate the magnetic vector gradient forces, it is assumed that the bulk HTS is located exactly in the middle of the 5TCFM bore (as delineated in Figure 5.6), whereas the flexure bearing is located concentrically (at the z-axis), but $135\,\mathrm{mm}$ distant from the middle of the magnetic bore. For this situation, the magnetic vector gradient has only a z-component and can be approximated:

$$F_{\nabla B, fb} \;=\; {}^z F_{\nabla B, fb}. \tag{5.5}$$

The magnetic gradient force ${}^z F_{\nabla B, fb}$ acting on the utilized AISI 420 steel flexure bearing was then calculated using the available data for the magnetic vector gradient [218, 219] for this particular 5TCFM when $5\,\mathrm{T}$ is applied[6]. The result is presented in Table 5.3, which also summarizes the data for magnetic susceptibility and material density. In order to reduce ${}^z F_{\nabla B, fb}$ acting on the flexure bearing, the flexure bearing must be manufactured from an alternative material with a low magnetic susceptibility ($\chi \ll 1$), e.g. austenitic steel or titanium (see Table 5.3). The manufacture using low-magnetic material, however, will change the flexure bearing's primary parameters,

---

[6]For this particular 5TCFM when $5\,\mathrm{T}$ is applied, the ${}^z((B \cdot \nabla)\,B)/\mu_0 = 56.01\,\mathrm{N\,cm^{-3}}$ was determined using experimental and numerical simulations in [218, 219].

Table 5.3: Magnetic vector gradient forces acting on the flexure bearing during 5 T magnetization.

Material	χ at 293 K	ρ, (kg m^{-3})	$^{z}F_{\nabla B, fb}$,(N)
used flexure bearing			
AISI 420 steel	9.50×10^{2} [217]	7.80×10^{3} [215]	6.82×10^{3}
alternative material for flexure bearing			
AISI 304 steel	2.70×10^{-3} [99]	7.86×10^{3} [99]	1.92×10^{-2}
AISI 316 steel	3.00×10^{-3} [99]	7.85×10^{3} [99]	2.14×10^{-2}
Titanium	1.78×10^{-4} [99]	4.00×10^{3} [99]	2.22×10^{-3}

such as stiffness, rotation angle, and load [215]. Therefore, further investigations of the non-magnetic flexure bearing are being considered for future Super-LOFOS development.

Summary.   By comparing the results presented in Table 5.2 and Table 5.3, both magnetic forces $^{x}F_{L,HTS}$ and $^{z}F_{\nabla B,fb}$ exceed the bearing axial load capacity of 101.1 N [215] and can lead to damage or TFMS functional restriction. Therefore, it was necessary to develop a safety inset of the flexure bearing, which prevents the flexure bearing from overloading during magnetization

In addition, the volume and surface area of the developed TFMS[7] must both be minimized. Otherwise, it would greatly contribute to the cryogenic cryogenic system heat load.

Thus, the TFMS was re-designed and scaled down from the wheel-plane structure to the lever-type structure. The scaled-down Torsion Force Measurement System (sTFMS) retained its key components and the prescribed arm length. The sTFMS design was accompanied by frequent and direct communications between two projects: the current project related to the Super-LOFOS development and the parallel project related to the TFMS development [22].

---

[7]The rotation part of the TFMS has a diameter of about 250 mm.

5.2.4 TFMS re-design

When the sTFMS was conceptualized due to issues discussed in Section 5.2.3, its manufacture and calibration were performed by Na Yan [22]. This allowed the parallel sTFMS development along with the development of Super-LOFOS vacuum and cryogenic components.

Figure 5.8 shows the CAD model and photograph of a new sTFMS, which consists of (1) bulk HTS and its holder, (2) lever, (3) counterweight, (4) flexure bearing, (5) conical
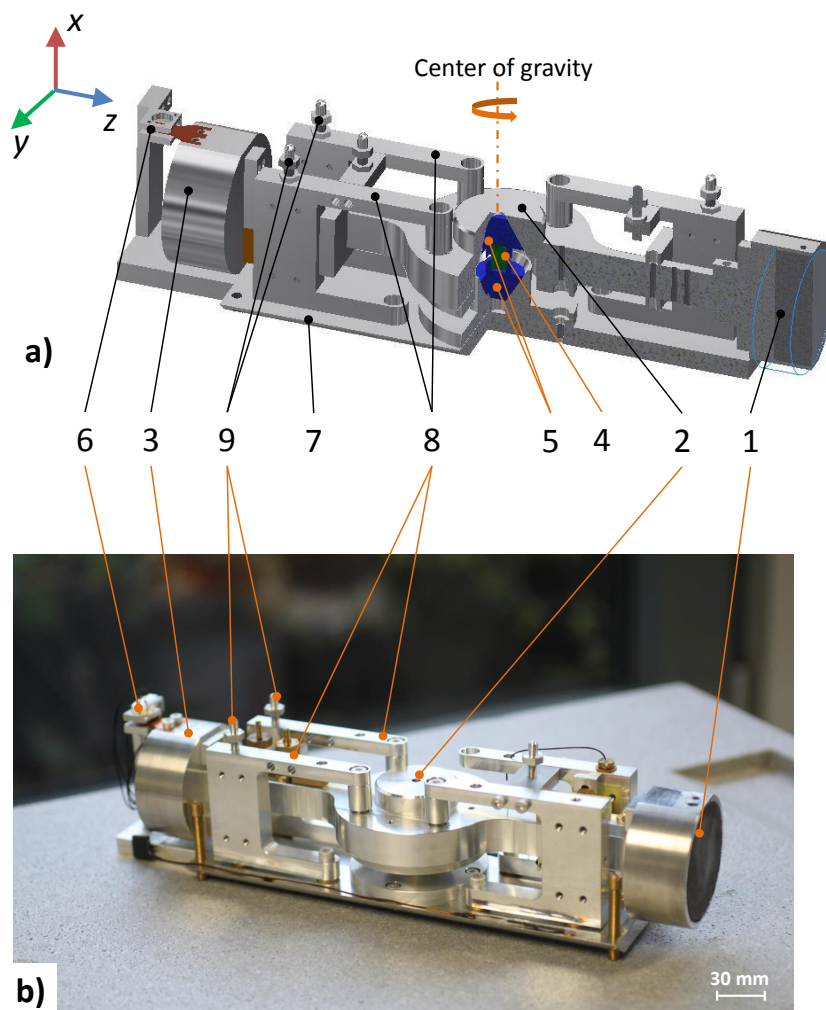
Figure 5.8: The scaled-down Torsion Force Measurement System (sTFMS): **a)** CAD model and **b)** photograph. It consists of (1) bulk HTS and its holder, (2) lever, (3) counterweight, (4) flexure bearing, (5) conical couplings, (6) positioning sensor, (7) support platform, (8) safety limiter for the flexure bearing and (9) screws for fixation. The design, manufacture, and calibration of the sTFMS were done by Na Yan [22].

couplings, (6) positioning sensor, (7) support platform, (8) safety limiter for the flexure bearing and (9) screws for fixation.

The new sTFMS, similar to the previous TFMS, consists of machined components and commercially available off-the-shelf components (i.e. flexure bearing, positioning sensor, and bulk HTS). The former components are made of the aluminum alloy (EN AW 7075), because of the ease of machining. Another important argument for aluminum was its low magnetic susceptibility, which is a strict demand in high-field applications. Also, manufacturing the mechanically complex structure of sTFMS from one material negates a problem related to the difference in thermal contraction upon cooling.

Safety inset of the flexure bearing. In order to secure the bearing from damage due to the magnetic forces (cf. Section 5.2.3), sTFMS was equipped with the (8) safety limiters, which are designed to separate the flexure bearing from the lever. Figure 5.9 sketches the sTFMS and explains the action of safety limiters. When sTFMS is in the measuring position (see Figure 5.9 a) the (2) lever is settled on the (4) bearing and is mechanically decoupled from the (8) safety limiter. In this case, the (2) lever rotates freely around the x-axis according to the expected sTFMS operation. However, when sTFMS is inverted 180° around the z-axis (see Figure 5.9 b), the (2) lever is mechanically anchored via the (8) safety limiter and is separated from the bearing. In this position, the flexure bearing is secured from overloading due to the magnetic forces and can be safely magnetized.

Summarizing, the bearing safety inset during magnetization implies that the sTFMS has to be arranged 0° and 180° regarding the z-axis:

a) *measuring mode*: the sTFMS is in the initial position enabling the free rotation of the sTFMS lever (cf. Figure 5.9 a),

b) *magnetization mode*: the sTFMS is inverted 180° related to its initial position to secure the flexure bearing from damage (cf. Figure 5.9 b).
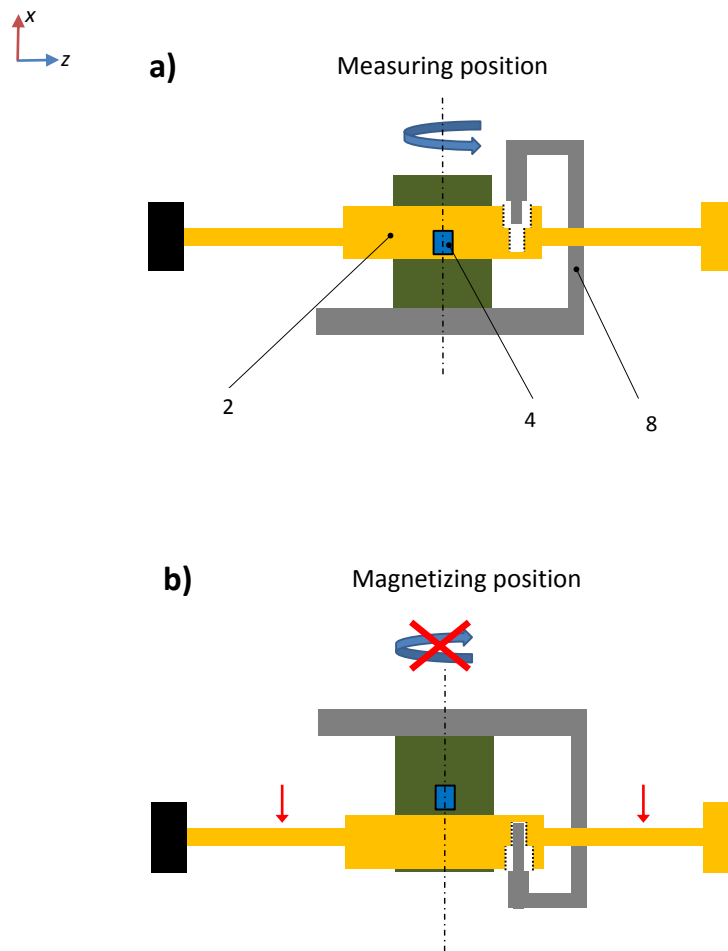
Figure 5.9: The the sketch of the flexure bearing safety inset. **a)** *measuring mode*: the sTFMS is in the initial position enabling the free sTFMS rotation. **b)** *magnetization mode*: the sTFMS is inverted on 180° related to its initial position to secure flexure bearing from damage. Labeling of the components correspond with the CAD-model (cf. Figure 5.8).

Positioning sensor. An optical positioning sensor is a compact solution to measure the position with the high precision in state-of-the-art torsion balances. Figure 5.10 shows the optical positioning sensor used in sTFMS. The position sensor consists of an (6.1) infrared light-emitting diode (LED), (6.2) two-segment differential photodiode, (6.3) aluminum frame, which hold both diodes, and (6.4) aperture, which is fixed to the sTFMS counterweight.

The LED and the differential photodiode are arranged face-to-face to each other and are mechanically fixed at a distance of 2 mm. The LED is excited by applying an excitation current $I_{ex} = 10$ mA, thereby illuminating the differential photodiode through
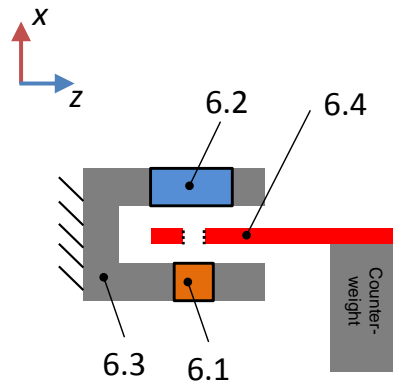
Figure 5.10: Position sensor of the TFMS consists of (6.1) infrared LED, (6.2) two-segment
         differential photodiode, (6.3) aluminum frame, which hold both diodes, and
         (6.4) aperture, which is fixed to the TFMS counterweight.

the movable aperture, which is fixed on the counterweight of sTFMS. The output
voltage ΔV_{ph} of the differential photodiode is then proportional to the displacement of
the aperture.

In the case of the sTFMS, the displacement of the aperture is the rotation of the
(2) lever around its center of gravity, as sketched in Figure 5.8 a). Upon the sTFMS
operation to measure forces, one measures an output voltage ΔV_{ph} of the positioning
sensor, which represents the rotation angle θ[8]. The rotation angle θ is expected to
be calibrated into the force F. The F– θ – ΔV_{ph} calibration is performed using the
controllable step-wise rotation and actuating applied force F_a in the horizontal plane
(cf. Figure 5.8, $y - z$ plane). Further calibration details are available in [22].
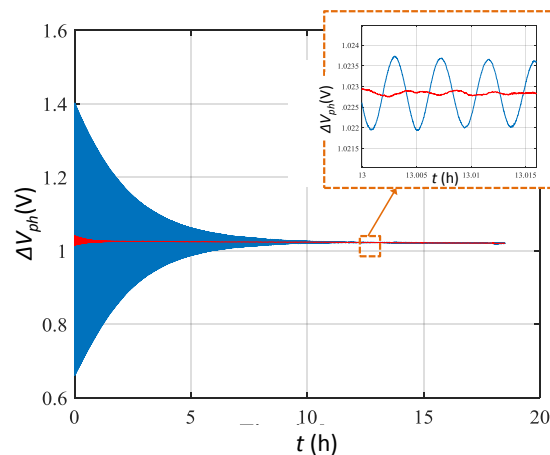
Figure 5.11: Example of an oscillating and damped ΔV_{ph} signal.

---

[8]The maximum rotation angle of $\theta_{max} = \pm15°$ enables force measurements in µN range [22].

When the sTFMS lever is perturbed (e.g. by applying a force), the sTFMS lever starts to rotate with the subsequent attenuation. This resembles a second-order mass-spring-damper and is reflected as a damped oscillating ΔV_{ph} signal, see Figure 5.11.

5.2.5 Super-LOFOS requirements

This section paid attention to the design of a novel LFV system using bulk HTS - Super-LOFOS addressing the operational and technical issues, such as:

1) bulk HTS specifications,

2) sTFMS specifications,

3) cooling below 77 K,

4) magnetization,

5) integration as a holistic system.

As a result, Table 5.4 summarizes Super-LOFOS requirements. In addition, it is also desired that the Super-LOFOS operates for 2 h, is portable ($m < 50$ kg), and with a design that is flexible enough to adjust to any available facility or to any future modifications.

Table 5.4: Summary of the requirements for the Super-LOFOS based on bulk HTSs and sTFMS.

	Requirements	Metric
General	Operation duration	> 2 h
	Portable	< 50 kg
	Easy maintenance/handling	
bulk HTS	Commercial Y-Ba-Cu-O	
	Reinforcement	encapsulation in aluminum tube
	Maximum field generation	$B_T = 5$ T
	Magnetization bore	$\varnothing = 300$ mm
	FC/ZFC magnetization	$B_A < 5$ T
	LN$_2$ pre-cooling	$Top = 77$ K
	LHe cooling	$Top = 50$ K
developed sTFMS	Force resolution	1 nN
	T-range operation	$T < 300$ K
	B-range operation	$B < 5$ T

5.3 Super-LOFOS design and manufacture issues

The Super-LOFOS design started with the *solid-plus-gas* concept, followed by the materials/components selection, and mechanical and manufacture considerations. Sec-
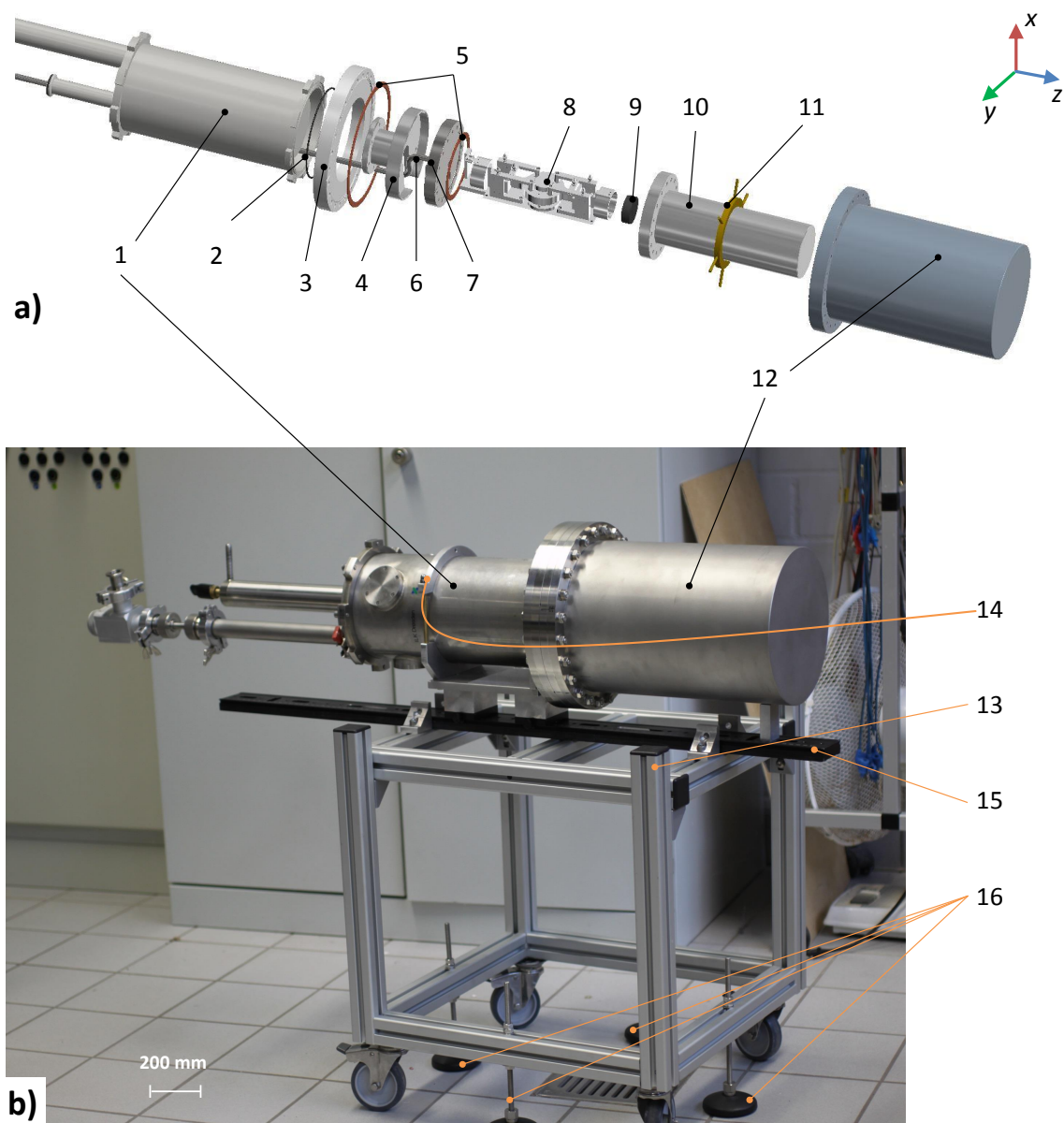
Figure 5.12: **a)** The exploded CAD model of the Super-LOFOS comprised of (1) cooling cryostat, (2) Viton® O-ring, (3) flange adapter, (4) aluminum thermal link, (5) copper seals, (6) He-line, (7) blind flange (8) sTFMS, (9) bulk HTS, (10) cryogenic force cell, (11) mechanical support and (12) outer vacuum vessel. **b)** Photograph of the assembled Super-LOFOS, which is fixed to the (13) transport table with (16) four swivel feet and fastened with the (14) security clamp and is firmly fixed to an (15) optical slab.

tion 5.3.1 outlines the structure of the Super-LOFOS, while Sections 5.3.2-5.3.3 describe its main components in detail.

5.3.1 Super-LOFOS outline

Figure 5.12 a) shows the exploded CAD model of Super-LOFOS that includes (1) cooling cryostat, (2) Viton® O-ring, (3) flange adapter, (4) aluminum thermal link, (5) copper seals, (6) He-line, (7) blind flange (8) sTFMS, (9) bulk HTS, (10) cryogenic force cell, (11) mechanical support, and (12) outer vacuum vessel.

Retaining the previous mounting system, Super-LOFOS was fixed at the (13) transport table as shown in Figure 5.12 b). The mounting here means that Super-LOFOS is fastened with the (14) security clamp and is firmly fixed to an (15) optical slab. The hight of the transport table can be regulated, whereas the level is adjustable using (16) four swivel feet.

5.3.2 Cooling cryostat

One previously mentioned LHe/LN_2 bath cryostat, used in the previous studies on bulk HTS for LFV (cf. Section 3.3.5), was utilized as the cooling cryostat for the Super-LOFOS. This cryostat was designed and manufactured by ILK Dresden [204] and is shown in Figure 5.13. It consists of (1) the outer vessel for vacuum isolation, (2) the inner vessel containing cryogenic liquid ($V = 1.5\,l$), (3) the multi layer isolation, (4) three ISO-KF ("Kleinflansch") vacuum ports, (5) the filling line, and (6) the blind flange.
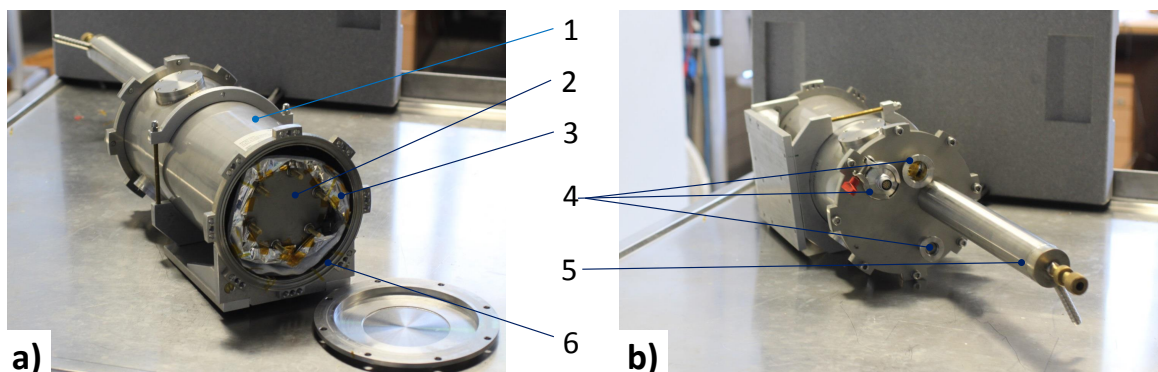
Figure 5.13: Front **a)** and Rear view **b)** of the Cooling Cryostat consisting of (1) outer vessel for vacuum shroud, (2) inner vessel containing cryogenic liquid ($V = 1.5\,l$), (3) multilayer isolation, (4) filling line, (5) three CF ports and (6) front blind flange.

The blind flange is a ConFlat® (CF) flange [220]. Two of three ISO-KF ("Kleinflansch") [221] vacuum ports are used for a vacuum pumping and electrical feedthrough, while one remained redundant. Both types of flanges have a sexless design, whereas their sizes are determined by the nominal internal diameter of the largest tube that can be welded to a bored flange [220][9]. CF flanges operate in a wider pressure range and, more importantly, are qualified for cryogenic temperatures [99, 220, 221].

Arguments for accommodating the LHe/LN$_2$ cryostat into the Super-LOFOS included:

1) opportunity of cooling down to 5 K using LHe,

2) possibility of thermal joining with measuring cryostat,

3) available redundant CF port allowing for the exchange gas supply and auxiliary wire leads,

4) savings on manufacture time and cost implications.

The LHe/LN$_2$ cryostat was docked on to the measuring cryostat. The vacuum-tight connection was possible via the CF flange, while thermal connection was done via the solid conduction. To realize these, the (3) flange adapter and the (4) aluminum thermal link (see Figure 5.12) were deployed. Additionally, the redundant CF port allowed for an exchange gas supply using a thin tube, which was threaded through the vacuum isolation.

Since the LHe/LN$_2$ cryostat cooling capacity[10] was not provided by the manufacturer [204] and was not investigated in previous studies, the latent heat vaporization L_v of a relevant cryogenic liquid (cf. Table 2.3) at its nominal atmospheric boiling temperature was considered as cooling cryostat capacity. In this case, the LHe/LN$_2$ cryostat cooling capacity depends on the cryogenic liquid, whereas the duration is restricted to the volume of the inner vessel (i.e. 1.5 l [204]). Fortunately, the cooling capacity can be significantly magnified by connecting the LHe/LN$_2$ cryostat to a storage dewar (e.g. 100 l), thereby realizing the so-called *liquid-flow refrigeration* system [99, 204].

---

[9]In Europe, the nominal internal diameter is represented in mm with prefixing DN. The principal difference of KF and CF flanges are their gaskets: KF uses an elastomeric O - ring (e.g. rubber or Viton®), while CF uses soft metal gaskets (e.g. indium or OFHC®).

[10]Here, the LHe/LN$_2$ cooling cryostat capacity is the measure of a cooling cryostat's ability to remove heat.

5.3.3 Measuring cryostat

As outlined in Figure 5.12, the measuring cryostat consists of the (9) bulk HTS mounted on the (8) sTFMS, the (10) cryogenic force cell and (12) outer vacuum vessel. The measuring cryostat layout is defined by the sTFMS dimensions, since the given length of sTFMS lever is crucial for the force measurements (cf. Section 5.1.2). Further important considerations for the measuring cryostat are the thermal sizing (heat load), the mechanical sizing, the materials/components selection, manufacture compatible with the imposed restrictions (i.e. magnet bore $\varnothing = 300\,\text{mm}$), as well as vacuum and cryogenic issues.

Before presenting the main components of the measuring cryostat, the short note on heat transfer relevant at cryogenic temperatures and cryostat design is surveyed and will be used in later sections.

Heat transfer at cryogenic temperatures. The heat transfer relevant for the measuring cryostat include radiative heat, a conduction through gases/vacuum, and a solid conduction,

Radiative heat transfer. The radiative heat transfer is the major contribution to the cryostat heat load [99] and is calculated using an idealized formula [122]:

$$\dot{Q}_r \;=\; \frac{\varepsilon}{(N+1)}\sigma_{sb}A(T_{RT}^4 - T_{op}^4), \tag{5.6}$$

where σ_{sb} is the Stefan–Boltzmann constant, A is the surface area, T_{RT} and T_{op} are the RT and operating temperature, respectively, ε is a factor for the reflectivity and geometry of the material, and N is the number of intermediate surfaces between the RT and T_{op}.

In practice, a multilayer insulation (MLI)[11] is used realizing a full potential of Eq. 5.6, thereby providing effective radiation shielding [122]. In this case, the MLI manufacturer characterizes an MLI performance by a given heat flow density $\dot{q}_{MLI}$, which depends on the number of layers N, temperature, and the level of vacuum.

Conduction through gases/vacuum. There are two different regimes of heat conduction through gas which depend on pressure of the gas [99]. The first one is called hydrodynamic regime and is applied for the gas pressures near the atmosphere ($p \approx 1 \times 10^3\,\text{mbar}$). The hydrodynamic regime is utilized in the *solid-and-gas* conduction concept (cf. Section 5.2.2) providing contactless bulk HTS cooling via the

---

[11]Multilayer insulation is a stack of a reflective films consisting of a µm-thin vapor-depositing layer of aluminum separated by the insulating Mylar® or Kapton® interlayers [122].

exchange gas. The gas heat conduction in this regime is estimated as:

$$\dot{Q}_g = \frac{\overline{\lambda}A\Delta T}{d}, \tag{5.7}$$

where A is surface area of two plates where gas is enclosed, d is separation between plates, ΔT is temperature difference, whereas $\overline{\lambda}$ is the mean value of the temperature-dependent gas thermal conductivity.

Another regime is called free-molecular regime and is applied to the low pressure. In this regime, the gas heat conduction is independent of the gas heat conductivity and the separation between two surfaces [99], but depends on the gas species (for gaseous helium (GHe) $k = 2.1$), the vacuum level p, and the temperature difference ΔT. It is given as:

$$\dot{Q}_v = \frac{1}{2}kP\Delta T. \tag{5.8}$$

In the free-molecular regime, lowering gas pressure (achieving higher vacuum $p < 1 \times 10^{-3}$ mbar) in a cryostat results in a small $\dot{Q}_v$, providing better thermal isolation.

Finally, the heat transfer via *solid conduction* contributes mainly to the heat load of the supporting system (i.e. ring-and-six-rods and cryostat feedthrough). It can be expressed via Fourier's law:

$$\dot{Q}_c = \frac{A}{L}\int_{T_{RT}}^{T_{op}} \lambda(T)dT, \tag{5.9}$$

where A is a cross-section, L is the length, and $\int_{T_{RT}}^{T_{op}} \lambda(T)dT$ is the thermal conductivity integral with strong $\lambda(T)$ dependence over temperature $T_{RT} - T_{op}$.

Bulk HTS: final structure and mounting on sTFMS. A standard off-the-shelf Y-Ba-Cu-O bulk HTS with typical parameters as presented in Table 5.1 was selected for the final construction and is shown in Figure 5.14 a). Before mounting it on sTFMS, the bulk HTS was characterized via Hall mapping following the FC magnetization at 77 K. Figure 5.14 b) shows the distribution of the magnetic flux density scanned across the 30 mm × 30 mm pitch with the peak $B_T = 1.26$ T at 1 mm distance.

Then, the bulk HTS was machined accurately to the form of a cylindrical disc with a diameter of 48 mm and a thickness of 15 mm. Afterward, the bulk HTS was glued with a StycastATZ® epoxy into the 3-mm-thin-walled aluminum holder to position and reinforce the bulk HTS.

The final weight of the bulk HTS excluding the aluminum holder is 150.2 g. To
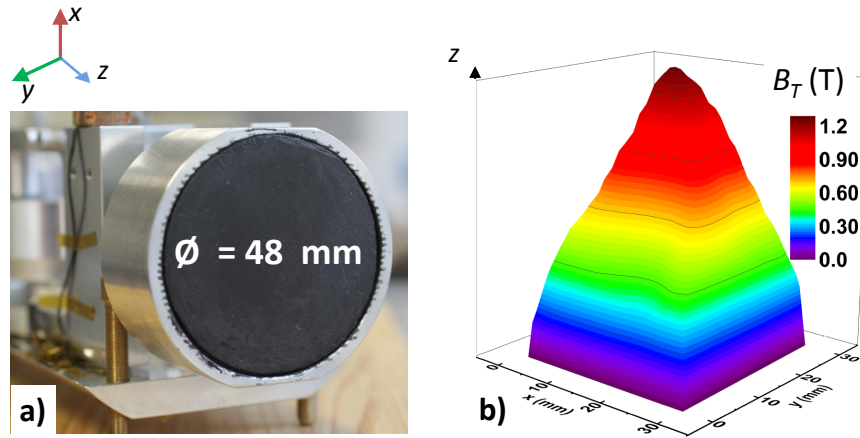
Figure 5.14: The Y-Ba-Cu-O bulk HTS used in the system: **a)** The bulk HTS with a diameter of 48 mm and a thickness of 15 mm is fixed in the aluminum holder using Stycast® epoxy. **b)** The distribution of the magnetic flux density with the peak trapped field of 1.26 T at 1 mm distance. Hall mapping is performed on the 30 mm × 30 mm pitch followed the FC magnetization at 77 K.

counterbalance this mass, the equivalent bronze cylinder[12] was glued into the aluminum holder with a StycastATZ® epoxy at the opposite site of the sTFMS lever.

Cryogenic force cell. The cryogenic force cell (CFC) was a realization of the closed single-walled vessel introduced for the *solid-plus-gas* conduction (see Section 5.2.2 and Figure 5.5). The *solid-and-gas* conduction was proposed to cool the bulk HTS (integrated with sTFMS) conforming the proper operation of the sTFMS. Furthermore, the *solid-and-gas* conduction concept performs several further functions, which are listed in Table 5.5.

Table 5.5: Required functions of the *solid-and-gas* conduction concept.

Number	Function
1)	housing and positioning bulk HTS and sTFMS
2)	contactless cooling the bulk HTS
3)	shortest thermal connection between the cooling and the measuring cryostats
4)	providing the exchange gas-tight (inside) and vacuum-tight (outside) environment
5)	access to the bulk HTS/sTFMS for their maintenance
6)	allowing for electrical feedthrough and an exchange gas supply

---

[12]The weight of bulk HTS is 150.2 g. In order to obtain the same mass of the counterweight from bronze ($\rho = 8.47\,\mathrm{g\,cm^{-3}}$), a cylinder with a diameter 45 mm and a height of 11 mm was used.

Figure 5.15 b) shows CFC, which consist of (1) cylindrical vessel, (2) DN100 CF blind flange, (3) copper gasket, (4) 15-pin-plug electrical feedthrough, (5) bolts, and (6) the exchange gas line. CFC has the inner diameter of 90 mm and the length of 280 mm resulting in a CFC's surface area to be about of $0.1\,m^2$, which was the crucial for the radiative heat load. The radial wall thickness is 6 mm, while the wall thickness in front of the bulk HTS is only 2 mm. The 2-mm-thin front wall was a compromise to provide sufficient mechanical strength of the aluminum vessel under pressure, manufacturability of aluminum, and the need to minimize the distance from the bulk HTS surface to the Super-LOFOS warm wall surface (see insert of Figure 5.16).
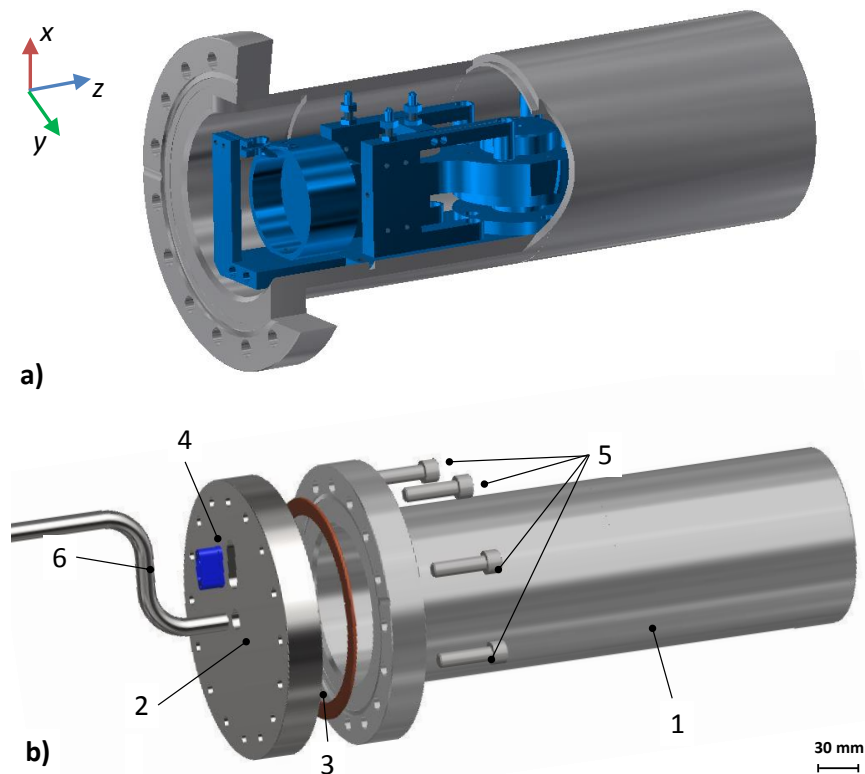
Figure 5.15: CAD models of the cryogenic force cell (CFC): **a)** illustrates the housing of the sTFMS within CFC; **b)** shows its components: (1) cylindrical vessel, (2) CF blind flange, (3) copper gasket, (4) electrical feedthrough, (5) bolts and (6) exchange gas supply line.

The selection of the material and components depended on multiple factors:

1) low magnetic susceptibility to operate in a high magnetic field,

2) vacuum sealing in a cryogenic environment,

3) machinability, manufacturability or commercial availability to remain flexible when combined with other components of Super-LOFOS,

4) degassing, permeation and thermal conductivity of the exchange gas with the regard to other component material.

The CFC was machined of aluminum alloy (AluVac®, Vacom, Jena [222]), has the form of a closed vessel from the one side (where the bulk HTS is located) and ends with the DN100 CF flange from the opposite side[13]. It is sealed with a mating (2) CF blind flange via (3) the copper gasket.

The ConFlat® utilization in the CFC was an important decision to satisfy all functions (cf. Table 5.5) of the *solid-and gas* concept. Alternatively, a standard Swagelock® system is also suitable for the cryogenic sealing, but it requires more space, especially along the *z*-axis, which is in contrast with a need to minimize the thermal contact between the cooling and measuring cryostats.

The (2) CF blind flange was made of AISI 316 stainless steel and includes (4) electrical feedthrough and (6) exchange gas line. The commercial electrical feedthrough and customized exchange gas line were manufactured also from AISI 316 stainless steel and, therefore, were welded[14] with the (2) CF blind flange. The vacuum compatible welding and cryogenic environment were arguments for the off-the-shelf (2) CF blind flange made from a steel, rather than an aluminum, although a customized CF blind flange made of aluminum would provide better thermal coupling between the cooling cryostat and the measuring cryostat.

The last concern was the choice of the exchange gas and condition to manage it. Among cryogenic gases, a gaseous helium (GHe) has the lowest condensation temperature and highest thermal conductivity ($\overline{\lambda_{He}} = 0.5\,\mathrm{W\,m^{-1}\,K}$) in the hydrodynamic regime (cf. Eq. 5.7), which makes it suitable for the *solid-and-gas* concept in the temperature range of interest. This, in turn, required the CFC to be helium-tight (inside) and vacuum-tight (outside) as well as to maintain the GHe at the atmosphere $p \approx 1 \times 10^3\,\mathrm{mbar}$.

---

[13]The DN100 CF flange is an optimal size to fit the Super-LOFOS.
[14]The tungsten-inert-gas (TIG) welding of the AISI 316 stainless steel ensures the vacuum-tight joint.

Vacuum vessel and mechanical support. Similar to the CFC, the design of the
vacuum vessel followed multiple trade-offs and resulted in a circular structure shown
in Figure 5.16. It consists of the (1) DN200 CF flange to mate with the cooling cryostat,
(2) DN200 tube (with length of 324 mm and thickness of 5 mm) and (3) a lid plate. All
parts were made of the AISI 316 stainless steel and are joined using tungsten-inert-
gas (TIG) welding. The (4) ring-and-six-rods was used to concentrically align and
mechanically fix the CFC within the vacuum vessel. Another function of the ring-and-
six-rods was to reduce the conduction heat leak (cf. Eq. 5.9), therefore the ring-and-
six-rods (cf. Figure 5.16) was made of G10-CR fiberglass with the thin diameter of the
rods and has an inherent low thermal conductivity of about 0.2-0.4 $\mathrm{W\,m^{-1}\,K^{-1}}$ in the
temperature range 40-100 K [99].

The vacuum vessel was vacuum-tightly connected with the measuring cryostat via
the CF DN200 flange and was sealed with the Cu-gasket. This configuration ensured
an access to CFC and allowed it to be flexible to adopt an alternative cooling solution
in the future (e.g. closed-cycle refrigerator systems).
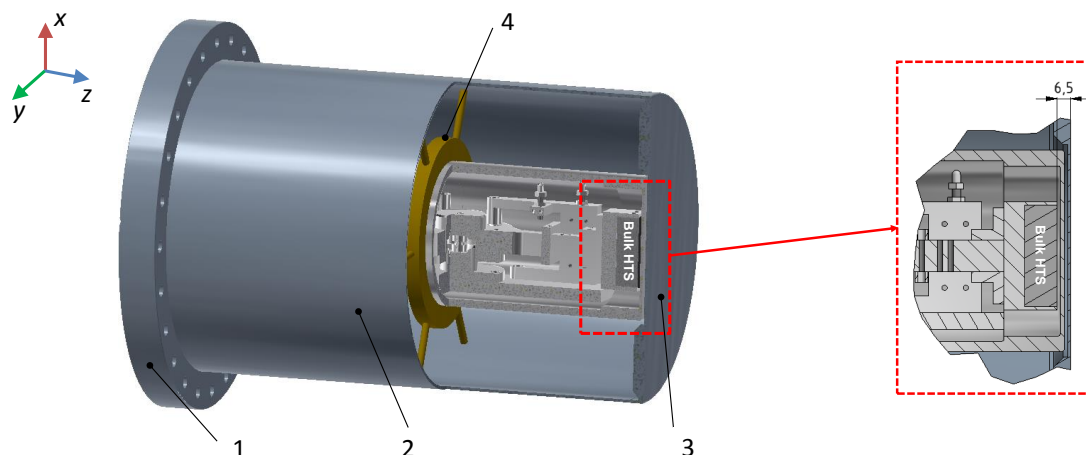
Figure 5.16: The outer vacuum vessel is composed of (1) CF flange, (2) tube and (3) lid plate.
            To mechanically fix the vacuum vessel on the CFC one uses the (4) ring-and-
            six-rods, which is made of G10-CR fiberglass. *Cutout*: drawing presentation of
            the area near the bulk HTS to demonstrate the isolation gap between the bulk
            HTS and the outer front Super-LOFOS surface.

As mentioned in Section 2.2.2 and also in the proof-of-principle experiment (cf. Chap-
ter 4) it was vital to minimize the distance between the bulk HTS surface and the
cryostat outer warm wall. In the case of the Super-LOFOS, this distance includes
GHe/vacuum gaps and lid thickness of the two vessels, namely CFC and outer vac-
uum vessel. On the one hand, the thickness of vessels must be enough to withstand

the pressure load and allow for welding and machining. On the other hand, the vacuum gap must be large enough to provide the thermal isolation. Taking all of these factors into account resulted in the distance of 6.5 mm, as delineated in the cutout of Figure 5.16.

Thermal insulation. A primary vacuum vessel function was to thermally insulate the CFC, minimizing the heat transfer (cf. Section 5.3.3) between the RT and desired cryogenic T_{op}. Therefore, the vacuum vessel used the advantage of the free-molecular regime (cf. Eq 5.8) enabling the pressure level of $p = 1 \times 10^{-5}$ mbar to reduce the gas heat transfer.

To reduce the radiative heat transfer, the 10-layer MLI (RUAG®, Coolant 2) was wrapped around the CFC. According to manufacture specifications [223], the MLI heat flow density of $\dot{q}_{MLI} = 1\,\mathrm{W\,m^{-2}}$ is given under condition of $p = 1 \times 10^{-5}$ mbar and temperatures ranging from 300 K to 77 K.

The thermal insulation of the measuring cryostat was estimated using a one dimensional and stationary methodology described in [99, 224, 225]. The solid conduction heat load of the bulk HTS and sTFMS as well as ring-and-six-rods were neglected.

Figure 5.17 shows the simplified thermal schematic of the measuring cryostat, which includes the CFC and the vacuum vessel. The temperature at the vacuum vessel outer wall is $T_{RT} = 300\,\mathrm{K}$. The temperature at the interface between the cooling and measuring cryostat is constant and corresponds to the boiling points of LN$_2$ and LHe (cf. Table 2.3), whereas the operating temperatures are $T_{op} = 50\,\mathrm{K}$ and $T_{op} = 80\,\mathrm{K}$ according to the requirements (cf. Table 5.4).
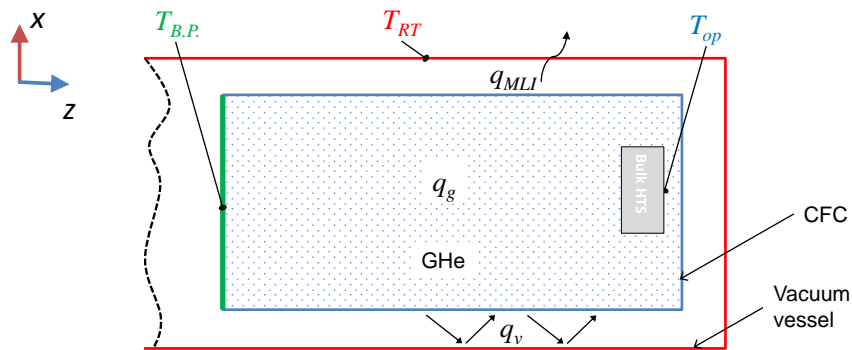
Figure 5.17: A thermal insulation schematic of the measuring cryostat.

Table 5.6 tabulates the calculated thermal insulation input for the stationary case, when the measuring cryostat is cooled down to the operation temperature. Among

vacuum isolation $\dot{Q}_v$ and gaseous helium thermal (or more correctly cold) transfer from the cooling cryostat to the bulk HTS along z-axis $\dot{Q}_g$, the radiation heat transfer $\dot{Q}_{MLI}$ degrades the thermal insulation the most. Table 5.6 also shows the amount of the required coolant (e.g. LN$_2$ and LHe)[15] to sustain the measuring cryostat in the stationary state for two hours.

Table 5.6: The thermal insulation of the measuring cryostat.

	LN$_2$	LHe
Radiation, $\dot{Q}_{MLI}$(W)	1.50×10^{-1}	1.00×10^{-1}
Vacuum, $\dot{Q}_v$(W)	6.60×10^{-3}	7.50×10^{-3}
Gas conduction, $\dot{Q}_g$(W)	4.36×10^{-3}	6.66×10^{-3}
Sum, $\dot{Q}$(W)	1.61×10^{-1}	1.64×10^{-1}
Required coolant amount, (l)	0.01	0.45

Cryogenic liquid consumption during cool-down. The stationary state is reached when the CFC containing bulk HTS/sTFMS within the measuring cryostat is already cooled down to the operating temperature. To determine how much cryogenic liquid is required to refrigerate the CFC with the bulk HTS and sTFMS, the Debye model approach described by Ekin [99] was used. This approach allows us to estimate the molar energy change ΔU upon refrigeration using the Debye relation of the volume specific heat C_V:

$$\frac{\Delta U}{T} \;=\; \frac{(U_{RT} - U_{op})}{T} \;=\; \frac{1}{T} \int_{T_{op}}^{T_{RT}} C_V dT. \tag{5.10}$$

Tabulated data represented by Eq. 5.10 is available from [99] and can be applied to calculate the amount of LN$_2$ or LHe that will be consumed to cool down a material with the mass m from the T_{RT} to T_{op}. In our case, the CFC with bulk HTS/sTFMS is made mainly of aluminum[16] and weighs 3 kg.

Table 5.7 presents the molar energy change, total energy, and required LN$_2$ or LHe amount necessary to refrigerate the CFC with bulk HTS/sTFMS to a corresponding operation temperature.

In practice, to reduce LHe consumption and to speed up the cool-down process, LN$_2$ precooling is commonly used, since LN$_2$ has almost sixty times the amount of latent

---

[15]Calculation is made based on the Latent heat of vaporization values (see Table 2.3).
[16]The aluminum molar mass $M = 26.98$ [99].

Table 5.7: Estimation of required cryogen amount necessary to refrigerate the CFC with bulk HTS/sTFMS to a corresponding operation temperature.

	300 K to 77 K	77 K to 50 K
Molar energy change $U_{RT} - U_{op}$ (kJ mol^{-1})	4.30	4.47
Total energy (kJ)	478.2	497.1
Required LN$_2$ (l)	3	
Required LHe (l)	185	8

vaporization heat as compared to LHe (cf. Table 2.3). In the case of CFC with bulk HTS/sTFMS refrigeration, precooling from 300 K to 77 K consumes 3 l of LN$_2$, instead of 185 l of LHe, and 8 l of LHe is required to continue cooling from 77 K to 50 K.

Besides the CFC with bulk HTS/sTFMS, Super-LOFOS contains more components (e.g. inner vessel of cooling cryostat, support system, etc.) which increase the mass and integrated specific heat to be cooled down. This requires more cooling capacity and consequently cryogenic liquid amounts. The concern of the Super-LOFOS cool-down time and consumed cryogenic liquids will be investigated experimentally in the next Section 5.4 as well as in implementation experiments (cf. Section 6).

5.3.4 Measurement instrumentation

The cooling cryostat was equipped with a 16-pin-plug feedthrough. This allows us to thread out fifteen wires through Super-LOFOS and provide electrical service for the sTFMS and install temperature sensors.

The sTFMS requires five lead wires for supplying the positioning sensor, where two wires are used for the excitation current I_{ex} and three lead wires for measuring the ΔV_{ph}. The rest of the wires serve for two temperature sensors, using four-point-probe connection. Figure 5.18 a) illustrates the position of temperature sensors in the Super-LOFOS: the Cernox® (CX-1070) sensor is mounted at the aluminum thermal link, which is located between cooling and measuring cryostat. The Pt-1000® sensor is mounted at the sTFMS platform in the vicinity of the bulk HTS.
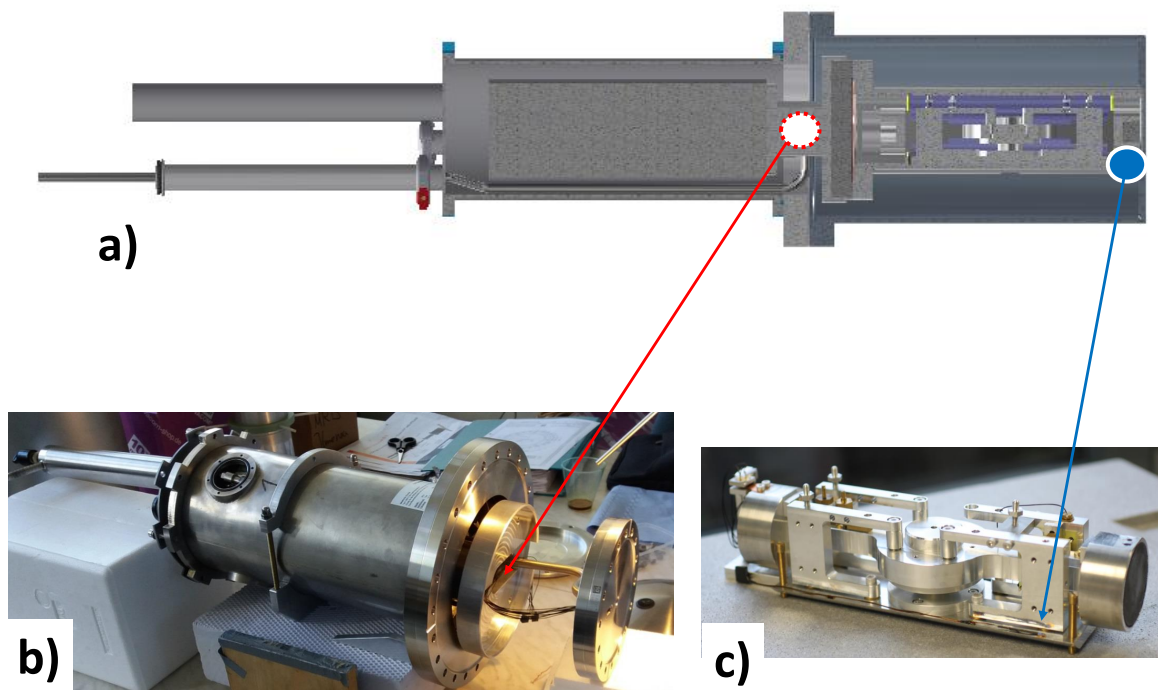
Figure 5.18: **a)** The location of temperature sensors in the Super-LOFOS. **b)** the Cernox® (CX-1070) sensor is mounted at the aluminum thermal link, which is located between cooling and measuring cryostat. **c)** the Pt-1000® sensor is mounted at the sTFMS platform in the vicinity of the bulk HTS.

In order to provide convenient and flexible system assembly, plug-and-socket terminals were also installed.

5.4 Initial assembly

The manufacturing of components was distributed between several companies depending on the required competencies and schedule considerations. However, the initial assembly of the Super-LOFOS took place at ATZ®, Torgau [86] and was dedicated to the validation of the system integrity and testing of the vacuum and cooling performance. Note, during the initial assembly bulk HTS/sTFMS were excluded from the system. Referring to Figure 5.12 the assembly sequence was to:

a) fasten the (3) flange adapter to the front flange of the (1) cooling cryostat,

b) install temperature sensors and wiring,

c) fasten the (4) thermal link to the cooling interface of the (1) cooling cryostat,

d) thread the He-line with the (7) blind flange through the (1) cooling cryostat,

e) fasten the (7) blind flange with the (10) CFC,

f) evacuate the (10) CFC and perform its leak test,

g) put the (11) ring-and-six-rods mechanical support on the (10) CFC,

h) wrap the (10) CFC and (4) thermal link with multilayer isolation foils,

i) put on the outer (12) vacuum vessel and tighten it with the (3) adapting vacuum flange,

j) perform leak test of the entire system,

k) perform a cooling test.

The initial assembly revealed some violations in manufacturing and tolerance issues of several components (e.g. aluminum thermal link, outer vacuum vessel, ring-and-six-rods mechanical support) and required re-work and subsequent machining. When those issues were fixed, Super-LOFOS passed the leak test with results documented in Table 5.8.

The cooling test comprised LN$_2$ refrigeration of the Super-LOFOS cooling cryostat. Thus, LN$_2$ was periodically poured manually into vertically standing Super-LOFOS, as illustrated in Figure 5.19 insert. Furthermore, Figure 5.19 shows the temperature T and cooling speed $\frac{dT}{dt} = 0$ as a function of time t, where temperature T was monitored at the (4) aluminum thermal link at the cooling cryostat bottom (cf. Figure 5.12). It

Table 5.8: Results of the leak test of the Super-LOFOS after the initial assembly at ATZ®, Torgau.

	Cryogenic Force Cell	Vacuum isolation
Pressure	$5 \times 10^{-5}\,\mathrm{mbar}$	$4 \times 10^{-5}\,\mathrm{mbar}$
Pumping time	$2\,\mathrm{h}$	$12\,\mathrm{h}$
Leak rate	$1 \times 10^{-10}\,\mathrm{mbar\,l\,s^{-1}}$	$1 \times 10^{-9}\,\mathrm{mbar\,l\,s^{-1}}$

took about $3\,\mathrm{h}$ to reach $93\,\mathrm{K}$ and stationary state ($\frac{dT}{dt} = 0$). Most of the cool-down time was needed to achieve $T \approx 100\,\mathrm{K}$, because the integrated specific heat of the Super-LOFOS cooling cryostat decreases slowly with temperature.
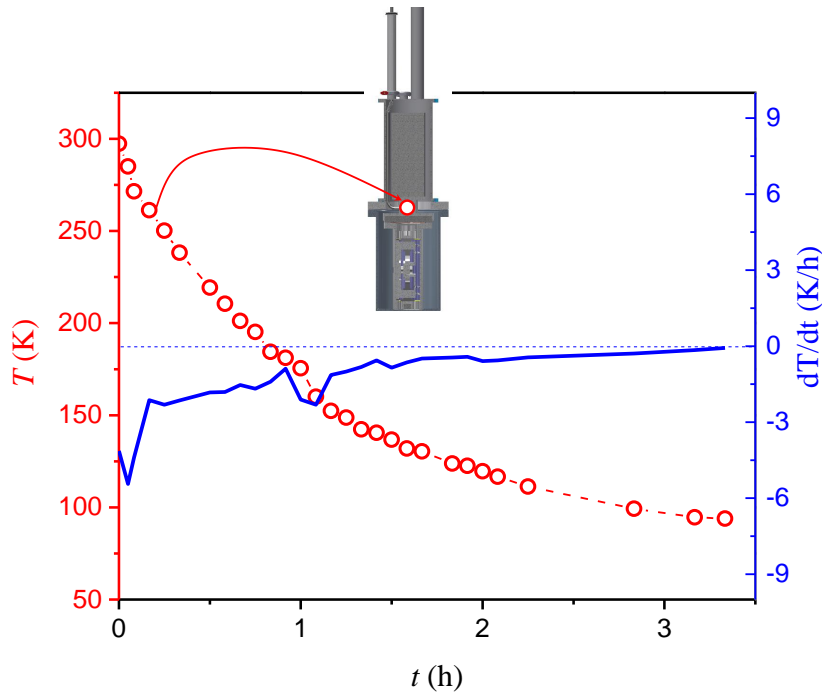
Figure 5.19: First Super-LOFOS cooling with $\mathrm{LN_2}$ during the initial assembly at ATZ®, Torgau.

6 Implementation of Super-LOFOS

6.1 Experimental

After the initial assembly, Super-LOFOS was disassembled and transported to Technische Universität Ilmenau for the final validation. Super-LOFOS was re-assembled to include its key sub-systems - the bulk HTS and sTFMS. In order to validate Super-LOFOS, several experiments were designed, each of which following the steps summarized Table 6.1:

Table 6.1: The experimental sequence for the validation of Super-LOFOS.

Number	Steps
(0)	assembling and preparatory work
(1)	pre-cooling
(2)	magnetization
(3)	LFV measurements

Assembling and preparatory work. After the sTFMS was calibrated and adjusted at the RT by Na Yan, the process of Super-LOFOS re-assembling was augmented to include placing the bulk HTS/sTFMS into the CFC and anchoring the sTFMS with screws to ensure it is properly fixed (see Figure 5.8). The CFC is then sealed with the CF blind flange, evacuated, and flushed several times with GHe. As a result, the CFC remains filled with the GHe under the normal atmosphere ($p \approx 1 \times 10^3$ mbar). The last assembly step is to dock the cooling cryostat on to the outer vacuum vessel and evacuate the outer vessel to $p = 1 \times 10^{-4}$ mbar or lower in order to ensure good thermal isolation.

Magnetization. As stressed in Section 5.2.3, the 5TCFM is deployed for the bulk HTS magnetization, during which Super-LOFOS is brought to the *magnetization mode* (sTFMS is inverted on 180°) and inserted into the magnet bore. Figure 6.1 a) shows the position of Super-LOFOS during magnetization. Note, Super-LOFOS is placed

eccentric ($\Delta x = 42\,\text{mm}$) in the magnet bore, since it is mounted on the optical slab of the transport table (see Figure 6.1 b).
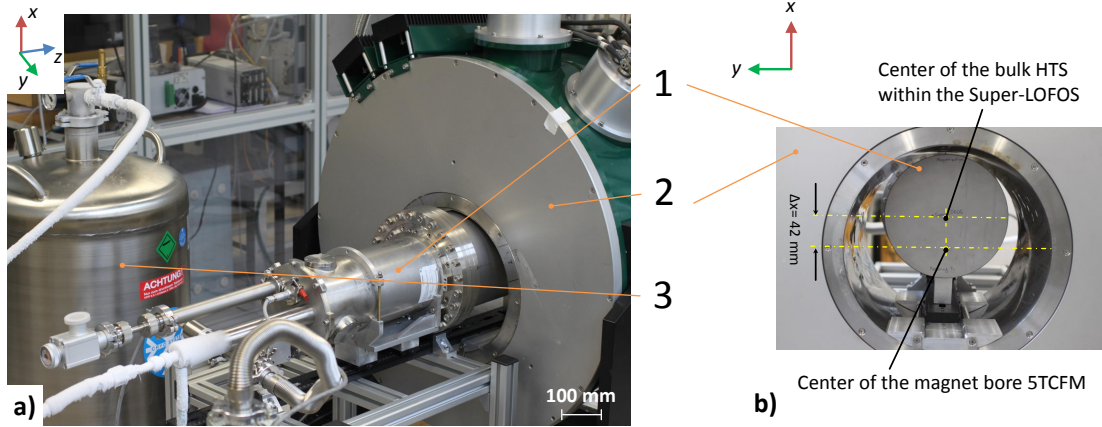
Figure 6.1: **a)** Magnetization set-up of (1) Super-LOFOS in the (2) magnet bore of the 5TCFM with the continuous liquid-flow cooling using (3) shipping dewar (with LN_2 or LHe). **b)** Eccentric positioning of Super-LOFOS in the magnet bore.

The magnetization can follow the FC or ZFC procedures with the ascent and descent ramp rate $\dot{B} = 0.092\,\text{T}\,\text{min}^{-1}$. The refrigeration can be done using LN_2 or LHe. However, in the case of LHe, the equipment is pre-cooled with LN_2. After reaching corresponding temperatures, LN_2 is purged with the GHe and the last bit of cooling is performed with LHe. The LN_2 pre-cooling accelerates the process, since LN_2 has almost sixty times the amount of latent vaporization heat as compared to LHe (cf. Table 2.3). It also reduces LHe consumption and subsequent costs.

LFV measurements. If the bulk HTS is magnetized, then the Super-LOFOS is turned around the z-axis, whereby sTFMS is brought to the *measuring mode* followed by the precise alignment in the horizontal plane (y-z plane).

Afterward, Super-LOFOS is arranged for the LFV measurements using the dry calibration setup, which is shown in Figure 6.2. In contrast to the previous case (cf. Chapter 4), the dry calibration setup accommodates force measurements in a horizontal direction because of typical industrial demand [16]. The dry calibration setup consists of (1) Super-LOFOS, an (2) aluminum rod (used in previous dry-calibration)[1], (3) linear drive, and a (4) transport table.

The (2) aluminum rod is attached to the (3) linear drive, which enables a repetitive motion with a prescribed constant velocity. One LFV measurement includes the motion

---

[1]The aluminum rod with an electrical conductivity $\sigma_{Al} = 19.43\,\text{MS}\,\text{m}^{-1}$ has a length of $1000\,\text{mm}$ and a diameter of $40\,\text{mm}$ [3].
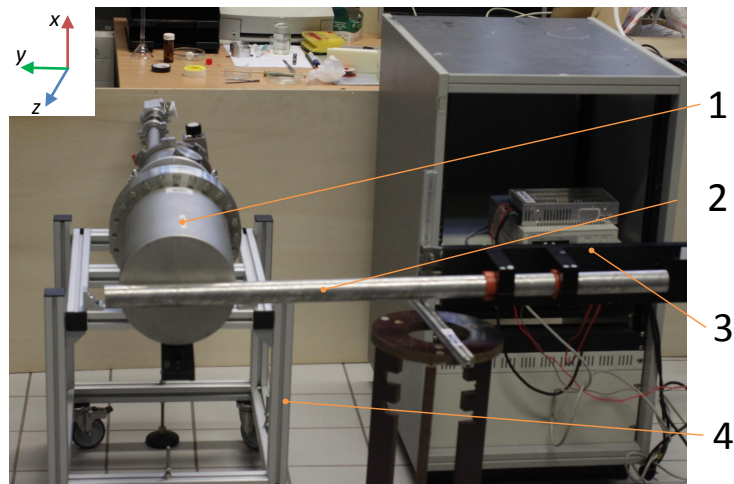
Figure 6.2: The experimental setup for the validation of Super-LOFOS. It includes (1) Super-LOFOS, (2) aluminum rod, (3) linear drive, and (4) support table.

of the (2) aluminum rod during $t = 40\,\mathrm{s}$ with a given delay of $t = 30\,\mathrm{s}$ before and after the start of the motion. The velocity in this experiment is limited by $3.3\,\mathrm{mm\,s^{-1}}$ due to the construction properties of the linear drive [22]. Thus, velocities are approximately one order of magnitude lower as compared to the prior proof-of-principle experiment (cf. Chapter 4), but it is sufficient to measure the force in the range of interest.

6.2 Results and discussion

Results of LFV measurements using Super-LOFOS are presented in chronological order below.

6.2.1 Experiment-1: Cooling with LN$_2$

Motivation.   The *experiment-1* was designed to give a first run and validate the working principle of Super-LOFOS. Apart, it was crucial to:

1) train personnel how to safely handle the system,

2) verify the *solid-plus-gas* cooling,

3) magnetize the bulk HTS,

4) provide means of improvement for the future implementation with LHe cooling.

Cooling.   After the Super-LOFOS was assembled, CFC was filled with the GHe and maintained at normal atmosphere ($p \approx 1 \times 10^3$ mbar). Preceding the LN$_2$ liquid-flow cooling, the Super-LOFOS was evacuated to the $p = 1.4 \times 10^{-4}$ mbar. Figure 6.1 shows a storage dewar with LN$_2$, which was connected to the Super-LOFOS, thereby providing the continuous cooling with the LN$_2$ flow regulation[2]. Figure 6.3 a) shows temperature as a function of time and indicates the experimental steps, while Figure 6.3 b) delineates the Super-LOFOS horizontal arrangement and position of sensors.

It took about 15.5 h to reach temperatures below T_c. Such a long cool-down time is attributed to the large cumulative Super-LOFOS specific heat and degraded vacuum.

Magnetization.   ZFC magnetization with $B_A = 2$ T was applied due to the continuous need of cooling to the desired $T_{op} < T_c$. When the B_A was reduced to zero, operating temperature reached $T_{op} = 88.8$ K and the maximum trapped field $^z B_T = 20$ mT was recorded. This trapped field $^z B_T$ was measured at the front surface of Super-LOFOS using a three-axis Hall probe (Magnet-Physik®, FH 36) and is 6.5 mm distant from the bulk HTS's surface (cf. Figure 5.16). Obtained $^z B_T$ reduced to $^z B_T = 15$ mT at about one hour and is shown in the cutout of Figure 6.3 together with $T_{op}(t)$.
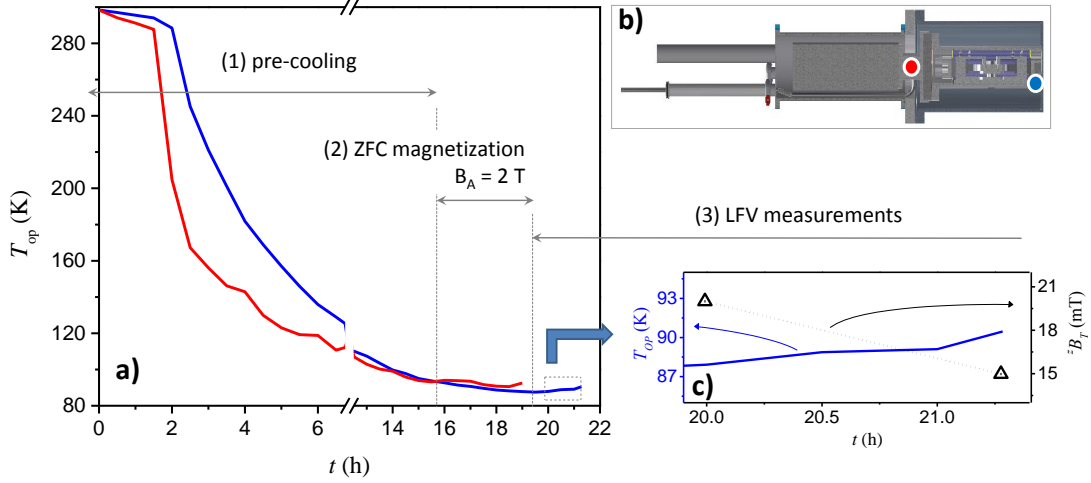
Figure 6.3: **a)** The LN$_2$ liquid-flow cooling, followed by the ZFC magnetization with B_A = 2 T. **b)** The location of temperature sensors in the Super-LOFOS. **c)** The cutout enlarges time-dependent temperature behavior and indicates the measured trapped field B_T, when the B_A was reduced to zero.

LFV measurements. Super-LOFOS was disconnected from the LN$_2$ continuous liquid-flow cooling and brought to the *measuring mode*. Furthermore, it was placed at 18 mm distance from the aluminum rod surface. It was necessary to ensure that resultant Lorentz forces F_L remain within the measuring range of sTFMS. Afterward, Super-LOFOS was adjusted to perfectly align sTFMS in the horizontal plane (y-z plane).

LFV measurements were performed for two given velocities $u_1 = 3.2\,\text{mm}\,\text{s}^{-1}$ and $u_2 = 1.55\,\text{mm}\,\text{s}^{-1}$, as displayed in Figure 6.4 a). Unfortunately, further LFV measurements were not possible because of obtained ^zB_T vanished (T_{op}>T_c). Thus, it is important to preserve the continuous liquid-flow cooling during LFV measurements.

Figure 6.4 b) shows the obtained output voltage $\Delta V_{ph}(t)$ of the positioning sensor, which exhibits a stepwise signal for both velocities. In the case of $u_1 = 3.2\,\text{mm}\,\text{s}^{-1}$, $\Delta V_{ph}(u_1)$ diminished down to zero when the aluminum rod stopped. However, in the case of $u_2 = 1.55\,\text{mm}\,\text{s}^{-1}$, $\Delta V_{ph}(u_2)$ is almost equal to $\Delta V_{ph}(u_2)$ and it does not shift back to the zero.

In principle, the expected $\Delta V_{ph}(u_2)$ should be about two times lower than $\Delta V_{ph}(u_1)$ since given velocities differ by almost a factor of two. Such a scenario was simulated using the developed model (cf. Section 4.3), which was adopted to the rel-

---

[2]To control the LN$_2$ flow the pressure in the storage dewar is manually regulated using a pressurized valve in a range between 0.5 bar to 1 bar.
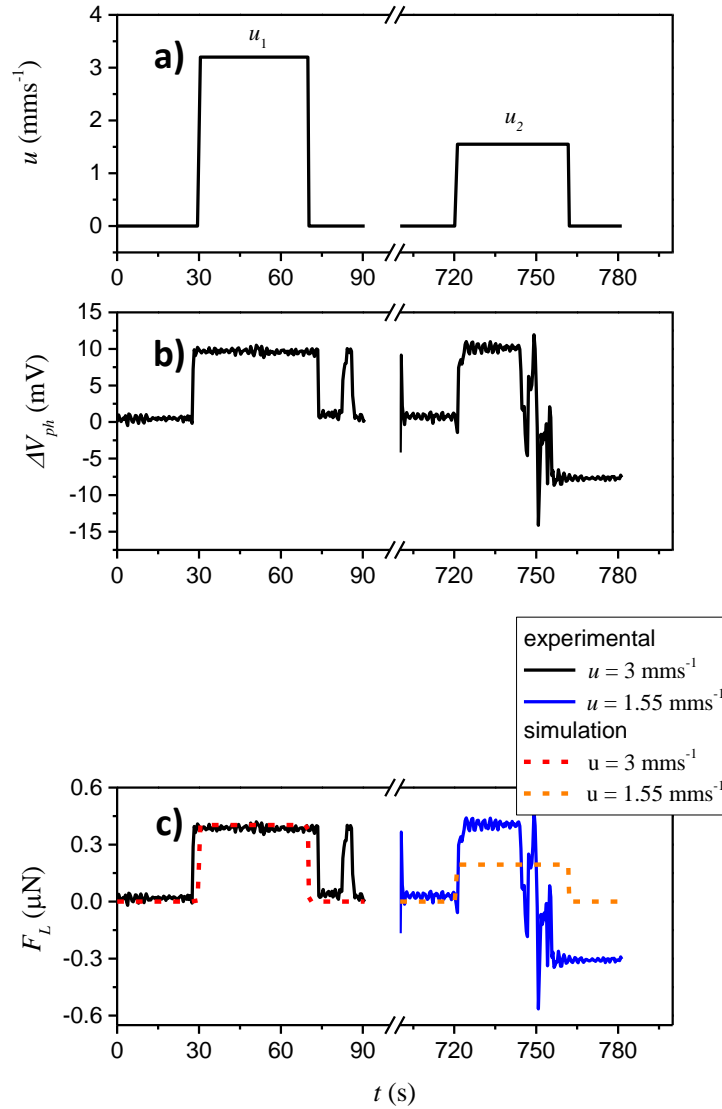
Figure 6.4: LFV measurement results: **a)** given velocities $u_1 = 3.2\,\text{mm}\,\text{s}^{-1}$ and $u_2 = 1.55\,\text{mm}\,\text{s}^{-1}$. **b)** Obtained output voltage $\Delta V_{ph}(t)$ of the positioning sensor. **c)** Lorentz force F_L as function of time: solid lines indicate the experimental results and dashed lines indicate the simulation results.

evant LFV experimental setup with the Super-LOFOS. The value of bulk HTS's $j_c = 4.33 \times 10^6\,\text{A}\,\text{m}^{-2}$ was determined from the experimentally obtained $^z B_T = 20\,\text{mT}$ using Eq. 4.3 and Eq. 4.4. The simulated $F_L(u)$ are compared with the experimental data in Figure 6.4 c). In the case of u_1, $F_L(u_1)$ obtained experimentally is consistent with the simulated result. However, in the case of u_2, experimental $F_L(u_2)$ quantitatively deviates from the simulation result. This rather contradictory result is likely to be related to mechanical or electrical disturbance of the sTFMS and can be revealed

only after warming and disassembly the Super-LOFOS.

When Super-LOFOS was warmed up to RT, the sTFMS was inspected, revealing no deviance and no defects. Following, sTFMS was newly calibrated and prepared for the next LFV measurements using LHe to achieve a lower temperature and thus a larger trapped magnetic flux density.

6.2.2 Experiment-2: Cooling with LHe

Experiment-2 was designed to let the bulk HTS trap a stronger B_T using LHe cooling. This required to exploit a modified dry calibration setup with a model electrolyte[3] of $\sigma = 20\,\mathrm{S\,m^{-1}}$ instead of the aluminum rod.
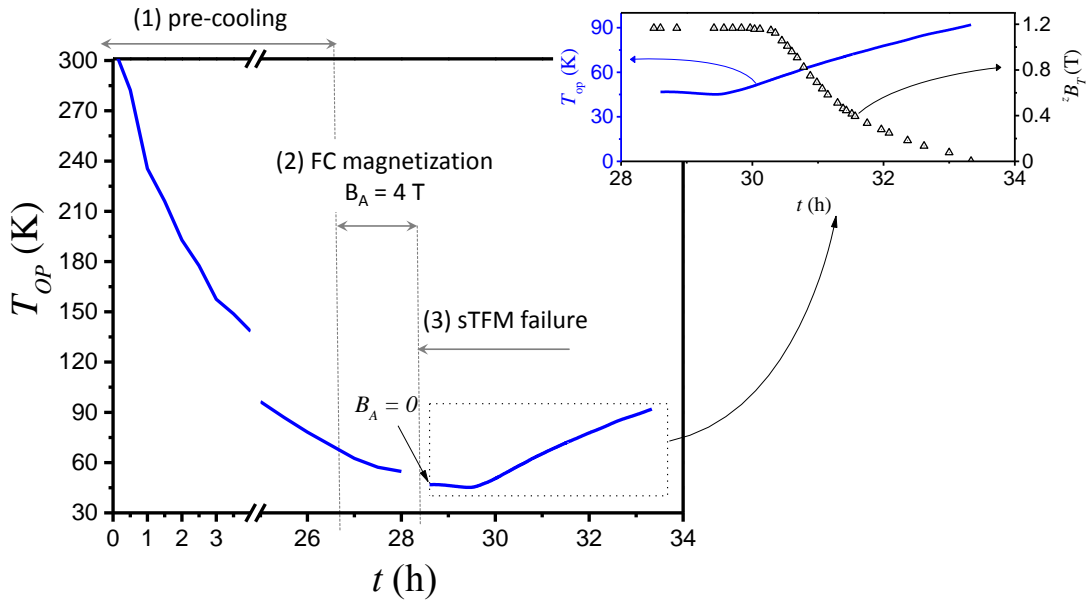
Figure 6.5: LHe liquid-flow cooling, followed by the FC magnetization with $B_A = 4\,\mathrm{T}$ and an attempt of LFV measurements, which failed due to sTFMS failure. *Cutout* enlarges time-dependent temperature behavior and indicates the measured trapped field ^zB_T, when the B_A was reduced to zero.

Pre-cooling and magnetization. The Super-LOFOS was evacuated to the $p = 1.1 \times 10^{-4}\,\mathrm{mbar}$[4] followed by LN$_2$ pre-cooling. As in the previous case, CFC was filled with the GHe and maintained at normal atmosphere ($p \approx 1 \times 10^3\,\mathrm{mbar}$).

---

[3]Plexiglas® vessel with fully filled saline water is used to model the electrolyte. The vessel has a cylindrical form with a length of 1000 mm, an outer diameter of 50 mm and a wall thickness of 2 mm.

[4]Achieved vacuum reduced to $p = 1.0 \times 10^{-5}\,\mathrm{mbar}$ before magnetization due to cryo-pumping.

Figure 6.5 shows a time-dependent temperature $T_{op}(t)$ monitored during the experiment. At first, Super-LOFOS was pre-cooled using LN$_2$ down to to the $T_{op} < T_c$. Afterward, LN$_2$ dewar was replaced with LHe shipping dewar and Super-LOFOS was further cooled using LHe continuous liquid-flow refrigeration[5]. In order to sustain better thermal vacuum insulation, the Super-LOFOS was evacuated continuously during entire cooling maintaining the pressure of $p = 1.0 \times 10^{-5}$ mbar. Relatively long cooldown time of about 26 h was deliberately performed setting slow rate of continuous liquid-flow refrigeration.

The magnetization followed FC process involving the application of $B_A = 4$ T and subsequent cooling to T_{op}. When $B_A = 0$ T, operating temperature reached $T_{op} \approx 46$ K and the trapped field of $^z B_T = 1.2$ T at the front surface of Super-LOFOS was documented. By regulating the LHe mass flow, the temperature at the bulk HTS was maintained below the reached value of $T_{op} \approx 46$ K. This enabled the trapped field to persist. The cutout of Figure 6.5 plots $T_{op}(t)$ superimposed with $^z B_T(t)$ when $B_A = 0$ T, showing the nearly constant trapped field $^z B_T = 1.2$ T over two hours.

LFV measurements and sTFMS failure. The sTFMS adjustment failed when the Super-LOFOS was arranged for the modified dry calibration setup. The signal of the positioning sensor yielded a constant ΔV_{ph}, which was sensitive only to the manual disturbances (see Figure 6.6 a). This observation suggested that the sTFMS operation is disturbed. In particular, it was suspected that the rotation movement of the lever with the respect to the flexure bearing is blocked.

Repeated attempts to release the blockage of sTFMS by rotating and inclining the Super-LOFOS brought no success. Moreover, it was verified that neither the acquisition program nor the electrical contact/connections were the problem.

Failure investigation. To understand what caused the sTFMS failure (blocked rotation), Super-LOFOS was warmed up and opened for sTFMS inspection. Upon opening the CFC, two deviances were discovered and are shown in Figure 6.6 b)-c):

1) tangled wires hampered the electrical connections between the sTFMS and the cooling cryostat, despite careful fixation and alignment with the Capton® band during assembly,

2) a bent movable aperture of the positioning sensor.

---

[5]Similar to the LN$_2$, the LHe flow was manually regulated using a pressurized valve.
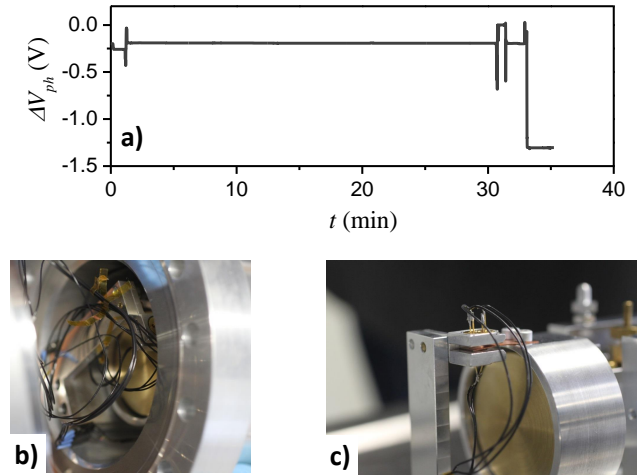
Figure 6.6: **a)** Output signal ΔV_{ph} of positioning sensor during LFV measurements. Observed deviance after disassembly of the Super-LOFOS: **b)** electrical connection between the sTFMS and the cooling cryostat, **c)** the bent movable aperture of the positioning sensor.

The tangled wires can partially limit the sTFMS rotation, rather than block it completely. Therefore, the bent movable aperture was identified as the root cause for blockage. This interpretation was proved in the subsequent test at RT after aligning the movable aperture to its original shape. As result, sTFMS operation was restored: The lever rotates freely, yielding the oscillating ΔV_{ph} signal (see Figure 6.7).
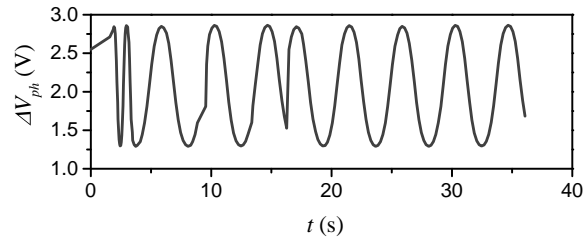
Figure 6.7: A periodical ΔV_{ph} signal of sTFMS, which was achieved after the movable aperture was aligned to its original shape.

The most probable reasons for the bent aperture were identified as follows:

1) routinely tilting and inclining the Super-LOFOS when rotating (around the z-axis) during assembly as well as before and after magnetization,

2) magnetic forces that emerge during magnetization (cf. Section 5.2.3) due to eccentric positioning of the bulk HTS in the magnet bore (see Figure 6.1 b).

Corrective actions and repeated LFV measurements.   A number of corrections and improvements of Super-LOFOS and its components were performed:

1) *Wiring:* (1) wires between the sTFMS and the cooling cryostat were shortened, better aligned, and fixed (see Figure 6.8 a),

2) *Controlled rotation:* a (2) security clamp and (3) rotation bearings were added at Super-LOFOS to provide smooth rotation around the z-axis and are shown in Figure 6.8 a),

3) *Concentric insertion:* the way in which Super-LOFOS is mounted to the optical slab was reworked in order to minimize the eccentric positioning. (see Figure 6.8 b).
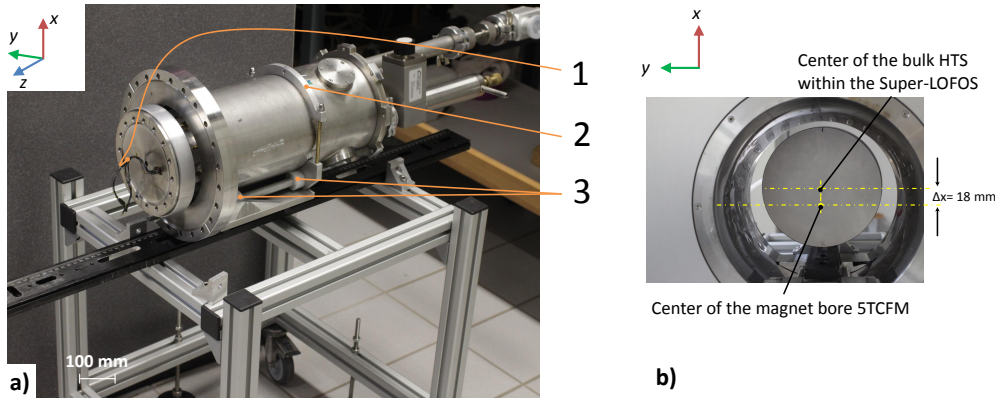
Figure 6.8: Visualization of the realized improvements. **a)** *Wiring:* (1) wires between the sTFMS and the cooling cryostat were shortened and better aligned. *Controlled rotation:* the rotation of Super-LOFOS was improved by adding (2) the security clamp and (3) four rotation bearings. Such a configuration minimizes undesired inclinations and provides smooth rotation of Super-LOFOS around the z-axis. **b)** the way in which Super-LOFOS is mounted to the optical slab was reworked in order to minimize the eccentric positioning from $42\,\mathrm{mm}$ to $18\,\mathrm{mm}$ (cf.Figure 6.1 and Figure 6.8.)

When the improvements were completed, sTFMS was assembled, adjusted, and again calibrated at RT. Afterward, another attempt to conduct LFV measurements using Super-LOFOS was made. Similar to the *experiment-2*, Super-LOFOS was refrigerated with the LHe liquid-flow cooling. This time FC magnetization was done with $B_A = 5\,\mathrm{T}$ to achieve the maximal trapped magnet flux density $^z B_T$. Furthermore, the output voltage of the positioning sensor $\Delta V_{ph}(t)$ as well as temperature $T_{op}(t)$ was monitored during the entire experiment.

However, during the cooling process from $T > T_c$ to T_{op} under $B_A = 5\,\text{T}$, the output signal ΔV_{ph} of the sTFMS positioning sensor disappeared. This can be seen in Figure 6.9 and its insert, which show the time-dependent temperature $T_{op}(t)$ and the output voltage $\Delta V_{ph}(t)$, respectively. An immediate inspection revealed an interrupted electrical connection with the position sensor LED.

Troubleshooting continued by first ramping down the applied field to $B_A = 0\,\text{T}$. Upon then thoroughly inspecting the outside electrical connections and the cable between Super-LOFOS and the measurement equipment, it became clear that the electrical signal for the LED was interrupted inside the Super-LOFOS itself. In order to investigate the exact failure source, the LFV measurements were aborted, then the Super-LOFOS was warmed up and opened.

Failure investigation. The failure investigation revealed that there was a broken wire between the vacuum feedthrough and the LED inside the CFC. Additionally, the movable aperture of the positioning sensor was bent again in spite of the controlled rotation around the z-axis, see Figure 6.10 a).

The interrupted electrical contact was an annoying but manageable failure. However, the repeated damage to and displacement of the sensor aperture was a severe issue requiring further investigations.

Figure 6.10 b)-c) shows the simplified structure of the sTFMS outlining the posi-
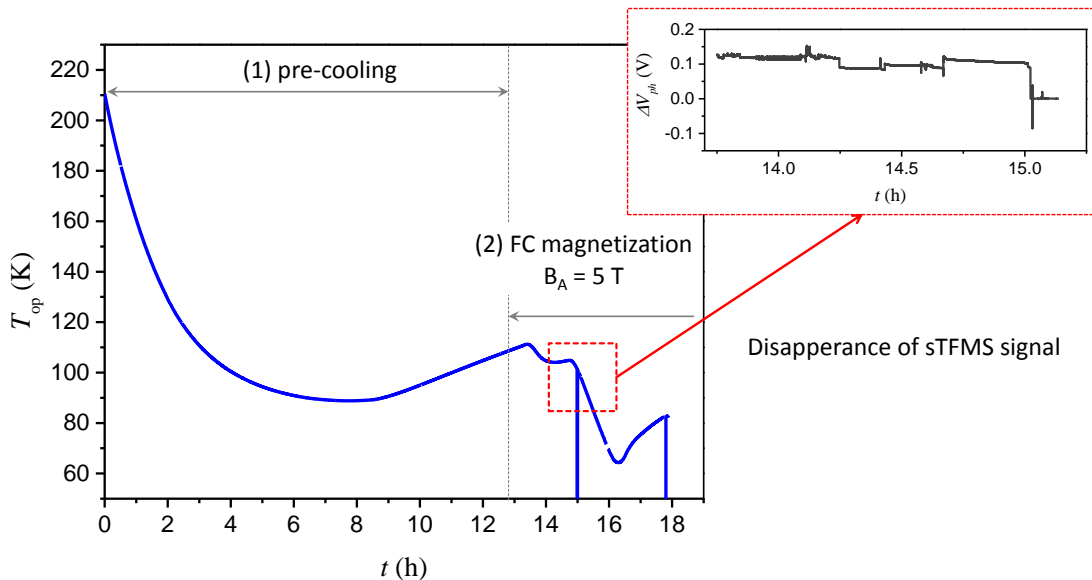
Figure 6.9: The second LHe liquid-flow cooling, followed by the FC magnetization with $B_A = 5\,\text{T}$. *Insert* Disappearance of the ΔV_{ph} during magnetization.
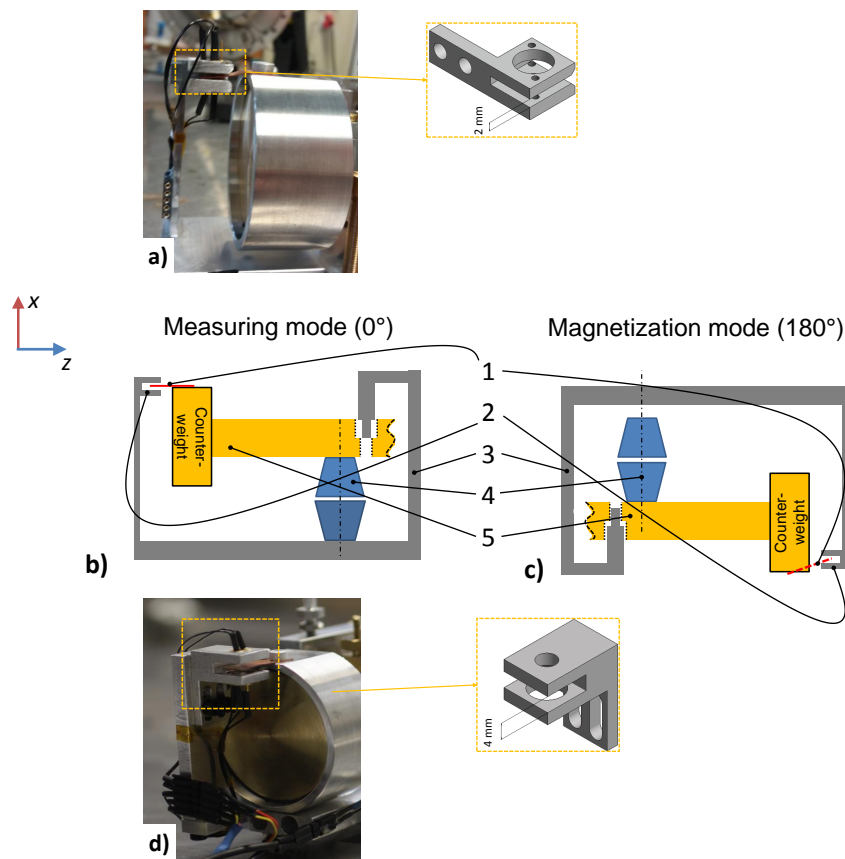
Figure 6.10: **a)** sTFMS photograph showing the repeated bending of the movable aperture of the positioning sensor, *Cutout:* CAD model of the aluminum frame of the positioning sensor. Simplified sTFMS structure outlining the positioning sensor with its (1) aperture, (2) the gap in the aluminum frame, (3) the safety limiter, (4) the flexure bearing, and (5) the lever in **b)** *measuring* and **c)** *magnetization* mode. **d)** sTFMS photograph showing a new aluminium frame design for the positioning sensor. *Cutout:* CAD aluminum frame model for the positioning sensor with an extended 4 mm-gap.

tioning sensor including the (1) aperture and (2) the aluminum frame as well as (3) the safety limiter in *measuring* and *magnetization* mode, respectively. Apparently, bending occured when sTFMS was rotated to the *magnetization mode*: The gap, at which the safety limiter is sunk, does not match the gap provided by the aluminum frame of the positioning sensor.

6.2.3 Experiment-3: Position sensor re-design and the sTFMS verification.

To ensure that the aperture does not bend, the positioning sensor was redesigned by Na Yan and is shown in Figure 6.10 d). The gap in the aluminum frame was widened from 2 mm to 4 mm.

The next steps were to adjust and calibrate the sTFMS. However, before assembling the Super-LOFOS and beginning with the LFV measurements, the decision was made to verify the sTFMS using an electrostatic force balancing (EFB) at room and LN$_2$ temperatures.

Electrostatic force balancing (EFB). The EFB was introduced by Yan [22] by embedding a capacitor into the sTFMS construction. Figure 6.11 a) highlights the embedded sTFMS capacitor, while Figure 6.11 b) shows further capacitor details.
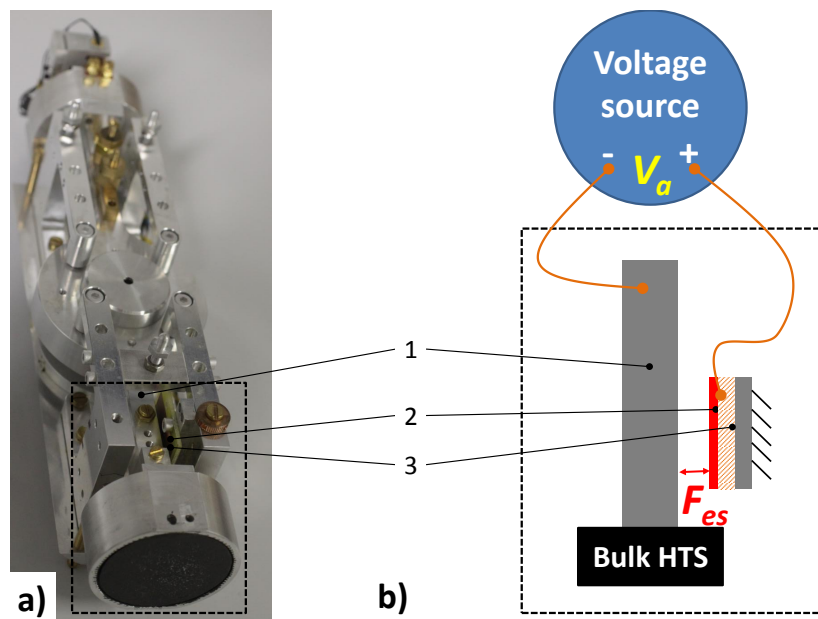
Figure 6.11: Electrostatic force balancing with the embedded capacitor. **a)** photograph and **b)** the capacitor schematics, which includes (1) a cathode (a part of whole conducting sTFMS structure), (2) an anode (a copper rectangular plate that is firmly attached to the safety limiter), (3) G-10 substrate for electrical isolation. An electrostatic voltage V_a can be applied using a dc voltage source.

The capacitor consists of (1) a cathode, which is a part of whole conducting sTFMS structure, (2) an anode, which is formed from a copper rectangular plate that is firmly attached to the safety limiter and is electrically isolated from it via the (3) G-10

substrate. Thus, a plate-shaped capacitor is engineered for two close electrodes that are separated by air at RT and gaseous He, when sTFMS is placed in the CFC.

The idea of the sTFMS verification using EFB is to excite a deliberate electrostatic force F_{es}, which is then measured as ΔV_{ph} by the sTFMS. The control of the force F_{es} is managed by applying an electrostatic voltage V_a across the engineered capacitor. The calibration of the $F_{es}(V_a)$ dependency was carried out by Yan [22] and is expressed as:

$$F_{es} = K_{es} \cdot V_a^2 \tag{6.1}$$

where $K_{es} \approx 0.04\,\mu\mathrm{N}\,\mathrm{V}^{-2}$.

A sequence of twelve EFB measurements at RT were conducted by applying a stepwise electrostatic voltage $V_a = [0; 10; 0]\mathrm{V}$ between the capacitor electrodes to monitor the positioning sensor's $\Delta V_{ph}(t)$. A separate EFB measurement is displayed as a set of the positioning sensor operating temperature $T_{op}(t)$, the applied electrostatic voltage $V_a(t)$, and the output voltage $\Delta V_{ph}(t)$ in Figure 6.12 a)-c), respectively. By comparing obtained results, it is clear that stepwise applying of V_a leads to the stepwise function of $\Delta V_{ph}(t)$. This implies that sTFMS operates properly, particularly:

1) imposed force F_{es} leads to the anticipated elastic rotation of sTFMS lever, which is reflected as oscillating $\Delta V_{ph}(t)$,

2) sTFMS is sensitive to F_{es} force in μN range.
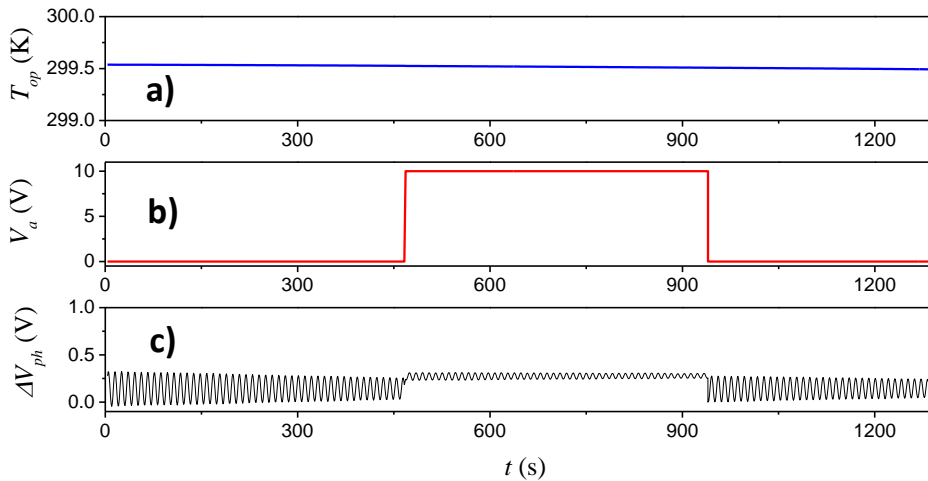
Figure 6.12: electrostatic force balancing results at RT as a set of **a)** operating temperature $T_{op}(t)$, **b)** applied electrostatic voltage $V_a(t)$, and **c)** the positioning sensor output voltage $\Delta V_{ph}(t)$.

Afterward, the sTFMS was assembled into the Super-LOFOS following two first steps listed in Table 6.1 and prepared for the EFB measurements at LN_2 temperature.

During LN_2-cooling, however, the output signal ΔV_{ph} of the sTFMS positioning sensor dropped from $-1.25\,V$ to $-20\,V$ at $T_{op} = 202\,K$ and finally disappeared at $T_{op} = 230\,K$, as documented in Figure 6.13. An immediate troubleshooting revealed an interrupted electrical LED connection analog to the second attempt of *experiment-2* (cf. Section 6.2.2). Therefore it was suspected that the electrical contact was somehow detached.
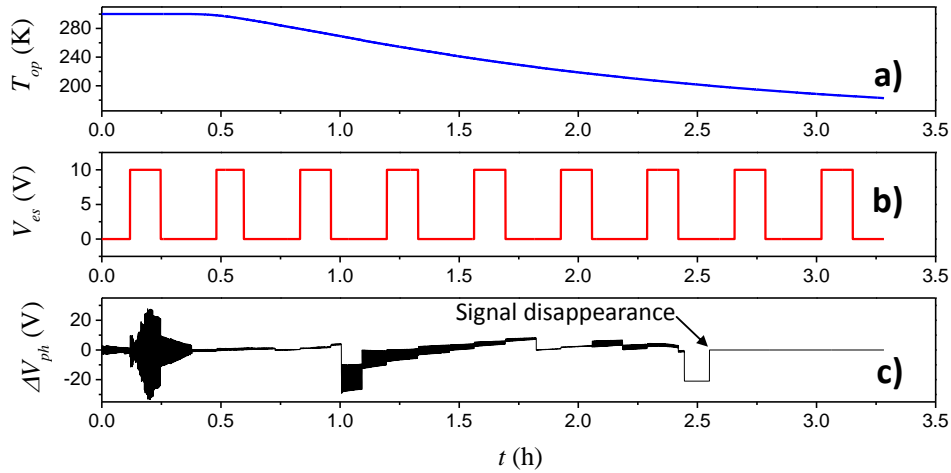
Figure 6.13: electrostatic force balancing results at LN_2 temperature as a set of **a)** operating temperature $T_{op}(t)$, **b)** applied electrostatic voltage $V_a(t)$, and **c)** the positioning sensor output voltage $\Delta V_{ph}(t)$.

Failure investigation. Surprisingly, the examination revealed that all electrical contacts were intact without any visible damage. Subsequently, the LED was subjected to a $V - I$ inspection. Applying $I_{ex} = 3\,mA$ it was indicated that a forward voltage $V_{LED} = 16.4\,V$ significantly exceeds a typical value $V_{LED} = 1.25\,V$ to $1.45\,V$ according to manufacture specifications [226]. Furthermore, $V - I$ characteristics were measured on three identical, but separate LED (L9337-02, Hamamatsu) at RT and $77\,K$[6]. Table 6.2 summarizes the obtained results indicating that the LED (used in *experiment-3*) is defective. It was necessary to examine if the LED failure was due to the cryogenic temperature.

In general, manufacturers of diodes provide information about the operation parameters of their components at about $230\,K$ to $240\,K$ [226, 227]. Diode-based systems

---

[6]Each LED was just immersed into the vessel with LN_2.

Table 6.2: $V-I$ inspection of the used LED (L9337-02, Hamamatsu) and comparison to other LEDs at RT and 77 K. Data is represented as a forward voltage V_{LED} after applied excitation current $I_{ex} = 3\,\text{mA}$.

LED	V_{LED}, (V)		comment
(L9337-02, Hamamatsu)	RT	77 K	
used	16.14	16.13	defected
(1)	1.3	1.7	o.k.
(2)	1.3	1.7	o.k.
(3)	1.3	1.7	o.k.

have been utilized in cryogenic environment in space and medical applications [228], as well as in nuclear and particle physics [229–232]. These works identified the advantages and feasibility of using diodes, but also warned about anticipated barriers.

Yang *et al* [232] investigated large-area silicon avalanche photodiodes and determined that at a given excitation current, the gain voltage increased with decreasing temperature. Such a tendency is consistent with the fact that the carriers mobility increases with lowering temperature, thus reducing phonon scattering [233]. Moreover, Yang *et al* [232] also determine a critical temperature of $T_{freeze} = 40\,\text{K}$, at which light-dependent diodes no longer function properly due to the so-called "freeze-out effect". The adverse influence of the thermal cycling has been reported for some commercial diodes in [228, 231].

Because of the three issues discussed above, the sTFMS positioning sensor, in particular the utilized LED and differential photodoide, were validated at cryogenic temperatures, which is discussed in the next section.

Verification of the position sensor at LN$_2$ temperature. The positioning sensor, the working principle of which was presented in Section 5.2.4, includes two off-the-shelf diodes: LED (Infrared LED L9337, Hamamatsu) [226] and photodiode (Silicon differential photodiode SFH221S, Siemens) [227]. Both light-dependent diodes have a hermetically sealed metal housing with a glass window (BPX65) or respectively a glass lens (OD880F). This results in a good protection against environmental influences at RT [234].

Figure 6.14 a) sketches the verification experimental setup. It includes (1) SFH221S photodiode and (2) L9337 LED, which were fixed at the (3) aluminum frame of sTFMS position sensor, as sketched in Figure 6.14 a). In this configuration, an excitation current I_{ex} was applied to the LED to illuminate the photodiode and resultant voltages V_{LED} as well as V_{ph} were then measured. Figure 6.14 b)-c) indicates the circuit

diagrams for both cases. It should be stressed that $V - I$ characteristics for each light-dependent diode were taken at RT and 77 K.

Obtained data is shown in Figure 6.15. It can be seen that the measured voltages $V_{LED(77K)}$ and $\Delta V_{ph(77K)}$ at the same excitation current are higher that those for RT. This is consistent with the data reported in [228, 229]. The results of $V - I$ characterization revealed that tested light-dependent diodes can be used at cryogenic temperatures and reliably serve for the sTFMS position sensor, but the I_{ex}-regulation of the LED must be attenuated in order to avoid the saturation of the forward voltage. Accordingly, one has to consider the correction to the calibration.

Repeated EFB measurements at RT. The positioning sensor was assembled to the sTFMS and subjected to repeated EFB measurements following the identical procedure as in previous case. Figure 6.16 displays obtained result at RT yielding the oscillating and stepwise behavior of the output signal $\Delta V_{ph}(V_a, t)$. This result was considered as successful, indicating that sTFMS and its component (i.a. positioning sensor and flexure bearing) operate properly.

The next step of the sTFMS verification was to perform LFV measurement accompanied with EFB measurements during LN_2 pre-cooling to attain additional information.
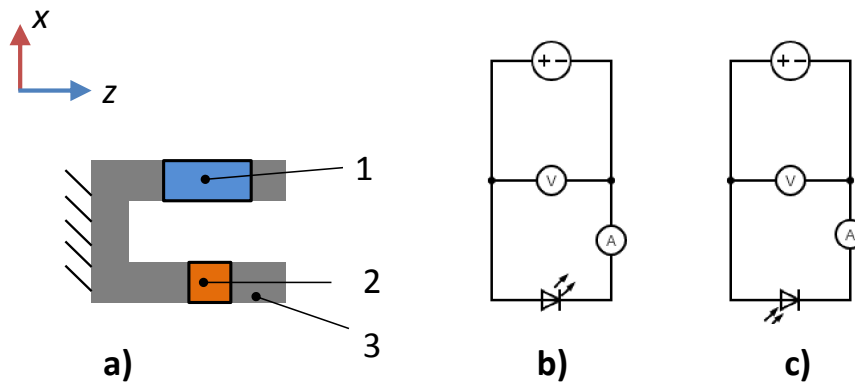
Figure 6.14: **a)** Schematic of the verification experimental setup, which includes (1) SFH221S photodiode and (2) L9337 LED, which are fixed at the (3) aluminum frame of sTFMS position sensor. The circuit diagram for the $V - I$ measurements with **b)** LED and **c)** photodiode at RT and 77 K.

.
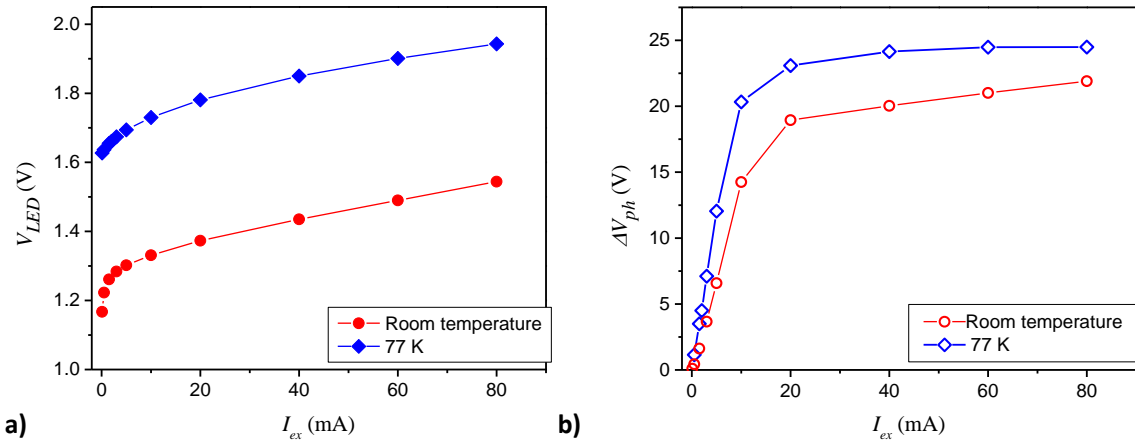
Figure 6.15: **a)** $V - I$ curves of the LED (V_{LED}) and **b)** the photodiode (V_{ph}) at prescribed I_{ex} of the LED at RT and 77 K.

6.2.4 Experiment-4: EFB and LFV measurements at LN$_2$.

The sTFMS was assembled into the Super-LOFOS followed by the preparation steps listed in Table 6.1. During LN$_2$ pre-cooling EFB measurements were conducted to monitor the behavior of sTFMS followed by the LFV measurements with the aluminum rod. Figure 6.17 shows the temperature as a function of time and indicates the experimental steps.
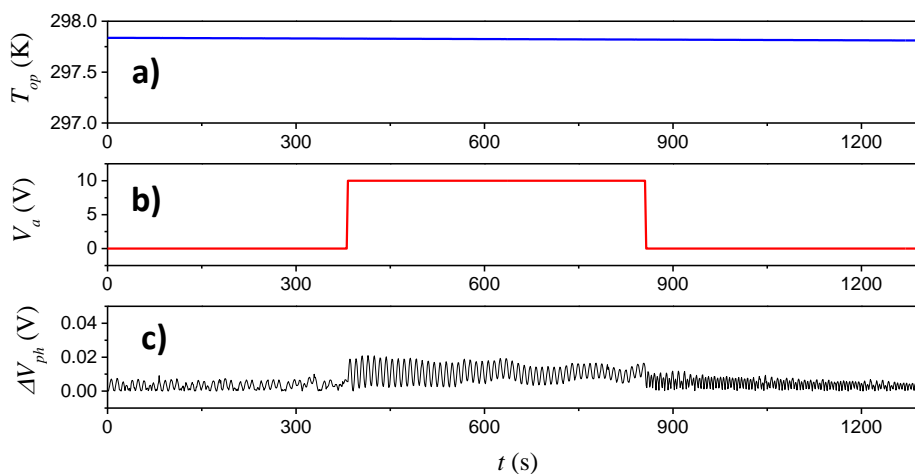
Figure 6.16: Repeated electrostatic force balancing results at RT as a set of **a)** operating temperature $T_{op}(t)$, **b)** applied electrostatic voltage $V_a(t)$, and **c)** the positioning sensor output voltage $\Delta V_{ph}(t)$.
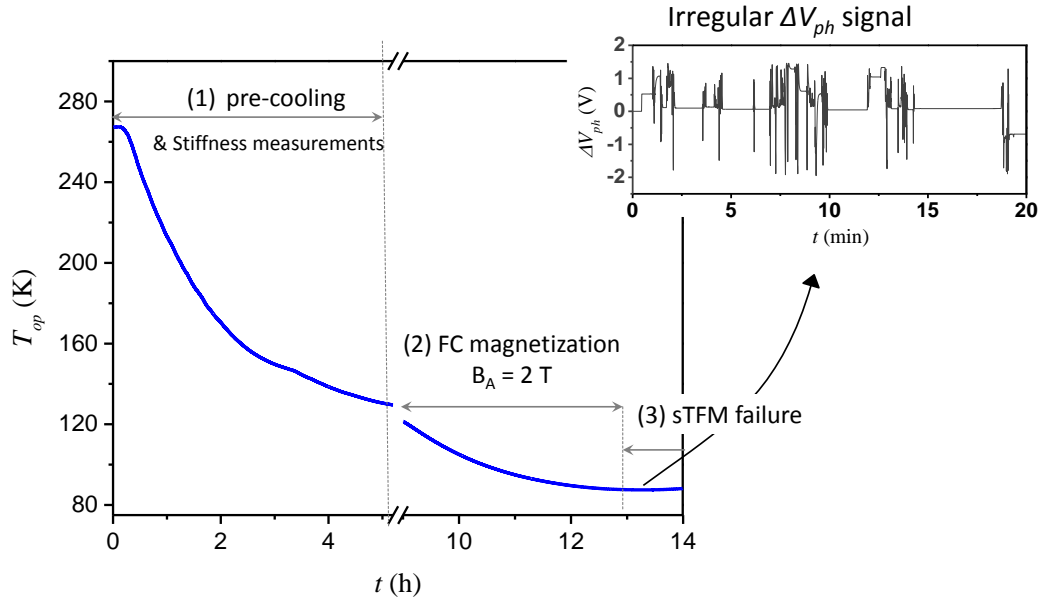
Figure 6.17: LN$_2$ liquid-flow cooling, followed by the ZFC magnetization with $B_A = 2$ T. *Insert* shows obtained ΔV_{ph} right after sTFMS is brought to the *measuring mode*.

EFB measurements. The EFB measurements were performed in the identical manner as in the previous measurements applying $V_a = [0; 10; 0]$V down to 100 K (cf. Figure 6.13). The $\Delta V_{ph}(t)$ increased with deceasing temperature, which is consistent with the observation of Yang [232] and results of $V - I$ measurements on light-dependent diodes (cf. Section 6.2.3).

A counterintuitive effect was encountered, whereby the stepwise function of V_a led to the upshift of $\Delta V_{ph}(t)$ in contrast to the anticipated downshift. It is shown in Figure 6.18, which presents an example of EFB measurement upon cooling from $T = 177$ K to 168 K. The observed effect indicated that sTFMS was not operating properly. On the one hand, the oscillating $\Delta V_{ph}(t)$ signal indicates that the sTFMS lever periodically rotates, but on the other hand, the upshift of $\Delta V_{ph}(t)$ might suggest that the elasticity of the flexture bearing is affected.

It is important to stress that the "$\Delta V_{ph}(t)$ upshift" effect was noticed not during EFB measurements, rather after them as well as after LFV measurements.

Magnetization and LFV measurements. The magnetization followed the FC process involving the application of $B_A = 2$ T and subsequent cooling to $T_{op} \approx 85$ K. As a result, the field of $^z B_T = 100$ mT at the front surface of Super-LOFOS was trapped.

When the Super-LOFOS was brought to the *measuring mode*, the positioning sensor
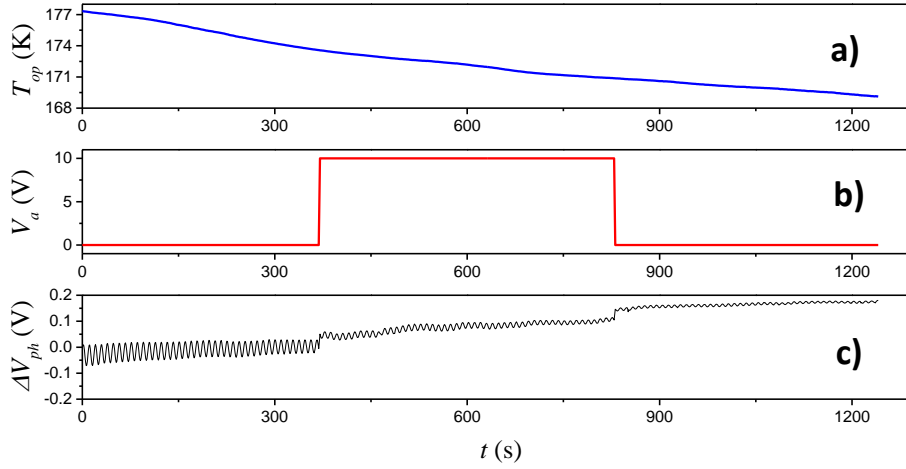
Figure 6.18: Repeated electrostatic force balancing results at LN_2 temperature as a set of **a)** operating temperature $T_{op}(t)$, **b)** applied electrostatic voltage $V_a(t)$, and **c)** the positioning sensor output voltage $\Delta V_{ph}(t)$.

displayed an abnormal and irregular ΔV_{ph} signal, as shown in the inset of Figure 6.17.

Since such a signal can imply that the sTFMS lever is blocked and not rotating freely, immediate steps were taken to release the lever in order to achieve the periodically oscillating ΔV_{ph} signal. However, all attempts to resolve the problem did not bring the desired results, so that all LFV measurements were halted before beginning the failure investigation.

Failure investigation. The examination revealed no damage or deviance of the positioning sensor or its components. Moreover, all electrical connections were intact. Figure 6.19 a) shows that upon opening CFC, the movable aperture is located in the gap between the aluminum frame and the positioning sensor and moves freely. This shows that re-designing the positioning sensor (i.e. extending of the gap from the 2 mm to 4 mm) prevented the bending of the aperture.

Afterward, the sTFMS was placed and adjusted in the horizontal plane (see Figure 6.19 b) to test whether it operates properly at RT. After engaging the sTFMS lever, it rotated again abnormally and stopped. The positioning signal showed irregular oscillations of ΔV_{ph} followed by the finite ΔV_{ph} signal, as recorded in Figure 6.19 c). Such behavior was a clear sign that sTFMS rotation was adversely degraded. Importantly, this time no mechanical bending of the positioning sensor aperture, nor effects related to the diodes at cryogenic temperatures led to the failure.

The sTFMS rotation degradation could be attributed to the ferromagnetic and
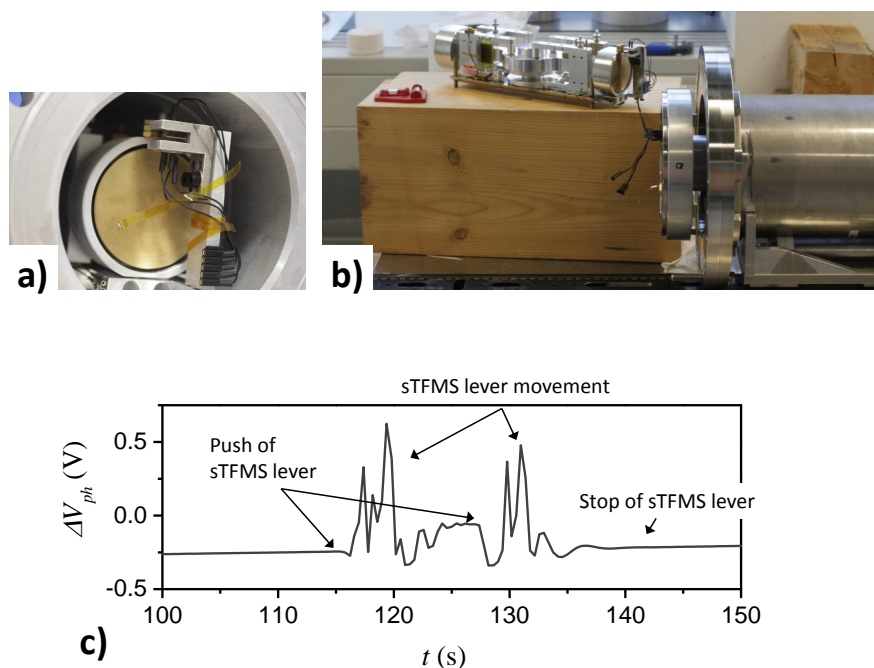
Figure 6.19: The results: **a)** A photograph of the movable aperture immediately after opening the CFC. It is shown that the aperture can move freely in the gap between positioning sensor's aluminum frame. **b)** sTFMS adjustment at RT showing **b)** irregular ΔV_{ph} signal.

thermal properties of the flexure bearing which is made from AISI 420 steel. At first, AISI 420 steel's high magnetic susceptibility ($\chi = 950$) is the reason of tremendous magnetic forces exerting on the sTFMS flexure bearing during magnetization (cf. Chapter 5). Although the sTFMS safety inset was developed to mitigated this force impact, the martensitic AISI 420 steel is metastable and can undergo structural transition when thermally strained, deformed, or welded [99]. This, in turn, can lead to geometry and mechanical (e.g. elasticity, stiffness) changes which result in flexure bearing degradation.

An alternative to the AISI 420 steel for the flexure bearing construction would be austenitic AISI 304/316 stainless steels (a common material for high-field and cryogenic temperature measurements) and titanium, which have a magnetic susceptibility at least five orders of magnitude smaller, see Table 5.3. In addition to the magnetic properties, the thermal characteristics such as reproducibility on thermal cycling, long-term thermal drift are vital issues for the flexure bearing material selection.

6.3 Chapter summary

This chapter described a number of experiments to validate Super-LOFOS. The important obtained results and conclusions are summarized as follows:

1) Using the integrating cooling concept the bulk HTS and sTFMS were effectively refrigerated together down to T_{op} enabling bulk HTS to be magnetized so that magnetic flux density $^z B_T$ at the Super-LOFOS outer front surface was generated. The obtained results are presented in Table 6.3.

Table 6.3: Super-LOFOS test results on achieved operating temperature T_{op}, trapped magnetic flux density $^z B_T$ at the Super-LOFOS outer front surface using LN$_2$ or LHe refrigeration.

Experiment	Cryogenic liquid	T_{op}	Magnetization/ B_A	$^z B_T$
1)	LN$_2$	88.8 K	ZFC/2 T	0.02 T
2)	LHe	46 K	FC/4 T	1.2 T
3)	LHe	<70 K	FC/5 T	failed
4)	LN$_2$	85 K	FC/2 T	0.1 T

2) The modular Super-LOFOS cryostat structure allowed us to use the available LHe/LN$_2$ cooling cryostat manufactured by ILK Dresden [204]. Although this LHe/LN$_2$ cryostat was initially developed to cool only a single bulk HTS, connecting the LHe/LN$_2$ cryostat with an either LN$_2$ or LHe storage dewar enabled a continuous liquid-flow cooling of the Super-LOFOS measuring cryostat (containing bulk HTS and sTFMS) down to required operating temperatures, see Table 6.3.

3) Time of 5-15 h was needed to cool bulk HTS below $T < 100$ K and is attributed to the cumulative Super-LOFOS specific heat and unoptimized regulation of the continuous liquid-flow cooling. In principle, such a cooling resembles a simplified closed-cycle refrigerator system. In the future, the optimized closed-cycle refrigerator system can be easily adapted to the Super-LOFOS measuring cryostat, thereby increasing cooling effectiveness.

4) Using electrostatic force balancing (EFB) and LFV measurements the Super-LOFOS functionality has been tested.

4.1) Using LN_2 cooling and aluminum rod dry calibration, the LFV measurements for two velocities were performed. The obtained results were anticipated, but not reproducible. Further attempts to conduct LFV measurements using either an aluminum rod or a model electrolyte dry calibration failed. The failures were caused by different reasons which were thoroughly examined and corrected.

4.2) Using electrostatic force balancing (EFB) measurements and separate position sensor examination enabled us to elucidate and deepen the understanding of sTFMS functionality under cryogenic temperature and magnetic field conditions.

    4.2.1) Separate examination of the position sensor light-dependent diode compounds, namely, LED (Infrared LED L9337, Hamamatsu) [226] and photodiode (Silicon differential photodiode SFH221S, Siemens) [227] revealed their proper function at 77 K if the light-dependent diode excitation current is accordingly attenuated.

    4.2.2) The light-dependent diodes were assembled to form sTFMS position sensor and the sTFMS functionality was then investigated from RT down to 77 K.

    4.2.3) Using EFB measurements the proper sTFMS functionality at RT and down to 77 K was confirmed: the oscillating $\Delta V_{ph}(t)$ signal measured by the positioning sensor indicated that the sTFMS lever periodically rotates, as anticipated.

    4.2.4) However, the sTFMS dysfunction was detected after FC magnetization (a part of LFV measurements) followed applying $B_A = 2\,T$ and cooling to $T_{op} \approx 85\,K$. An immediate examination at 85 K and followed examination at RT indicated that the flexure bearing does not rotate freely.

4.3) sTFMS functionality was clearly affected in a result of the cryogenic temperature and magnetic field. In particular, the sTFMS rotation malfunction could be attributed to the ferromagnetic and thermal properties of the flexure bearing which is made from AISI 420 steel.

    4.3.1) AISI 420 steel's high magnetic susceptibility ($\chi = 950$) is the reason of tremendous magnetic forces acting on the sTFMS flexure bearing during magnetization (cf. Chapter 5). Although the sTFMS safety

inset was developed to mitigated this force impact, the martensitic AISI 420 steel is metastable and can undergo structural transition when thermally strained, deformed, or welded [99].

4.3.2) This, in turn, can lead to geometry and mechanical (e.g. elasticity, stiffness) changes which result in flexure bearing degradation.

4.3.2) An alternative to the AISI 420 steel for the flexure bearing construction would be austenitic AISI 304/316 stainless steels (a common material for high-field and cryogenic temperature measurements) and titanium, which have a magnetic susceptibility at least five orders of magnitude smaller, see Table 5.3. In addition to the magnetic properties, the thermal characteristics such as reproducibility on thermal cycling, long-term thermal drift are vital issues for the flexure bearing material selection.

7 Summary and Outlook

7.1 Summary

In order to use Lorentz Force Velocimetry (LFV) for velocity measurements of low-conducting ($\sigma < 10\,\mathrm{S\,m^{-1}}$) and slow-flowing ($u < 1\,\mathrm{m\,s^{-1}}$) electrolytes, high-precision force measurements below $1\,\mathrm{\mu N}$ and the magnetic field generation over $1\,\mathrm{T}$ are required. A bulk HTS can generate a magnetic field of several teslas and therefore was proposed for use in LFV.

The present thesis investigates the possibility of integrating bulk HTS into the LFV considering requirements regarding refrigeration and magnetization as well as enabling the synergistic functionality of the bulk HTS and the FMS, which is the other integral LFV part. The end goal is to design, manufacture, and test a novel and improved LFV system for velocity measurements of low-conducting and slow-flowing electrolytes.

The approach used in the investigations as well as important results and conclusions are summarized as follows:

1. It was experimentally proven, for the first time, that bulk HTS using simplified liquid nitrogen cooling is feasible for LFV applications. This was a vital intermediate step indicating that bulk HTS can potentially generate magnetic flux densities over $1\,\mathrm{T}$ for LFV applications. In addition to the experiment, a 3D numerical model was developed. The obtained experimental and numerical simulation results agreed well, exhibiting the linear relationship between the Lorentz force and product of the electrical conductivity and velocity in accordance with LFV theory. The developed numerical model was used to calculate necessary trapped magnetic flux densities B_T for future LFV measurements of the model electrolyte with $(\sigma \cdot u) = 10\,\mathrm{S\,s^{-1}}$.

2. Commercial off-the-shelf Y-Ba-Cu-O bulk HTSs were investigated to define their mechanical stability and reproducibility, as well as the trapped field capability.

High-field measurement tests revealed that encapsulating the bulk HTS with either an aluminum or stainless steel tubes are both equally suitable and effective reinforce-

ments. The used bulk HTSs trapped the reproducible magnetic flux density in the range of 6 T to 7 T at the bulk HTS surface.

3. The obtained results were then used to develop a novel LFV system which is referred as to **Super**conducting High-precision **Lo**rentz **Fo**rce Measurement **S**ystem (Super-LOFOS) comprised of the bulk HTS as magnetic field generator and scaled-down Torsion Force Measurement System (sTFMS) as the FMS. The Super-LOFOS novelty lies in using an integrated cooling of the bulk HTS and sTFMS as well as in the modular cryostat structure.

3.1. Using integrated cooling eliminated the FMS mass limitation to carry the bulk HTS magnet system and enabled the contacless cooling of the bulk HTS and sTFMS, thereby excluding sTFMS constrains due to the direct thermal coupling. The Super-LOFOS integrated cooling was validated experimentally. Using nitrogen and helium cryogenic liquids, the magnetic flux density of $B_T = 100$ mT at $T_{op} \approx 85$ K and $B_T = 1.2$ T at $T_{op} \approx 46$ K were generated on the Super-LOFOS front surface, respectively.

3.2. The modular Super-LOFOS cryostat structure allowed us to use the available LHe/LN$_2$ cooling cryostat. Connecting the LHe/LN$_2$ cryostat with either an LN$_2$ or LHe storage dewar enabled a continuous liquid-flow cooling of the bulk HTS integrated with sTFMS) down to required operating temperatures.

Bulk HTS cool-down time below $T < 100$ K lasted 5-15 h and is attributed to the cumulative Super-LOFOS specific heat and unoptimized regulation of the continuous liquid-flow cooling, which resembles a simplified closed-cycle refrigerator system. In order to improve and optimize Super-LOFOS cooling the closed-cycle refrigerator system can be further developed in the future.

4. Using electrostatic force balancing (EFB) and LFV measurements, the Super-LOFOS functionality as well as the functionality of its components were tested.

Using LN_2 cooling and aluminum rod dry calibration, the LFV measurements, were performed for two velocities. The obtained results were anticipated, but not reproducible. Further attempts to conduct LFV measurements using either an aluminum rod or a model electrolyte dry calibration failed. The failures were caused by different reasons which were thoroughly examined and corrected. Failures related to the sTFMS position sensor functionality and the sTFMS flexure bearing functionality were identified as the most important:

sTFMS position sensor The functionality of the sTFMS position sensor, which is based on light-dependent diodes, was investigated under cryogenic temperatures. Separate investigations of the position sensor light-dependent diode compounds (LED and photodiode) revealed their proper function at $77\,K$ if the light-dependent diode excitation current is accordingly attenuated. Furthermore, when LED and photodiode were re-assembled to the sTFMS position sensor, temperature-dependent tests showed that the utilized sTFMS position sensor can reliably serve at cryogenic temperatures.

sTFMS flexure bearing sTFMS dysfunction was detected after FC magnetization followed applying $B_A = 2\,T$ and cooling to $T_{op} \approx 85\,K$. An immediate examination at $85\,K$ and following examination at RT indicated that the flexure bearing does not rotate freely. Influences of cryogenic temperatures and magnetization were identified as primary challenges hampering proper sTFMS functionality.

The sTFMS rotation malfunction could be attributed to the ferromagnetic and thermal properties of the flexure bearing which is made of AISI 420 steel. AISI 420 steel's high magnetic susceptibility ($\chi = 950$) is the reason for the tremendous magnetic forces exerted on the sTFMS flexure bearing during magnetization.

Although the sTFMS safety inset was developed to mitigate this force impact, the martensitic AISI 420 steel is metastable and can undergo structural transition when thermally strained, deformed, or welded [99]. This, in turn, can lead to geometry and mechanical (e.g. elasticity, stiffness) changes which result in flexure bearing malfunction.

7.2 Outlook

The present thesis addresses the challenge of integrating bulk HTS into the LFV pursuing the goal to generate a magnetic flux density over 1 T and develop the improved LFV system for velocity measurements of low-conducting and slow-flowing electrolytes. Although such an LFV system was designed manufactured, and tested, its applications for velocity measurements were hampered by the sTFMS dysfunction under the cryogenic temperatures and magnetic field. On this basis, suggestions for future investigations are classified as follows:

1) The important *short-term milestone* is to verify the flexure bearing functionality under a magnetic field. At first, one can continue investigations with the utilized flexure bearing made from AISI 420 steel. In order to understand the magnetic field influence on the flexure bearing and sTFMS functionality, the EFB measurements at RT with the sTFMS (not enclosed in the CFC) must be performed within the 5TCFM at various applied magnetic field from 0 T to 5 T.

   Later, one can repeat magnetic field investigations of the flexure bearing made of low-magnetic material such as AISI 304/316 steel or titanium.

   This will facilitate the understanding of how the magnetic field impacts the flexure bearing as well as helping to diagnose and find remedies for any failures that might occur in the future.

2) The next *short-term milestone* is to verify the sTFMS at cryogenic temperatures using EFB and LFV measurements. It is crucial to understand how the flexure bearing behaves at cryogenic temperatures, especially also after thermal cycling. It might be helpful to use temperature control by means of a Manganin wire-wound heater, which radially envelops the CFC.

3) It is necessary to find a safety method in order to eliminate the action of the Lorentz and magnetic vector gradient forces on the bulk HTS during magnetization.

4) The *middle-term milestone* is to optimize and improve the magnetic field generation using bulk HTS. There is a number of factors to improve magnetic field generation, but the most straightforward way is to increase the bulk HTS volume using larger or multi-seeded bulk HTS or even configurating bulk HTS from several samples.

5) The *long-term milestone* is to optimize or re-design the Super-LOFOS cooling cryostat, adapting the closed-cycle refrigerator system or a continuous-flow cryostat. In contrast to a mechanical cryocooler, both cooling systems do not vibrate and are therefore more suitable for high-precision force measurements.

6) Another *long-term milestone* is to magnetize the bulk HTS using the PFM instead of FC magnetization in order to make the Super-LOFOS more commercially attractive: a flow-meter which is faster, more compact, and portable.

Bibliography

[1] A. Thess, E. Votyakov, and Y. Kolesnikov. Lorentz force velocimetry. *Phys. Rev. Lett.*, 96:164501, Apr 2006.

[2] A. Thess, E. Votyakov, and Y. Kolesnikov. Theory of the lorentz force flow meter. *New J. Phys*, 9:. 299, Apr 2007.

[3] C. Weidermann. *Design and laboratory test of a Lorentz force flowmeter for pipe flows.* PhD thesis, Techniche Universität Ilmenau, 2016.

[4] V. Minchenya, C. Karcher, Y. Kolesnikov, and A. Thess. Lorentz force flowmeter in industrial application. *Magnetohydrodynamics*, (3):459–465, 2009.

[5] Y. Kolesnikov, C. Karcher, and A. Thess. Lorentz force flowmeter for liquid aluminum: Laboratory experiments and plant tests. *Metallurgical and Materials Transactions B: Process Metallurgy and Materials Processing Science*, 42(3):441–450, 2011.

[6] Y. Kolesnikov. Contactless flow measurement in liquid metal using electromagnetic time-of-flight method. *Measurement Science and Technology*, 27:242–247, 2012.

[7] I. Sokolov. *Lorentz Force Velocimetry at High Magnetic Reynolds Numbers.* PhD thesis, Technishe Universität Ilmenau, 2016.

[8] Z. Lyu, C. Karcher, Y. Kolesnikov, and Th. Boeck. Electromagnetic flow rate measurement in molten tin circulating in a closed-loop test system. *IOP Conference Series: Materials Science and Engineering*, 424(1), 2018.

[9] A. Wegfrass, C. Diethold, M Werner, C. Resagk, T. Fröhlich, B. Halbedel, and A. Thess. Flow rate measurement of weakly conducting fluids using lorentz force velocimetry. *Measurement Science and Technology*, 23(10):105307, 2012.

[10] A. Wegfrass, C. Diethold, M. Werner, T. Fröhlich, B. Halbedel, F. Hilbrunner, C. Resagk, and A. Thess. A universal noncontact flowmeter for liquids. *Applied Physics Letters*, 100(19):194103, 2012.

[11] B. Halbedel, C.Resagk, A. Wegfrass, C. Diethold, M. Werner, F. Hilbrunner, and A. Thess. A novel contactless flow rate measurement device for weakly conducting fluids based on lorentz force velocimetry. *Flow, Turbulence and Combustion*, 92(1-2):361–369, 2014.

[12] P. Havel. Overview of automatic controlof glass furnaces. *Ceramics – Silikáty*, 50(1):51–55, 2005.

[13] E. Muijsenberg, M. Eisenga, and J. Buchmayer. *Increase of Glass Production Efficiency and Energy Efficiency with Model-Based Predictive Control*, pages 143–149. John Wiley & Sons, Ltd, 2010.

[14] E. Muijsenberg, J. David, M. Dobka R. Mackh, and J. Leckert. Complete model based control glass production. In *87. Glastechnische Tagung, Bremen*, 2013.

[15] C. Fröba. Optimization of container production with plunger process control. *Glasingenieur*, 1,2-4, 2007.

[16] S. Vasilyan, R. Ebert, M. Weidner, M. Rivero, B. Halbedel, C. Resagk, and T. Fröhlich. Towards metering tap water by lorentz force velocimetry. *Measurement Science and Technology*, 26(11):115302, 2015.

[17] O. Gutfleisch, M. Willard, E. Brueck, C. Chen, S. Sankar, and J. Liu. Magnetic materials and devices for the 21st century: Stronger, lighter, and more energy efficient. *Advanced Materials*, 23(7):821–842, 2011.

[18] S. Vasilyan. *High Precision Force Measurements in Horizontal Direction in Combination with High Dead Loads : Non-Contact Flowmeter for Low Conducting.* PhD thesis, Technische Universität Ilmenau, 2016.

[19] J. O. Torres-Perez. *Nutzung von Lorentzkräften für Mischprozesse in der Chemie- und Glasindustrie.* PhD thesis, Technische Universität Ilmenau, 2016.

[20] K. Müller, G. Krabbes, J. Fink, S. Gruß, A. Kirchner, G. Fuchs, and L. Schultz. New permanent magnets. *Journal of Magnetism and Magnetic Materials*, 226-230(PART II):1370–1376, 2001.

[21] J. Durrell, A. Dennis, J. Jaroszynski, M. Ainslie, K. Palmer, Y. Shi, A. Campbell, J. Hull, M. Strasik, E. Hellstrom, and D. Cardwell. A trapped fi eld of 17.6T in melt-processed , bulk Gd-Ba-Cu-O reinforced with shrink- fit steel. *Superconductor Science and Technology*, 27(082001), 2014.

[22] N. Yan. *High Resolution Force Measurement System for Lorentz Force Velocimetry Dissertation.* PhD thesis, Techniche Universität Ilmenau, 2019.

[23] D. van Delf and P. Kes. The discovery of superconductivity. *Physics Today*, 2(7):38–43, 2010.

[24] All Nobel Prizes. `https://www.nobelprize.org/prizes/lists/all-nobel-prizes/`. Accessed: 2019-08-08.

[25] O. Kamerlingh. Further experiments with liquid helium. d. on the change of the electrical resistance of pure metals at very low temperatures, etc. v. the disappearance of the resistance of mercury. *Communications from the Physical Laboratory at the University of Leiden*, 12(122b):65–71, 1911. Proc. K. Ned. Akad. Wet. 14, 113 (1911).

[26] D. Larbalestier, A. Gurevich, D. Feldmann, and A. Polyanskii. High-Tc superconducting materials for electric power applications. *Nature, Nature Publishing Group*, 414:368, 2001.

[27] O. Kamerlingh. The appearance of the resistance in superconductors, which are brought into a magnetic field, at a threshold value of the field. *Communications from the Physical Laboratory at the University of Leiden*, 13(139f):65–71, 1914.

[28] W. Meissner and R. Ochsenfield. Ein neuer effekt bei eintritt der supraleitfähigkeit. *Naturwissenschaften*, 21(44):787–788, 1933.

[29] A. Abrikosov. Magnetic properties of superconductors of the second group. *Journal of Physics and Chemistry of Solids*, 2(3):199–208, 1957.

[30] L. Shubnikov, V. Khotkevich, Y. Shepelev, and Y. Riabinin. Magnetic properties of superconducting metals and alloys. *Zh. Exper. Teor. Fiz. (USSR)*, 7(2):221–237, 1937.

[31] L. Shubnikov, V. Khotkevich, Y. Shepelev, and Y. Ryabinin. Magnetic properties of superconducting rb 3 c 60. *Ukrainian Physico-Technical Institute, Academy of Sciences of the Ukrainian SSR*, 53(Special Issue):42–52, 2008.

[32] A. Shepelev. The Discovery of Type II Superconductors (Shubnikov Phase). *Superconductor*, 2, 2012.

[33] V. Ginzburg. On superconductivity and superfluiditiy. *Uspehi Fizicheskih Nauk*, 174(11):1240–1255, 2004.

[34] V. Ginzburg and L. Landau. On the theory of superconductivity. *Zh. Exper. Teor. Fiz. (USSR)*, 20(12):1064–1982, 1950.

[35] V. Ginzburg. On the theory of superconductivity. *Nuovo Cimento*, 2(6):1234–1250, 1955.

[36] C. Poole, H. Farach, R. Creswick, and R. Prozorov. *Superconductivity*. Elsevier B.V., Amsterdam, second edition edition, 1995.

[37] P. Goa, H. Hauglin, M. Baziljevich, E. Il'Yashenko, P. Gammel, and T. Johansen. Real-time magneto-optical imaging of vortices in superconducting NbSe2. *Superconductor Science and Technology*, 14(9):729–731, 2001.

[38] G. Krabbes, G. Fuchs, W. Canders, H. May, and R. Palka. *High Temperature Superconductor Bulk Materials*. WILEY-VCH Verlag GmbH & Co. KGaA, Weinheim, 2006.

[39] J. Mazur, J. Kellers, P. Colin, and D. Cardwell. Applied properties of superconducting materials. In David A. Cardwell and David Ginley, editors, *Handbook of superconducting materials*, chapter Applied pr, pages 27–52. Institute of Physics Publishing, Bristol and Phladelphia, 2003.

[40] P. Seidel. *Applied Superconductivity. Handbook on Devices and Applications*, volume 3. Wiley-VHC Verlag GmbH, 1981.

[41] W. Buckel and R. Kleiner. *Supraleitung. Grundlagen und Anwendung*, volume 7. Wiley-VHC Verlag GmbH, 2013.

[42] C. Bean. Magnetization of hard superconductors. *Phys. Rev. Lett.*, 8:250–253, Mar 1962.

[43] C. Bean. Magnetization of high-field superconductors. *Rev. Mod. Phys.*, 36:31–39, Jan 1964.

[44] P. Anderson. Theory of flux creep in hard superconductors. *Physical Review Letters*, 9(7):309–311, 1962.

[45] P. Anderson and Y. Kim. Hard superconductivity: Theory of the motion of abrikosov flux lines. *Reviews of Modern Physics*, 36(1):39–43, 1964.

[46] Y. B. Kim, C. F. Hempstead, and A. R. Strnad. Magnetization and critical supercurrents. *Physical Review*, 129(2):528–535, 1963.

[47] J. Kunzler, E. Buehler, F. Hsu, and J. Wernick. Superconductivity in nb$_3$sn at high current density in a magnetic field of 88 kgauss. *Phys. Rev. Lett.*, 6:89–91, Feb 1961.

[48] K. Tachikawa and P. J Lee. *100 Years of Superconductivity - History of Nb3Sn and Related A15 Wires*. CRC Press, Boca Raton, 2011.

[49] N. Mitchell, P. Bruzzone, M. Spadoni, M. Nishi, A. Shikov, and J. Minervini. Strand production and benchmark testing for the iter model coils. *IEEE Trans. Appl. Supercond.*, 5(2):905–908, 1995.

[50] N. Mitchell, A. Devred, P. Libeyre, B. Lim, and F. Savary. The iter magnets: Design and construction status. *IEEE Transactions on Applied Superconductivity*, 22(3):4200809–4200809, June 2012.

[51] A. Mueller and J. Bednorz. Possible High-T c Superconductivity in the Ba-La-Cu-O System. *Z. Phys. B*, 64:189–193, 1986.

[52] L. Gao, Y. Xue, F. Chen, Q. Xiong, R. Meng, D. Ramirez, C. Chu, J. Eggert, and H. Mao. Superconductivity up to 164 K in Hg-Ba-Ca-Cu-O under quasihydrostatic pressures. *Physical Review B*, 50(6):4260–4263, 1994.

[53] A. Schilling, M. Cantoni, J. D. Guo, and H. R. Ott. Superconductivity above 130 K in the Hg-Ba-Ca-Cu-O system. *Nature*, 363(6424):56–58, 1993.

[54] D. Castelvecchi. Hint seen of new superconductor. *Nature*, 565(7737):12, 2019.

[55] A. Hosono, H.and Yamamoto, Hidenori Hiramatsu, and Yanwei Ma. Recent advances in iron-based superconductors toward applications. *Materials Today*, 21(3):278–302, 2018.

[56] I. Pallecchi and M.Putti. *Applied Superconductivity. Handbook on Devices and Applications*, volume 1, chapter Iron-based Superconductors:Materials Aspect for Applications, pages 166–188. Wiley-VHC Verlag GmbH, 2012.

[57] D. Nardelli, I. Pallecchi, and M. Tropeano. *Applied Superconductivity. Handbook on Devices and Applications*, volume 1, chapter Magnesium Diboride, pages 129–148. Wiley-VHC Verlag GmbH, 2012.

[58] A. Ballarino and R. Flükiger. Status of MgB2 wire and cable applications in europe. *Journal of Physics: Conference Series*, 871:012098, jul 2017.

[59] N. Khare. *Handbook of high-temperature superconductor electronics*. Marcel Dekker, Inc., New Deli, 2003.

[60] B. Lehndorff. *High-Tc Superconducs for Magnet and Energy Technology*. Springer, Berlin, 2001.

[61] F. Werfel, U. Floegel-Delor, R. Rothfeld, T. Riedel, B. Goebel, D. Wippich, and P. Schirrmeister. Superconductor bearings, flywheels and transportation. *Superconductor Science and Technology*, 25(1), 2012.

[62] J. Durrell, M. Ainslie, D. Zhou, P. Vanderbemden, T. Bradshaw, S. Speller, M. Filipenko, and D. Cardwell. Bulk superconductors: A roadmap to applications. *Superconductor Science and Technology*, 31(10):103501, 2018.

[63] F. Werfel. *Applied Superconductivity. Handbook on Devices and Applications*, volume 1, chapter Bulk Materials, pages 193 – 221. Wiley-VHC Verlag GmbH, 2012.

[64] J. Hull. Superconducting bearings. *Supercond. Sci. Technol. 13*, 13(R1-R15), 1999.

[65] J. Hull and M. Murakami. Applications of bulk high-temperature superconductors. *Proceedings of the IEEE*, 92(10):1705–1717, 2004.

[66] M. Murakami. Processing and Applications of Bulk RE-Ba-Cu-O Superconductors. *Int. J. Appl. Ceram. Technol.*, 4(3):225–241, 2007.

[67] T. Oka. Processing and applications of bulk HTSC. *Physica C: Superconductivity and its Applications*, 463-465(SUPPL.):7–13, 2007.

[68] T. Coombs. *Bulk high temperature superconductor (HTS) materials*. Woodhead Publishing Limited, 2011.

[69] D. Zhou, M. Izumi, M. Miki, B. Felder, T. Ida, and M. Kitano. An overview of rotating machine systems with high-temperature bulk superconductors. *Superconductor Science and Technology*, 25(10), 2012.

[70] G. Sotelo, D. Dias, R Jr, and R. Stephan. Tests on a superconductor linear magnetic bearing of a full-scale maglev vehicle. *Applied Superconductivity, IEEE Transactions on*, 21:1464 – 1468, 07 2011.

[71] M. Strasik, J. R. Hull, P. E. Johnson, J. Mittleider, K. E. McCrary, C. R. McIver, and A. C. Day. Performance of a conduction-cooled high-temperature superconducting bearing. *Materials Science and Engineering B: Solid-State Materials for Advanced Technology*, 151(3):195–198, 2008.

[72] T. Nakamura, Y. Itoh, and T. Yoshikawa, M.and Oka. Development of a Superconducting Magnet for Nuclear Magnetic Resonance Using Bulk High-Temperature Superconducting Materials. *Concepts in Magnetic Resonance Part B (Magnetic Resonance Engineering)*, 31 B(2):65–70, 2006.

[73] K. Ogawa, T. Nakamura, Ya. Terada, K. Kose, and T. Haishi. Development of a magnetic resonance microscope using a high Tcbulk superconducting magnet. *Applied Physics Letters*, 98(23):2–5, 2011.

[74] U. Mizutani, T. Oka, Y. Itoh, Y. Yanagi, M. Yoshikawa, and H. Ikuta. Pulsed-field magnetization applied to High-Tc superconductors. *Applied Superconductivity*, 6(98):235–246, 1998.

[75] D. Zhou, M. Ainslie, Y. Shi, Anthony R. Dennis, K. Huang, J. Hull, D. Cardwell, and J. Durrell. A portable magnetic field of >3 T generated by the flux jump assisted, pulsed field magnetization of bulk superconductors. *Applied Physics Letters*, 110(6), 2017.

[76] N. Saho, N. Nishijima, H. Tanaka, and A. Sasaki. Development of portable superconducting bulk magnet system. *Physica C: Superconductivity and its Applications*, 469(15-20):1286–1289, 2009.

[77] K. Yokoyama, E. Kulawansha, Z. Yuanding, and T. Oka. Development of a desktop-type superconducting bulk magnet. *IEEE Transactions on Applied Superconductivity*, 26(4):1–4, June 2016.

[78] K. Yokoyama, A. Katsuki, A. Miura, and T. Oka. Enhancement of Trapped Magnetic Field Using a Large-Size REBCO Bulk in a Desktop Type Superconducting Bulk Magnet. *IEEE Transactions on Applied Superconductivity*, 28(3), 2018.

[79] A Yamamoto. Tokyo University of Agriculture and Technology.

[80] F. Werfel, Uta Floegel-Delor, Rolf Rothfeld, Thomas Riedel, Peter Schirrmeister, Rene Koenig, and Viktor Kantarbar. Impact of Cryogenics and Superconducting Components for HTS Magnetic Levitation Devices. *IEEE Transactions on Applied Superconductivity*, 27(4), 2017.

[81] S. Jin, T. Tiefel, R. Sherwood, M. Davis, and R. van Dover. High critical ccurrent in ybacuo superconductors. *Appl Phys Lett*, 52:2074–2076, 1988.

[82] K. Salama, V. Selvamanickam, L. Gao, and K. Sun. High current density in bulk yba2cu3ox superconductor. *Appl Phys Lett*, 52:2353, 1989.

[83] M Murakami, M Morita, K Doi, and M. Miyamoto. New process with the promise of high jc in oxide superconductors. *JournalJapanese Journal of Applied Physics*, 28(7):1189–1194, 1989.

[84] K. Sawano, M. Morita, M. Tanaka, T. Sasaki, K. Kimura, S. Takebayashi, M. Kimura, and K. Miyamoto. High magnetic flux trapping by melt-grown YBaCuO superconductors. *Japanese Journal of Applied Physics*, 30(Part 2, No. 7A):L1157–L1159, jul 1991.

[85] H. Ikuta, A. Mase, Y. Yanagi, M. Yoshikawa, Y. Itoh, T. Oka, and U. Mizutani. Melt-processed Sm-Ba-Cu-O superconductors trapping strong magnetic field. *Superconductor Science and Technology*, 11(11):1345–1347, 1998.

[86] Adelwitz Technologiezentrum GmbH, Torgau, Germany. `http://atz-gmbh.com/`. Accessed: 2019-08-08.

[87] M. Murakami, S. Gotoh, N. Koshizuka, S. Tanaka, T. Matsushita, S. Kambe, and K. Kitazawa. Critical currents and flux creep in melt processed high tc oxide superconductors. *Cryogenics*, 30(5):390 – 396, 1990. Critical Currents in High Tc Superconductors.

[88] F. Werfel, Uta Floegel-Delor, Thomas Riedel, Rolf Rothfeld, Dieter Wippich, and Bernd Goebel. HTS magnetic bearings in prototype application. *IEEE Transactions on Applied Superconductivity*, 20(3):874–879, 2010.

[89] F. Werfel, U. Floegel-Delor, T. Riedel, R. Rothfeld, P. Schirrmeister, D. Wippich, and R. Koenig. Technical progress in HTS magnetic bulk application development. *IEEE Transactions on Applied Superconductivity*, 25(3), 2015.

[90] G.Fuchs, G.Krabbes, and W. Canders. *Applied Superconductivity. Handbook on Devices and Applications*, volume 1, chapter Properties of Bulk Materials, pages 231–246. Wiley-VHC Verlag GmbH, 2012.

[91] S. Nariki, H. Teshima, and M. Morita. Development of High-Performance QMG Bulk Magnets for High Magnetic Field Engineering Applications. *IEEE Transactions on Applied Superconductivity*, 26(3):3–6, 2016.

[92] S. Nariki, H. Teshima, and M. Morita. Performance and applications of quench melt-growth bulk magnets. *Superconductor Science and Technology*, 29(3), 2016.

[93] S. I. Yoo, N. Sakai, H. Takaichi, T. Higuchi, and M. Murakami. Melt processing for obtaining ndba2cu3oy superconductors with high tc and large jc. *Applied Physics Letters*, 65(5):633–635, 1994.

[94] M. Murakami, N. Sakai, T. Higuchi, and S. I Yoo. Melt-processed light rare earth element - ba - cu - o. *Superconductor Science and Technology*, 9(12):1015–1032, dec 1996.

[95] Nippon Steel Corporation, Tokio, Japan. `https://www.nipponsteel.com/`. Accessed: 2019-08-08.

[96] Y. Shi, A. Dennis, J. Durrell, and D. Cardwell. The effect of size and aspect ratio on the trapped fi eld properties of single grain , Y-Ba-Cu-O bulk superconductors. *Superconductor Science and Technology*, 32(025005):10, 2019.

[97] Tomáš Hlásek and Vladimír Plecháček. Long-Term Quality Observation in Large-Scale Production of Top-Seeded Melt Growth YBCO Bulks. *IEEE Transactions on Applied Superconductivity*, 27(4):1–4, 2017.

[98] CAN superconductors, Prague, Chech Republic. `https://www.can-superconductors.com/`. Accessed: 2019-08-08.

[99] J. Ekin. *Experimental Techniques for Low-Temperature. Cryostat Design, Material Properties, and Superconductor Critical-Current Testing.* Oxford University Press, Oxford, 2006.

[100] D. Cardwell, M. Murakami, M. Zeisberger, W. Gawalek, R. Gonzalez-Arrabal, M. Eisterer, H. W. Weber, G. Fuchs, G. Krabbes, A. Leenders, H. C. Freyhardt, and N. Hari Babu. Round robin tests on large grain melt processed Sm-Ba-Cu-O bulk superconductors. *Superconductor Science and Technology*, 18(2), 2005.

[101] M D Ainslie and H Fujishiro. Modelling of bulk superconductor magnetization. *Superconductor Science and Technology*, 28(5):53002, 2015.

[102] National High Magnetic Field Laboratory (NHMFL) at Florida State University, Tallahassee, USA. `https://nationalmaglab.org/`. Accessed: 2019-08-24.

[103] Tsukuba Magnet Laboratory, Tsukuba City, Japan. `https://www.nims.go.jp`. Accessed: 2019-08-08.

[104] G. Fuchs, P. Schätzle, G. Krabbes, S. Gruß, P. Verges, K. H. Müller, J. Fink, and L. Schultz. Trapped magnetic fields larger than 14 T in bulk YBa2Cu3O7-x. *Applied Physics Letters*, 76(15):2107–2109, 2000.

[105] H. Fujishiro, T. Tateiwa, A. Fujiwara, T. Oka, and H. Hayashi. Higher trapped field over 5 T on HTSC bulk by modified pulse field magnetizing. *Physica C: Superconductivity and its Applications*, 445-448:334 – 338, 2006. Proceedings of the 18th International Symposium on Superconductivity (ISS 2005).

[106] H. Fujishiro, K. Yokoyama, M. Kaneyama, T. Oka, and K. Noto. Estimation of generated heat in pulse field magnetizing for smbacuo bulk superconductor. *Physica C: Superconductivity*, 412-414:646 – 650, 2004. Proceedings of the 16th International Symposium on Superconductivity (ISS 2003). Advances in Superconductivity XVI. Part I.

[107] T. Ida, Y. Kimura, T. Sano, K. Yamaguchi, M. Izumi, and M. Miki. Trapped field measurements of gd-ba-cu-o bulk superconductor in controlled pulse field magnetizing. *Journal of Physics: Conference Series*, 97:012292, feb 2008.

[108] M. Ainslie, H. Fujishiro, T. Ujiie, J. Zou, A. Dennis, Y. Shi, and D. Cardwell. Modelling and comparison of trapped fields in (RE)BCO bulk superconductors for activation using pulsed field magnetization. *Superconductor Science and Technology*, 27(6):065008, apr 2014.

[109] J. Zou, M. Ainslie, H. Fujishiro, A. Bhagurkar, T. Naito, N. Hari Babu, J-f Fagnard, P. Vanderbemden, and A. Yamamoto. Numerical modelling and comparison of MgB 2 bulks fabricated by HIP and in fi ltration growth. *Superconductor Science and Technology*, 28(7):1–9, 2015.

[110] T. Ida, H. Matsuzaki, Y. Akita, M. Izumi, H. Sugimoto, Y. Hondou, Y. Kimura, N. Sakai, S. Nariki, I. Hirabayashi, M. Miki, M. Murakami, and M. Kitano. Magnetization properties for gd–ba–cu–o bulk superconductors with a couple of pulsed-field vortex-type coils. *Physica C: Superconductivity*, 412-414:638 – 645, 2004. Proceedings of the 16th International Symposium on Superconductivity (ISS 2003). Advances in Superconductivity XVI. Part I.

[111] H. Fujishiro, T. Naito, and M. Oyama. Mechanism of magnetic flux trapping on superconducting bulk magnetized by pulsed field using a vortex-type coil. *Superconductor Science and Technology*, 24(7):075015, 2011.

[112] H. Kamijo and H. Fujimoto. Repeated pulsed-field magnetization with temperature control in a high-t bulk superconductor. *IEEE Transactions on Applied Superconductivity*, 11(1):1816–1819, March 2001.

[113] U. Mizutani, H. Ikuta, T. Hosokawa, H. Ishihara, K. Tazoe, T. Oka, Y. Itoh, Y. Yanagi, and M. Yoshikawa. Applications of superconducting permanent magnets driven by static and pulsed fields. *Superconductor Science and Technology*, 13(6):836–840, 2000.

[114] M. Sander, U. Sutter, R. Koch, and M. Kläser. Pulsed magnetization of HTS bulk parts at less 77 k. *Superconductor Science and Technology*, 13(6):841–845, may 2000.

[115] M. Sander, U. Sutter, M. Adam, and M. Kläser. Comparison of pulsed magnetization processes for hts bulk parts. *Superconductor Science and Technology*, 15(5):748–753, apr 2002.

[116] H. Fujishiro, T. Hiyama, T. Naito, Y. Yanagi, and Y. Itoh. Enhancement of trapped field and total trapped flux on GdBaCuO bulk by the MMPSC + IMRA method. *Superconductor Science and Technology*, 22(9):095006, aug 2009.

[117] R. Weinstein, D. Parks, R. Persad Sawh, K. Davey, and K. Carpenter. Observation of a bean model limit-A large decrease in required applied activation field for TFMs. *IEEE Transactions on Applied Superconductivity*, 25(3), 2015.

[118] F. Werfel, U. Floegel-Delor, R. Rothfeld, T. Riedel, D. Wippich, B. Goebel, and P. Schirrmeister. Bulk superconductors in mobile application. *Physics Procedia*, 36:948–952, 2012.

[119] K. Haran, S Kalsi, T. Arndt, H. Karmaker, R. Badcock, B. Buckley, T. Haugan, M. Izumi, D. Loder, J. W. Bray, P. Masson, and E. Stautner. High power density superconducting rotating machines - Development status and technology roadmap. *Superconductor Science and Technology*, 30(12):123002, 2017.

[120] B. Felder, M. Miki, K. Tsuzuki, N. Shinohara, H. Hayakawa, and M. Izumi. A 100-w grade closed-cycle thermosyphon cooling system used in hts rotating machines. *AIP Conference Proceedings*, 1434(1):417–424, 2012.

[121] Nippon Gases Deutschland GmbH, Dresden, Germany. `https://www.nippongases.com/de`. Steffen Eulitz: discussion on actual prizes (2019-08-23).

[122] J G Weisend. *Cryostat Design Case Studies, Principles and Engineering.* Springer International Publishing Switzerland, 2016.

[123] G.Kaiser and G. Schroeder. *Applied Superconductivity. Handbook on Devices and Applications*, volume 1, chapter Cryocoolers, pages 383– 392. Wiley-VHC Verlag GmbH, 2012.

[124] R. Radebaugh. Cryocoolers: the state of the art and recent developments. *Journal of Physics: Condensed Matter*, 21(16):164219, 2009.

[125] A. T. A. M. de Waele. Basic operation of cryocoolers and related thermal machines. *Journal of Low Temperature Physics*, 164(5):179, 2011.

[126] R. Radebaugh. Refrigeration for superconductors. *Proceedings of the IEEE*, 92(10):1719–1734, Oct 2004.

[127] K. Yokoyama, A..i Katsuki, A. Miura, and T. Oka. Comparison of magnetizing characteristics of superconducting bulk magnet cooled by Stirling and GM refrigerators during pulsed field magnetization. *IEEE Transactions on Applied Superconductivity*, 28(4):4–7, 2018.

[128] R. G. Ross and D. L. Johnson. Effect of gravity orientation on the thermal performance of stirling-type pulse tube cryocoolers, 2003.

[129] Sunpower, Inc., Ohaio, USA. `https://www.sunpowerinc.com/products/cryocoolers/cryotel-cryocoolers`. Accessed: 2019-08-08.

[130] AIM Infrarot-Module GmbH, Heilbronn, Germany. `https://www.aim-ir.com/`. Sebastian Zehner - private communication: 2017.

[131] Thales Cryogenics, Blagnac Cedex, France. `http://www.thales-cryogenics.com`. Oliver Clesca - private communication: 2017.

[132] H.J.M. ter Brake and G.F.M. Wiegerinck. Low-power cryocooler survey. *Cryogenics*, 42(11):705 – 718, 2002.

[133] R. Richardson. Pulse tube refrigerator — an alternative cryocooler? *Cryogenics*, 26(6):331 – 340, 1986.

[134] P. Kittel. Advances in Cryogenic Engineering. page 1 p, 1995. Cryogenic Engineering Conference, held Jyly 17-21, 1995 Columbus, Ohio.

[135] S. Moldenhauer, A. Thess, C. Holtmann, and C. Fernández-Aballí. Thermodynamic analysis of a pulse tube engine. *Energy Conversion and Management*, 65:810 – 818, 2013. Global Conference on Renewable energy and Energy Efficiency for Desert Regions 2011 2011.

[136] E. Mikulin, A. Tarasov, and M. Shkrebyonock. *Low-Temperature Expansion Pulse Tubes*, pages 629–637. Springer US, Boston, MA, 1984.

[137] R. Radebaugh, J. Zimmerman and. D.Zimmerman, D. Smith, and Louie B. Cryocoolers: the state of the art and recent developments. *Adv. Cryog. Eng.*, 31:779, 1986.

[138] M. Green and H. Witte. The use of small coolers in a magnetic field. *AIP Conference Proceedings*, 985(1):1299–1306, 2008.

[139] M. Green. The cost of coolers for cooling superconducting devices at temperatures at 4.2 k, 20 k, 40 k and 77 k. *IOP Conference Series: Materials Science and Engineering*, 101(1):012001, 2015.

[140] Lihan Technologies Co., Ltd., Shenzhen, China. `http://www.lihantech.com/`. Xiaozhong Cheng - private communication: 2016.

[141] O. Vakaliuk. Report on cryocooler for superconducting magnet system. Technical report, Techniche Universität Ilmenau, 2016.

[142] S. Nariki, N. Sakai, and M. Murakami. Melt-processed Gd-Ba-Cu-O superconductor with trapped field of 3 T at 77 K. *Superconductor Science and Technology*, 18(2), 2005.

[143] S. Gruss, G. Fuchs, G. Krabbes, P. Verges, G. Stöver, K. H. Müller, J. Fink, and L. Schultz. Superconducting bulk magnets: Very high trapped fields and cracking. *Applied Physics Letters*, 79(19):3131–3133, 2001.

[144] M Tomita and M Murakami. High-temperature superconductor bulk magnets that can trap magneitc fields of over 17 tesla at 29 kelvin. *Nature*, 421:517, 2003. doi:10.1103/PhysRevLett.96.164501.

[145] G. Milne. *Gardner's Commercially Important Chemicals: Synonyms, Trade Names, and Properties*. John Wiley & Sons, 2005.

[146] T. Johansen. Flux-pinning-induced stress and magnetostriction in bulk superconductors. *Superconductor Science and Technology*, 13(10), 2000.

[147] Y. Ren, R. Weinstein, J. Liu, R. P. Sawh, and C. Foster. Damage caused by magnetic pressure at high trapped field in quasi-permanent magnets composed of melt-textured YBaCuO superconductor. *Physica C: Superconductivity and its applications*, 251(1-2):15–26, 1995.

[148] P. Diko. Cracking in melt-grown RE-Ba-Cu-O single-grain bulk superconductors. *Superconductor Science and Technology*, 17(11):45–58, 2004.

[149] M. Tomita, M. Murakami, and K. Yoneda. Improvements in the mechanical properties of bulk ybco superconductors with carbon fibre fabrics. *Superconductor Science and Technology*, 15(5):803, 2002.

[150] T. Miyamoto, K. Nagashima, N. Sakai, and M. Murakami. Direct measurements of mechanical properties for large-grain bulk superconductors. *Physica C: Superconductivity*, 340(1):41 – 50, 2000.

[151] D. Lee and K. Salama. Enhancements in current density and mechanical properties of y-ba-cu-o/ag composites. *Japanese Journal of Applied Physics*, 29(11A):L2017, 1990.

[152] U. Floegel-Delor, T. Riedel, D. Wippich, B. Goebel, R. Rothfeld, P. Schirrmeister, F. Werfel, A .Usoskin, and A Rutt. Reel-to-reel copper electroplating on

pulse laser deposition coated conductor. *IEEE Transactions on Applied Superconductivity*, 21(3):2984–2987, June 2011.

[153] D. Namburi, J. Durrell, J. Jaroszynski, Y. Shi, M. Ainslie, K. Huang, A. Dennis, Er. Hellstrom, and D. Cardwell. A trapped fi eld of 14 . 3T in Y − Ba − Cu − O bulk superconductors fabricated by buffer- assisted seeded in fi ltration and growth. *Superconductor Science and Technology*, 2018.

[154] H. Seki, Y. Honma, M. Nomura, C. Nakayama, N. Koshizuka, T. Maruyama, and M. Murakami. Reinforcement of bulk Y-Ba-Cu-O superconductors by using Fe-Mn-Si-Ni shape memory alloy rings. *Physics Procedia*, 27(December):144–147, 2012.

[155] T.H. Johansen, Q.Y. Chen, and W.-K. Chu. Pinning-induced stress in clamped superconductors. *Physica C: Superconductivity*, 349(3):201 − 210, 2001.

[156] X. Yang and W. Gan. Effect of thermal dilation stress and flux pinning induced stress on superconductor/tube system. *Journal of Superconductivity and Novel Magnetism*, 26(10):3057–3063, Oct 2013.

[157] F. Trillaud, K. Berger, B. Douine, and J. Lévêque. Temperature , mechanical deformation and current density distribution in YBCO bulks during magnetization. *IEEE Transactions on Applied Superconductivity*, 28(4):6800805, 2016.

[158] H Fujishiro, M D Ainslie, K Takahashi, T Naito, Y Yanagi, Y Itoh, and T Nakamura. Simulation studies of mechanical stresses in rebacuo superconducting ring bulks with infinite and finite height reinforced by metal ring during field-cooled magnetization. *Superconductor Science and Technology*, 30(8):085008, 2017.

[159] K. Takahashi, H. Fujishiro, T. Naito, Y. Yanagi, Y. Itoh, and T. Nakamura. Fracture behavior analysis of EuBaCuO superconducting ring bulk reinforced by a stainless steel ring during field-cooled magnetization. *Superconductor Science and Technology*, 30(11):115006, 2017.

[160] K. Takahashi, H. Fujishiro, T. Naito, Y. Yanagi, Y. Itoh, and T. Nakamura. Numerical Simulation of Electromagnetic and Thermal Stress in REBaCuO Superconducting Ring and Disk Bulks Reinforced by Stainless Steel Ring with Various Widths during Field-Cooled Magnetization. *IEEE Transactions on Applied Superconductivity*, 28(3), 2018.

[161] H. Wu, H. Yong, and Y. Zhou. Stress analysis in high-temperature superconductors under pulsed field magnetization. *Superconductor Science and Technology*, 31(4):45008, 2018.

[162] M D Ainslie, K Y Huang, H Fujishiro, J Chaddock, and K Takahashi. Numerical modelling of mechanical stresses in bulk superconductor magnets with and without mechanical reinforcement. *Superconductor Science and Technology*, 2019.

[163] E. Baruch-El, M. Baziljevich, B. Ya. Shapiro, T. H. Johansen, A. Shaulov, and Y. Yeshurun. Dendritic flux instabilities in $YBa_2Cu_3O_{7-x}$ films: Effects of temperature and magnetic field ramp rate. *Phys. Rev. B*, 94:054509, Aug 2016.

[164] P. Swartz and C. Bean. A model for magnetic instabilities in hard superconductors: The adiabatic critical state. *Journal of Applied Physics*, 39(11):4991–4998, 1968.

[165] R. Mints and E. Brandt. Flux jumping in thin films. *Phys. Rev. B*, 54:12421–12426, Nov 1996.

[166] Merriam-Webster Dictionary. `https://www.merriam-webster.com/dictionary/electrolyte`. Accessed: 2019-08-08.

[167] B. Kumar. *Magnetohydrodynamic duct and channel flows at finite magnetic Reynolds numbers.* PhD thesis, Technische Universität Ilmenau, 2016.

[168] C. Heinicke. *Local Lorentz Force Velocimetry for liquid metal duct flows.* PhD thesis, Technische Universität Ilmenau, 2013.

[169] V. Minchenya, C. Karcher, Y. Kolesnikov, and A. Thess. Calibration of the lorentz force flowmeter. *Flow Measurement and Instrumentation*, 22(3):242 – 247, 2011.

[170] I. Sokolov, Y. Kolesnikov, and A. Thess. Experimental investigation of the transient phase of the Lorentz force response to the time-dependent velocity at finite magnetic Reynolds number. *Measurement Science and Technology*, 25(12), 2014.

[171] H. Brauer and M. Ziolkowski. Eddy current testing of metallic sheets with defects using force measurements. *Serbian Journal of Electrical Engineering*, 5(1):11–20, 2008.

[172] M. Ziolkowski and H. Brauer. Fast computation technique of forces acting on moving permanent magnet. *IEEE Transactions on Magnetics*, 46(8):2927–2930, 2010.

[173] M. Zec. *Theory and Numerical Modelling of Lorentz Force Eddy Current Testing.* PhD thesis, Technische Universität Ilmenau, 2013.

[174] K. Weise. *Advanced Modeling in Lorentz Force Eddy Current Testing Dissertation.* PhD thesis, Technishe Universität Ilmenau, 2016.

[175] R. Uhlig. *Identification of Material Defects in Metallic Materials Using Lorentz Force Eddy Current Testing.* PhD thesis, Technische Universität Ilmenau, 2013.

[176] M. Carlstedt. *A Contribution to the Experimental Validation in Lorentz Force Eddy Current Testing.* PhD thesis, Techniche Universität Ilmenau, 2017.

[177] B. Petković. *Assessment of Linear Inverse Problems in Magnetocardiography and Lorentz Force Eddy Current Testing.* PhD thesis, Technische Universität Ilmenau, 2013.

[178] H. Brauer, Weise K. Ziolkowski, M., M. Carlstedt, R. Uhlig, and M. Zec. *Motion-Induced Eddy Current Techniques for Non-Destructive Testing and Evaluation.* The Institution of Engineering and Technology (IET), London, United Kingdom, 2018.

[179] H. Brauer and M. Ziolkowski. Motion-induced eddy current testing. In *Handbook of Advanced Non-Destructive Evaluation, N. Ida, N. Meyendorf (Eds.).* Springer, Cham, 2018.

[180] R. Schmidt, J. M. Otterbach, M. Ziolkowski, H. Brauer, and H. Toepfer. Portable lorentz force eddy current testing system with rotational motion. *IEEE Transactions on Magnetics*, 54(3):1–4, March 2018.

[181] Otterbach J.-M., Schmidt R., Brauer H., and Ziolkowski M. Portable system for motion induced eddy current testing. Nürnberg, Germany, June 2018.

[182] E-V. Doelker, R. Schmidt, K. Weise, B. Petković, M. Ziolkowski, H. Brauer, and J. Haueisen. Assessment of two forward solution approaches in lorentz force evaluation. *IEEE Transactions on Magnetics*, 54(3):1–5, March 2018.

[183] M. Werner. *Design, Optimierung, Realisierung und Test von passiven Magnetsystemen für die Lorentzkraftanemometrie an Elektrolyten.* PhD thesis, Techniche Universität Ilmenau, 2013.

[184] C. Diethold. *Lorentzkraft-Anemometrie von elektrisch schwach leitfähigen Fluiden.* PhD thesis, Techniche Universität Ilmenau, 2016.

[185] A. Wegfraß. *Experimentelle Untersuchungen zur Anwendbarkeit der Lorentzkraft-Anemometrie auf schwach leitfähige Fluide.* PhD thesis, Techniche Unibersität Ilmenau, 2013.

[186] R. Ebert. *Kontaktlose Durchflussmessung in turbulenten Elektrolytströmungen mittels Lorentzkraft Anemometrie Kontaktlose Durchflussmessung in turbulenten Elektrolytströmungen mittels Lorentzkraft Anemometrie.* PhD thesis, Technische Universität Ilmenau, 2016.

[187] Weidner M. Innovative magnet system based on high-temperature superconductors. Technical report, Research Training Group "Lorentz Force Velocimetry and Lorentz Eddy Current Testing", 2016. Presented at closed workshop in Kloster Banz, Germany.

[188] A. Wiederhold. *Strömungsmessung und Strömungsbeeinflussung in leitfähigen Mehrphasensystemen durch elektromagnetische Kräfte.* PhD thesis, Technische Universität Ilmenau, 2019.

[189] A Wiederhold, R Ebert, M Weidner, B Halbedel, T Fröhlich, and C Resagk. Influence of the flow profile to Lorentz force velocimetry for weakly conducting fluids—an experimental validation. *Measurement Science and Technology*, 27(12):125306, 2016.

[190] C. Diethold and F. Hilbrunner. Force measurement of low forces in combination with high dead loads by the use of electromagnetic force compensation. *Measurement Science and Technology*, 23(7), 2012.

[191] S. Vasilyan, M. Rivero, J. Schleichert, B. Halbedel, and T. Fröhlich. High-precision horizontally directed force measurements for high dead loads based on a differential electromagnetic force compensation system. *Measurement Science and Technology*, 27(4):045107, 2016. doi:10.1088/0957-0233/27/4/045107.

[192] H. Weis, F. Hilbrunner, T. Fröhlich, and G. Jäger. Mechatronic FEM model of an electromagnetic-force-compensated load cell. *Measurement Science and Technology*, 23(7), 2012.

[193] M. Werner and B. Halbedel. Optimization of NdFeB magnet arrays for improvement of lorentz force velocimetry. *IEEE Transactions on Magnetics*, 48(11):2925–2928, 2012.

[194] T. Koishi, S. Kawase, and S. Tamaki. A theory of electrical conductivity of molten salt. *Journal of Chemical Physics*, 116(7):3018–3026, 2002.

[195] R. W. Higgs and T. A. Litovitz. Ultrasonic Absorption and Velocity in Molten Salts. *The Journal of the Acoustical Society of America*, 32(9):1108–1115, 1960.

[196] O. Vakaliuk, M. Weidner, and B. Halbedel. High-temperature superconducting magnet systems for Lorentz Force Velocimetry. In *XVIII International UIE-Congress Electrotechnologies for Material Processing*, number June, Hannover, Germany, 2017.

[197] J. Mauro and E. Zanotto. Two centuries of glass research: Historical trends, current status, and grand challenges for the future. *International Journal of Applied Glass Science*, 5(3):313–327, 2014. http://dx.doi.org/10.1111/ijag.12087.

[198] B. Berman. Our bodies' velocities, by the numbers, June 2014. Science for the curious Discover.

[199] O. Vakaliuk, M. Ainslie, and B. Halbedel. Lorentz force velocimetry using a bulk HTS magnet system: proof-of-concept. *Superconductor Science and Technology*, 31(8), 2018.

[200] R. Ebert, J. Leineweber, and C. Resagk. Performance enhancement of a Lorentz force velocimeter using a buoyancy-compensated magnet system. *Measurement Science and Technology*, 26(7):075301, 2015.

[201] M. Klaiber. Untersuchung an hochtemperatursupraleitern als magnetfeldquellen für die lorentzkraft-anemometrie an elektrolytströmungen. Master's thesis, Technische Universität Ilmenau, 2013.

[202] Cryogenic, London. UK. `http://www.cryogenic.co.uk`. The cryomagnetic magnet system contains the cryogen free room temperature bore superconducting

magnet, cryostat, cryocooler and compressor, temperature monitor unit (nominally Lakeshore) and HTS current leads. The cooling for the magnet and cryostat housing is provided by a standard cryocooler with a base temperature of 4K. This magnet provides field up to 5 T in the middle of the bore.

[203] M. Weidner, B. Halbedel, and E. Readlein. Expectable Forces of Lorentz Force Velocimetry in low conducting and slow flowing solutions by the use of high-Tc superconductors. Number OCTOBER, Lyon, France, 2015.

[204] Andreas Kade. *Handbuch zur Verwendung der Heliumkryostate für die Entwicklung eines Durchflussmesssystems (Lorentzkraftanemometrie auf HTSL-Basis).* Institut für Luft- und Kältetechnik gemeinnützige Gesellschaft mbH (ILK), 2015.

[205] K. Yokoyama, T. Oka, H. Okada, Y. Fujine, A. Chiba, and K. Noto. Solid-liquid magnetic separation using bulk superconducting magnets. *IEEE Transactions on Applied Superconductivity*, 13(2 II):1592–1595, 2003.

[206] K. Yokoyama, T. Oka, and K. Noto. A strong magnetic field generation by superconducting bulk magnets with the same pole arrangement. *IEEE Transactions on Applied Superconductivity*, 19(3):2178–2181, 2009.

[207] T. Oka, H. Kanayama, K. Tanaka, S. Fukui, J. Ogawa, T. Sato, M. Yamaguchi, M. Ooizumi, K. Yokoyama, and K. Noto. Study on magnetic separation system using high Tc superconducting bulk magnets for water purification technique. *Journal of Physics: Conference Series*, 156:2–7, 2009.

[208] T. Oka, Y. Yamada, T. Horiuchi, J. Ogawa, S. Fukui, T. Sato, K. Yokoyama, and M. Langer. Magnetic flux-trapping of anisotropic-grown Y-Ba-Cu-O bulk superconductors during and after pulsed-field magnetizing processes. *Journal of Physics: Conference Series*, 507(PART 1):9–13, 2014.

[209] A. Alferenok, A. Pothérat, and U. Luedtke. Optimal magnet configurations for Lorentz force velocimetry in low conductivity fluids. *Measurement Science and Technology*, 24(6), 2013.

[210] Mark D. Ainslie, Jan Srpcic, DIfan Zhou, Hiroyuki Fujishiro, Keita Takahashi, David A. Cardwell, and John H. Durrell. Toward Optimization of Multi-Pulse, Pulsed Field Magnetization of Bulk High-Temperature Superconductors. *IEEE Transactions on Applied Superconductivity*, 28(4), 2018.

[211] X. Yang and S. Tu. The effect of a constraining metal tube on flux pinning induced stress in a long cylindrical superconductor. *Journal of Applied Physics*, 112(2), 2012.

[212] G. Krabbes, W. Bieger, P. Schätzle, and U. Wiesner. Improved HTSC bulk materials: A thermodynamic approach to processing. *Superconductor Science and Technology*, 11(1):144–148, 1998.

[213] N. Yan, S. Vasilyan, M. Kühnel, and T. Fröhlich. Investigation to the tilt sensitivity of the Lorentz force velocimetry system for the flow rate measurement of low conducting fluids. In *Helsinki, Finland*, pages 3–6, Helsinki, Finland, 2017.

[214] N. Yan, M. Kühnel, S. Vasilyan, and T. Fröhlich. Torsion balance-based system for high-precision force measurement in horizontal plane: Part I. Development concept. *Measurement Science and Technology*, 29(8), 2018.

[215] C-Flex Bearing Company 2015 Design guide:'C-Flex pivot bearing, D-10'. `https://c-flex.com/pivot-bearings/design-guide/`. Accessed: 2019-08-08.

[216] B. Halbedel, O. Vakaliuk, T. Fröhlich, and N. Yan. Vorrichtung zur Ermittlung von Parametern einer elektrisch leitfähigen Substanz und dazugehöriges Verfahren: DE102017005210A12018.12.20, 2017.

[217] D. Dietrich. *Magnetically Soft Materials, ASM Handbook*, volume 2 of *Properties and Selection: Nonferrous Alloys and Special-Purpose Materials*. ASM, Materials Park, 1990.

[218] M. Ziolkowski, H. Brauer, B. Halbedel, and U. Krieger. Simulation of the Distribution of Paramagnetic Ions in Melts Influenced by Inhomogeneous Magnetic Fields. *2. Multiphysics*, pages 871–872, 2007.

[219] Schadewald U., Halbedel B., Ziolkowski M. , Brauer H. Influence of magnetic Kelvin forces on aqueous solution containing paramagnetic FeII ions. In *Influence of magnetic kelvin forces on aquaous solutions containing paramagnetic Fe-III ions*, page 1, 4-th International Conference on magneto-Science, Shanhai, 2011.

[220] CF flanges, Kurt J. Lesker, Technical notes. `https://www.lesker.com/newweb/flanges/flanges_technicalnotes_conflat_1.cfm`. Accessed: 2019-09-04.

[221] KF flanges, Kurt J. Lesker, Technical notes. `https://www.lesker.com/newweb/flanges/flanges_technicalnotes_kf_1.cfm`. Accessed: 2019-09-04.

[222] VACOM, Jena, Germany. `https://www.vacom.de/en/products/standard-components/materials/aluminum`. Accessed: 2019-09-04.

[223] RUAG Thermal insulation products. `https://www.ruag.com/sites/default/files/2016-12/150622_Broschuere_Thermal_Jun2015_single-low.pdf`. Accessed: 2019-11-08.

[224] Ozan Keysan. *Superconducting Generators for Large Offshore Wind Turbines Doctor of Philosophy*. PhD thesis, The University of Edinburgh, 2014.

[225] M. Haug. *Liquid Nitrogen Cooled Cryostat to Provide Mechanical Stability on a Nanometre Level for the Astronomical Instrument GRAVITY*. PhD thesis, University of Applied Sciences Munich, 2013.

[226] High power LED, L9337-02, Hamamatsu. `https://www.hamamatsu.com/eu/en/product/type/L9337-02/index.html`. Accessed: 2019-10-03.

[227] Silicon Differential Photodiode, SIEMENS. `https://datasheetspdf.com/pdf-file/486493/SiemensSemiconductorGroup/SFH221S/1`. Accessed: 2019-10-03.

[228] I. Valiente-Blanco, E. Diez-Jimenez, J. A. Cervantes-Montoro, and J. L. Perez-Diaz. Characterization of commercial-off-the-shelf electronic components at cryogenic temperatures. *Instruments and Experimental Techniques*, 56(6):665–671, 2013.

[229] E. Bardalen, H. Karlsen, B.and Malmbekk, M. N. Akram, and P. Ohlckers. Evaluation of InGaAs/InP photodiode for high-speed operation at 4 K. *International Journal of Metrology and Quality Engineering*, 9:13–17, 2018.

[230] E. Bardalen, B. Karlsen, H. Malmbekk, M. Akram, and P. Ohlckers. Reliability study of fiber-coupled photodiode module for operation at 4 K. *Microelectronics Reliability*, 81(September 2017):362–367, 2018.

[231] F. Wauters, I. S. Kraev, M. Tandecki, E. Traykov, S. Van Gorp, D. Zákoucký, and N. Severijns. Performance of silicon PIN photodiodes at low temperatures and in high magnetic fields. *Nuclear Instruments and Methods in Physics Research, Section A: Accelerators, Spectrometers, Detectors and Associated Equipment*, 604(3):563–567, 2009.

[232] L. Yang, S. N. Dzhosyuk, J. M. Gabrielse, P. R. Huffman, C. E.H. Mattoni, S. E. Maxwell, D. N. McKinsey, and J. M. Doyle. Performance of a large-area avalanche photodiode at low temperature for scintillation detection. *Nuclear Instruments and Methods in Physics Research, Section A: Accelerators, Spectrometers, Detectors and Associated Equipment*, 508(3):388–393, 2003.

[233] K. Seeger. *Semiconductor Physics (An Introduction)*. Springer, Berlin, Germany, 1985.

[234] C. Diethold, Laser Imaging, Systems Gmbh, and F. Hilbrunner. High precission optical position sensor for electromagnetic force compensated balances. (November), 2010.

Acronyms and Variables

Acronyms

CFC	cryogenic force cell
DEMFC	Differential Electromagnetic Force Compensation Balance
EFB	electrostatic force balancing
EMFC	Electromagnetic Force Compensation Balance
FMS	force measurement system
GHe	gaseous helium
LED	light-emitting diode
LFV	Lorentz Force Velocimetry
LRE	Light rare earth elements
HTS	high-temperature superconductor
LN$_2$	Liquid nitrogen
LHe	Liquid helium
MS	magnet system
NFMFL	National High Magnetic Field Laboratory
PFMS	Pendulum Force Measurement System
PM	permanent magnet
RT	room temeprature
RTG	Research Training Group

TFM   Trapped Field Magnet

TFMS   Torsion Force Measurement System

sTFMS   scaled-down Torsion Force Measurement System

Super-LOFOS **Super**conducting High-precision **Lo**rentz **Fo**rce Measurement **S**ystem

Variables

A Surface area

B Magnetic lux density

B_A Applied magnetic flux density

B_c Critical magnetic field of a superconductor

B_{c1} First critical magnetic flux density

B_{c2} Second critical magnetic flux density

$(BH)_{max}$ Maximal energy density of a permanent magnet

B_{in} Internal magnetic flux density

B_{irr} Irreversibility magnetic flux density

B_{j1} First flux jump

B_p Full penetration magnetic flux density

B_r Remanence of a permanent magnet

B_T Trapped magnetic flux density

$B_{T,exp}$ Experimetally measured trapped magnetic flux density

$B_{T,sim}$ Simulated trapped magnetic flux density

$^z B_T$ Measured trapped magnetic flux density distant from the bulk HTS's surface

D_{th} Thermal diffusivity

D_m	Magnetic diffusivity
F	Force
F_L	Lorentz force
$F_{L,HTS}$	Lorentz force acting on bulk HTS during magnetization
$F_{\nabla B,fb}$	Magnetic vector gradient force
E	Young's modulus
F_{es}	Electrostatic force
H_A	Anisotropy field of a permanent magnet
I_{ex}	LED excitation current
$_JH_c$	Coercive field of a permanent magnet
J	Magnetic polarization
L	Length
L_1	Arm length of dummy counterweight
L_2	Arm length of of the magnet system
$\dot{Q}_r$	Radiative heat transfer
$\dot{Q}_g$	Gas heat transfer
$\dot{Q}_v$	Heat transfer through vacuum
$\dot{Q}_c$	Heat transfer through solid
M	Magnetization of a permanent magnet
N	Number of intermediate surfaces between the RT and T_{op}
P	Pressure
Q_c	Heat lift of a cryocooler
R	Radius of the bulk HTS
Re_m	Magnetic Reynolds numbers

T	Temperature
T_c	Critical temperature of a superconductor
T_{curie}	Curie temperature of the ferromagnetic material
T_{shrink}	Temperature, at which sample was heate to shrink the metal tube of a superconductor
T_{op}	Operating temperature
ΔT	Temperature difference
V	Volume
V_a	Applyed an electrostatic voltage
ΔV_{ph}	Output voltage of differential photodiode
V_{LED}	LED forward voltage
$a; b; c$	Growth directions
d	Separation between plates
j	Currnet density
j_c	Critical currnet density of a superconductor
h	Heat transfer coefficient
m	Mass
m_1	Mass of dummy counterweight
m_2	Mass of the magnet system
m_{fb}	Mass of the D-10 flexure bearing
t	The finite thickness of a disc-shaped bulk superconductor
$\dot{q}_{MLI}$	Heat flux through MLI
u	Velocity
$x; y; z$	Cartesian coordinates

$r; \theta; z$ Cylindrical coordinates

ε Factor for the reflectivity and geometry of the material

θ Rotation angle

κ Ginzburg-Landau parameter

$\overline{\lambda}$ Mean value of the temperature-dependent gas thermal conductivity

λ_p penetration depth of the magnetic field

$\lambda(T)$ Tempeture-dependent thermal conductivity

ξ Coherence length

ρ Density

σ Electrical conductivity

σ_B Tensile strength of a bulk HTS

σ_{ns} Surface energy at the interface between normal and superconducting state

χ Magnetic susceptibility

Constants

K_{es} sTFMS calibration constant ($0.04\,\mu\mathrm{N}\,\mathrm{V}^{-2}$)

Φ_0 Quantum of the magnetic flux ($2.1 \times 10^{-15}\,\mathrm{T}\,\mathrm{m}^2$)

h_p Planck constant ($6.6 \times 10^{-34}\,\mathrm{m}^2\,\mathrm{kg}\,\mathrm{s}^{-1}$)

e Electron charge ($1.6\,\mathrm{C}$)

k gaseous helium species (2.1)

μ_0 Magnetic permeability of vacuum ($1.2 \times 10^{-6}\,\mathrm{N}\,\mathrm{A}^{-2}$)

σ_{sb} Stefan–Boltzmann constant ($5.7 \times 10^{-8}\,\mathrm{W}\,\mathrm{m}^{-1}\,\mathrm{K}^{-4}$)

List of Figures

List of Tables

Erklärung

Ich versichere, dass ich die vorliegende Arbeit ohne unzulässige Hilfe Dritter und ohne Be-nutzung anderer als der angegebenen Hilfsmittel angefertigt habe. Die aus anderen Quellen direkt oder indirekt übernommenen Daten und Konzepte sind unter Angabe der Quelle gekennzeichnet

Bei der Auswahl und Auswertung folgenden Materials haben mir die nachstehend aufgeführten Personen in der jeweils beschriebenen Weise unentgeltlich geholfen:

1) Die fachliche Betreuung der Arbeit erfolgte durch Prof. Thomas Fröhlich.

2) Hilfreiche fachliche Diskussionen wurden zudem mit Dr. Bernd Halbedel geführt.

3) Die numerische Modellierungen in Kapiteln 4.3 wurden von Dr. Mark Ainslie (Cambridge University, UK) durch fachliche Hinweise unterstützt.

4) Die Experimente in Kapitel 5.1 haben Dr. Frank Werfel (ATZ®, Torgau, Deutschland) und Dr. Jan Jaroszynski (Florida State University, Tallahassee, USA) durch fachliche Hinweise unterstützt

5) Die Experimente in Kapitel 6 wurden von Dr. Na Yan (TU Ilmenau) durch fachliche Hinweise unterstützt.

6) Zu einigen Messungen haben Studierende der TU Ilmenau Georg Langhof und Lulas Kellmann (Kapitel 4.2) im Rahmen ihrer Anstellung als studentische Assistenten unter meiner Betreuung beigetragen.

7) Zu einigen CAD Konstruktionen haben Studierende der TU Ilmenau Christian Dresler und Jonathan Ehrmann (Kapitel 5.3) im Rahmen ihrer Anstellung als studentische Assistenten unter meiner Betreuung beigetragen.

8) Cindy Karcher (TU Ilmenau) hat diese Dissertation im rein redaktionellen Sinn (Sprache, Grammatik, Rechtschreibung) Korrektur gelesen.

Weitere Personen waren an der inhaltlich-materiellen Erstellung der vorliegenden Arbeit nicht beteiligt. Insbesondere habe ich hierfür nicht die entgeltliche Hilfe von Vermittlungs- bzw. Beratungsdiensten (Promotionsberater oder anderer Personen) in Anspruch genommen. Niemand hat von mir unmittelbar oder mittelbar geldwerte Leistungen für Arbeiten erhalten, die im Zusammenhang mit dem Inhalt der vorgelegten Dissertation stehen.

Die Arbeit wurde bisher weder im In- noch im Ausland in gleicher oder ähnlicher Form einer Prüfungsbehörde vorgelegt.

Ich bin darauf hingewiesen worden, dass die Unrichtigkeit der vorstehenden Erklärung als Täuschungsversuch bewertet wird und gemäß § 7 Abs. 10 der Promotionsordnung den Abbruch des Promotionsverfahrens zur Folge hat.

Ilmenau, den 01. 12. 2019   Oleksii Vakaliuk